

Electronic Thesis and Dissertation Repository

2-15-2022 10:00 AM

Investigating tumor perfusion, glycolysis and pH environments with multimodal in vivo imaging

Qi Qi, *The University of Western Ontario*

Supervisor: Thiessen, Jonathan D., *The University of Western Ontario*

Co-Supervisor: Lee, Ting-Yim, *The University of Western Ontario*

A thesis submitted in partial fulfillment of the requirements for the Doctor of Philosophy degree in Medical Biophysics

© Qi Qi 2022

Follow this and additional works at: <https://ir.lib.uwo.ca/etd>

Recommended Citation

Qi, Qi, "Investigating tumor perfusion, glycolysis and pH environments with multimodal in vivo imaging" (2022). *Electronic Thesis and Dissertation Repository*. 8436.
<https://ir.lib.uwo.ca/etd/8436>

This Dissertation/Thesis is brought to you for free and open access by Scholarship@Western. It has been accepted for inclusion in Electronic Thesis and Dissertation Repository by an authorized administrator of Scholarship@Western. For more information, please contact wlsadmin@uwo.ca.

Abstract

Background: Cancer cells have a complex microenvironment that helps create optimal conditions for cancer proliferation. Nutrients such as glucose will pass through a tortuous and leaky vascular structure developed by cancer cells, and are subsequently distributed and transported inside the cancer cells to meet their metabolic demands. This leaky and poorly organized vasculature leads to a buildup in the interstitial fluid pressure surrounding the tumor, subsequently resulting in tumor hypoxia. Due to an overreliance on glycolysis, more acid and protons are produced by cancer cells, leading to a more acidic environment which, in combination with tumor hypoxia, often leads to a poor patient outcome. This thesis aims to explore the intrinsic relationship between tumor perfusion, glycolysis and its pH environment using a C6 rat model of glioma.

Methods: All rats were implanted with 1 million C6 glioma cells using stereotactic surgery. The growth of tumor cells was monitored either with computed tomography perfusion (CTP) or magnetic resonance imaging (MRI). Once tumors had reached the optimal size, tumor perfusion was measured using CTP. Tumor glycolytic metabolism was measured using positron emission tomography (PET) with ^{18}F -flurodeoxyglucose (FDG) and MR spectroscopy imaging (MRSI) using hyperpolarized $[1-^{13}\text{C}]$ pyruvate. Chemical exchange saturation (CEST) MRI was also used to investigate tumor glucose distribution (glucose contrast enhancement, or ΔCEST) and pH environments (intra-/extracellular pH, pH_i and pH_e respectively and simultaneously) during/after a glucose infusion/injection. All experimental procedures were completed within 24 hours. Measurements of tumor perfusion, glycolysis, ΔCEST and pH environments were correlated using Pearson's correlation.

Results: Tumor perfusion measurement of permeability surface-area product (PS) was significantly correlated with tumor glycolysis measurement of lactate to pyruvate ratio (Lac:Pyr) from hyperpolarized MRSI as well as ΔCEST . Tumor Lac:Pyr was also significantly correlated with tumor pH_i . Tumor metabolic rate of glucose derived from dynamic PET was significantly correlated with tumor pH_i and pH_e .

Conclusion: This research showed the possibility of measuring the intracellular and extracellular pH environment simultaneously. Multimodal imaging approaches provided a more complete picture of the tumor microenvironment and helped elucidate the intrinsic relationship between tumor perfusion, glycolysis and the pH environment.

Keywords

multimodal imaging, glioblastoma multiforme, cancer perfusion, cancer metabolism, cancer pH, computed tomography (CT), magnetic resonance imaging (MRI), chemical exchange saturation transfer (CEST), pH imaging, amine and amide concentration independent detection (AACID), AcidoCEST, hyperpolarized $[1-^{13}\text{C}]$ -Pyruvate MRSI, ^{18}F -flurodeoxyglucose positron emission tomography (PET), PET kinetic analysis.

Summary for Lay Audience

Cancer cells have a complex microenvironment that helps create optimal conditions for them to survive and grow. Nutrients that are essential for cancer growth such as glucose will be delivered to the cancer cells using a poorly developed vessel system that is also developed by cancer cells. The amount of nutrients delivered is based on the energy needs of cancer cells. These delivered nutrients will then be used for energy production to support the cancer cells' survival. Glycolysis is an energy production method that is mainly used by cancer cells. During glycolysis, glucose acts as a fuel and helps to produce enough energy to meet the energy demands of cancer cells. However, this energy production process is very inefficient, leading to the production of acids as a side product. As a result, this makes the environment where cancer cells reside very acidic. This acidic environment will further help cancer cells to avoid detection by the host's immune system, killing off the healthy cells around the tumor, and help cancer cells to spread into the surrounding areas. Moreover, the acidic cancer environment will lead to the formation of more vessels and further help the delivery of nutrients to cancer cells. This completes the vicious cycle between the delivery of cancer nutrients, the energy needs of cancer cells, and the acidic environment around cancer cells.

It is important to explore the relationships between the delivery process of nutrients to cancer cells to meet their metabolic demand, cancer cells' energy production and the production of acid due to the inefficient energy production commonly found in cancer. Measuring these changes with non-invasive imaging methods, we will get more insight into cancer cell growth and spreading. Ultimately, we can use this information to achieve a better treatment outcome by stopping this vicious loop.

This thesis aims to explore these intrinsic relationships among cancer nutrients delivery, energy need and the acidic environment; and better understanding the environment that the cancer cells reside using a number of complementary medical imaging methods in a clinically translatable animal cancer model.

Co-Authorship Statement

Chapter 2: Multimodality In Vivo Imaging of Perfusion and Glycolysis in a Rat Model of C6 Glioma. *Molecular Imaging and Biology*, **23**: 516-526, February 2021. DOI: 10.1007/s11307-021-01585-1.

This work was co-authored by: Qi Qi, Matthew S. Fox, Heeseung Lim, Robert Bartha, Timothy J. Scholl, Lisa Hoffman, Ting-Yim Lee, Jonathan D. Thiessen

The experiments in this chapter were performed and analyzed primarily by Qi Qi with the guidance of Drs. Jonathan D. Thiessen and Ting-Yim Lee. Dr. Matthew S. Fox oversaw animal handling though out the experiment. Drs. Heeseung Lim and Timothy J. Scholl assisted in collecting and processing the hyperpolarized [1-¹³C]pyruvate MRSI data. Dr. Robert Bartha assisted in interpreting CEST MRI data. Dr. Lisa Hoffman provided C6 glioma cells for this experiment.

Chapter 3: Glucose Infusion Induced Change in Intracellular pH and Its Relationship with Tumor Glycolysis in a C6 Rat Model of Glioblastoma. Submitted to *Molecular Imaging and Biology* on November 2, 2021.

This work was co-authored by: Qi Qi, Matthew S. Fox, Heeseung Lim, Rebecca Sullivan, Alex Li, Miranda Bellyou, Lise Desjardins, Andrew McClennan, Robert Bartha, Lisa Hoffman, Timothy J. Scholl, Ting-Yim Lee, Jonathan D. Thiessen

The experiments in this chapter were performed and analyzed primarily by Qi Qi with the guidance of Drs. Jonathan D. Thiessen and Ting-Yim Lee. Dr. Matthew S. Fox and Lise Desjardins oversaw animal handling though out the experiment. Drs. Heeseung Lim and Timothy J. Scholl assisted in collecting and processing the hyperpolarized [1-¹³C]pyruvate MRSI data. Dr. Alex Li and Miranda Bellyou helped with CEST data collection. Dr. Robert Bartha assisted in interpreting CEST MRI data. Dr. Lisa Hoffman and Andrew McClennan provided C6 glioma cells for this experiment. Dr. Rebecca Sullivan helped with making pH phantoms for pH calibration.

Chapter 4: Evaluation of the Change in Tumor Intra-/Extracellular pH Environment Induced by Glucose Injection and its Relationship with Tumor Glycolysis in a C6 Rat Model of Glioblastoma. To be submitted to an appropriate journal in 2022.

This work was co-authored by: Qi Qi, Matthew S. Fox, Heeseung Lim, Harris Smailovic, Rebecca Sullivan, Alex Li, Miranda Bellyou, Lise Desjardins, Andrew McClennan, Robert Bartha, Lisa Hoffman, Timothy J. Scholl Ting-Yim Lee, Jonathan D. Thiessen

The experiments in this chapter were performed and analyzed primarily by Qi Qi with the guidance of Drs. Jonathan D. Thiessen and Ting-Yim Lee. Drs. Matthew S. Fox and Heeseung Lim, and Lise Desjardins oversaw animal handling throughout the experiment. Dr. Alex Li and Miranda Bellyou helped with CEST data collection. Dr. Robert Bartha assisted in interpreting CEST MRI data. Dr. Scholl helped with experiment plans and validation. Dr. Lisa Hoffman and Andrew McClennan provided C6 glioma cells for this experiment. Dr. Rebecca Sullivan and Harris Smailovic assisted in making pH phantoms for pH calibration.

Acknowledgments

Thank you to the Lawson Internal Research Fund, Natural Sciences and Engineering Research Council of Canada, and Ontario Research Fund for supporting the projects presented in this thesis.

I am very grateful for the help and guidance I have received from my supervisor Dr. Jonathan D. Thiessen throughout my PhD training. Jonathan has always been patient and supportive over the past 6 years, and has helped to shape me to be a more meticulous researcher. I am also very thankful to my co-supervisor, Dr. Ting-Yim Lee. I might not have been the most attentive student, but your diligence and professionalism are what I would strive to achieve in the future. Thank you Jonathan and Ting.

I would like to thank my advisory committee members: Drs. Timothy Scholl, Aaron So and James Koropatnick, they have provided numerous invaluable suggestions for my thesis and made sure that I am in a good academic standing.

I would like to thank Drs. Matthew S. Fox and Heeseung (Patrick) Lim. Matt has helped me in all aspects of my experiment tirelessly and made sure that the experiments of all of my projects were able to finish smoothly. Patrick only joined the Hybrid-Imaging Lab in 2020, but he had been helping and training me since I started my graduate studies in 2016. Both Matt and Patrick have provided a lot of helpful suggestions for my projects.

I would like to thank Jennifer Hadway and Lise Desjardins from the Lee lab for teaching me how to care for the animals and helped me tremendously with animal handling throughout my projects. I would not have been able to finish the last set of projects without their help.

I would like to thank Drs. Alex Li and Robert Bartha for their help and guidance on how to analyze the acquired CEST data. I would also like to thank Miranda Bellyou who help with the animal handling at CFMM.

Thank you to our previous lab member Nassir Al-Khishman for helping me when I first took on the project, you really lightened a lot of the load!

Thank you Dr. Udunna Anazodo for all the helps and inspiring talks we had over the years, you really helped me by expanding my horizons on research.

Thank you to all my previous mentors Drs. Timothy Pok Chi Yeung, Slav Yartsev, Sarah Mattonen and Aaron Ward for introducing me to research and helping me developing proper research skills.

Thank you to Dr. Benjamin Wilk, Alyssa Barker and Lawrence Yip whom I have become great friends with and helped me to keep my sanity throughout my graduate training.

Thank you to all my friends who have supported me along the way during the long stretch of my doctoral training, and best of luck to Stefan Poirier, Josephine Tan, Fahad Hannan, Sawyer Badiuk, Nourhan Shalaby and, last but not least, Kate Onuska in their endeavors!

Finally, I would like to thank my parents Ying Xiang and Lin Qi who have sacrificed so much to provide me the opportunity to receive training at one of the finest research institutions in Canada. I am eternally indebted and grateful.

Table of Contents

Abstract.....	ii
Co-Authorship Statement.....	iv
Acknowledgments.....	vi
Table of Contents.....	viii
List of Tables.....	xiii
List of Figures.....	xiv
List of Appendices.....	xviii
Chapter 1.....	1
1 Introduction.....	1
1.1 Motivation and Overview.....	2
1.2 Glioblastoma Multiforme (GBM).....	4
1.3 Cancer cell metabolism and its pH environment.....	5
1.4 Magnetic resonance imaging.....	8
1.4.1 Chemical exchange saturation transfer.....	9
1.4.1.1 Glucose-CEST MRI.....	12
1.4.1.2 CEST with pH.....	14
1.4.1.3 Amine and amide concentration independent detection.....	15
1.4.1.4 AcidoCEST MRI.....	17
1.4.1.5 Simultaneously measuring pH_i and pH_e	20
1.4.2 Hyperpolarized $[1-^{13}\text{C}]$ pyruvate MRSI.....	22
1.5 Computed tomography perfusion.....	23
1.6 Positron emission tomography.....	25
1.6.1 PET basics.....	25
1.6.2 $[^{18}\text{F}]$ -Fluorodeoxyglucose.....	28

1.6.3 PET kinetic modeling	29
1.7 Objectives and Hypothesis.....	31
1.8 References.....	34
Chapter 2.....	37
2 Multimodality In Vivo Imaging of Perfusion and Glycolysis in a Rat Model of C6 Glioma.....	37
2.1 Introduction.....	37
2.2 Methods.....	39
2.2.1 C6 glioma model.....	40
2.2.2 CT-perfusion and analysis	40
2.2.3 FDG-PET imaging	41
2.2.4 Dynamic glucoCEST imaging	42
2.2.5 Hyperpolarized [1- ¹³ C]pyruvate MRSI.....	44
2.2.6 Benchtop blood glucose measurement.....	44
2.2.7 ROI selection and imaging registration	45
2.2.8 Statistical analysis.....	46
2.3 Results.....	46
2.3.1 Tumor size	46
2.3.2 Blood glucose measurement	47
2.3.3 Dynamic CEST MRI trends.....	49
2.3.4 Tumor vs. contralateral brain tissue.....	49
2.3.5 CEST vs. perfusion and glycolysis	51
2.3.6 Glycolysis vs. perfusion measurement	51
2.3.7 Expected vs. Unexpected group.....	53
2.4 Discussion.....	53
2.5 Conclusion	59

2.6	References.....	60
Chapter 3..... 65		
3	Glucose Infusion Induced Change in Intracellular pH and Its Relationship with Tumor Glycolysis in a C6 Rat Model of Glioblastoma	65
3.1	Introduction.....	65
3.2	Methods.....	66
3.2.1	Experiment design	66
3.2.2	C6 glioma model.....	66
3.2.3	FDG-PET imaging	67
3.2.4	Dynamic CEST imaging	67
3.2.5	Hyperpolarized [1- ¹³ C]pyruvate MRSI.....	69
3.2.6	Phantom preparation	69
3.2.7	Simulation	69
3.2.8	CEST imaging analysis.....	71
3.2.9	Estimation of pH _i using AACID	72
3.2.9	ROI selection and image registration.....	74
3.2.10	Statistical analysis.....	74
3.3	Results.....	75
3.3.1	AACID vs. pH from simulation.....	75
3.3.2	CEST signal at relevant metabolite resonant frequencies.....	76
3.3.3	AACID value vs. pH from phantom	77
3.3.4	Comparison among phantom and <i>in vivo</i> AACID values.....	78
3.3.5	pH _i change during glucose infusion.....	78
3.3.6	Tumor glycolysis measurements vs. <i>in vivo</i> pH _i	81
3.4	Discussion	82
3.5	Conclusion	87

3.6	References.....	88
Chapter 4.....		90
4	Evaluation of the Change in Tumor Intra-/Extracellular pH Environment Induced by Glucose Injection and its Relationship with Tumor Glycolysis in a C6 Rat Model of Glioblastoma	90
4.1	Introduction.....	91
4.2	Methods.....	92
4.2.1	Experiment design	92
4.2.2	C6 cell implantation.....	92
4.2.3	Benchtop blood glucose measurement.....	94
4.2.4	MR tumor check	94
4.2.5	FDG-PET	94
4.2.6	CEST MRI experiment	95
4.2.7	Kinetic analysis of FDG-PET	96
4.2.8	acidoCEST MRI phatom calibration	96
4.2.9	Tumoral and peritumoral pH_i , pH_e and pH gradient.....	98
4.2.10	Histology.....	98
4.2.10	Image registration and ROI selection	99
4.2.10	Statistical analysis.....	101
4.3	Results.....	101
4.3.1	Blood glucose measurement	101
4.3.2	Calibration of acidoCEST MRI to pH_e	102
4.3.3	The effect of glucose injection of pH_i and pH_e	103
4.3.4	Kinetic analysis results	104
4.3.5	Correlation between tumoral, peritumoral pH measurements and tumor glycolysis	105

4.3.6 Histological validation	106
4.4 Discussion	107
4.5 Conclusion	111
4.6 References.....	112
Chapter 5.....	115
5 Discussion and future directions	115
5.1 Chapter 2.....	115
5.2 Chapter 3.....	116
5.3 Chapter 4.....	117
5.4 Future directions	118
5.5 Conclusion	120
5.5 References.....	122
Appendices	126
Curriculum Vitae	129

List of Tables

Table 2.1: Pearson correlation coefficients between CT perfusion (BF, BV and PS), FDG-PET (SUV), hyperpolarized [$1-^{13}\text{C}$]pyruvate (Lac:Pyr) and glucoCEST (ΔCEST) measured in the tumor. * indicates P value < 0.05 .

Table 2.2: Pearson correlation coefficients between CT perfusion (BF, BV and PS), FDG-PET (SUV), hyperpolarized [$1-^{13}\text{C}$]pyruvate (Lac:Pyr) and glucoCEST (ΔCEST) measured in the tumor for the expected group. * indicates P value < 0.05 .

Table 2.3: Pearson correlation coefficients between CT perfusion (BF, BV and PS), FDG-PET (SUV), hyperpolarized [$1-^{13}\text{C}$]pyruvate (Lac:Pyr) and glucoCEST (ΔCEST) measured in the tumor for the unexpected group. * indicates P value < 0.05 .

Table 3.1: Parameters used for the 7-pool BM simulation.

Table 3.2: Range of AACID values from *in vivo* and phantom measurements.

Table 3.3: Pearson's correlation among tumor glycolysis measurements (SUV and Lac:Pyr) and tumor and peritumor baseline pH_i , pH_G and ΔpH_i induced by glucose infusion. The asterisk indicates a statistical significance of $P < 0.05$.

Table 4.1: Pearson's correlation among baseline tumor glycolysis measurements (MRGlu), tumor and peritumor pH environments (pH_i , pH_e and pH_G) and AUC_{MTR} . The asterisk indicates a statistical significance of $P < 0.05$.

Table 4.2: Pearson's correlation among tumor glycolysis measurement (MRGlu) and tumor and peritumor ΔpH (ΔpH_i and ΔpH_e) induced by glucose injection. The asterisk indicates a statistical significance of $P < 0.05$.

List of Figures

Figure 1.1: An illustrative figure of tumor metabolism. The majority of glucose transported into the cell will go through glycolysis and is converted into lactic acid. Lactic acid will be pumped out into the extracellular space leading to a more acidic pH_e versus a neutral or slightly basic pH_i .

Figure 1.2: A pictorial representation of proton exchange between a metabolite and its neighboring water, this exchange behavior occurs naturally. After the saturation of the metabolite proton is achieved by an on-resonance radiofrequency irradiation, the saturated proton can be exchanged with a water proton and in turn transfer the saturation to the water pool. The exchange rate from metabolite to the water pool is denoted as k_{XB} and the reverse exchange rate is denoted as k_{BX} . The proton in red denotes the saturated proton, and the proton in black denotes the unsaturated protons.

Figure 1.3: An illustrative figure of Z-spectrum in blue and its associated MTR_{asym} spectrum in red for a biological system containing glucose. The shaded orange area represents the AUC for MTR_{asym} spectrum, and it is related to the concentration of glucose molecules.

Figure 1.4: Two anomeric forms of D-glucose, 4 resonant frequencies at 0.66, 1.28, 2.08 and 2.88 ppm are associated with these two forms of D-glucose.

Figure 1.5: Illustrative simulation results of a 3-pool model on the top row (a-c) and a 7-pool model in the bottom row (d-f). The resultant Z-spectra (a) along with their corresponding MTR_{asym} spectra (b) and the AACID values at their associated pHs (c) in a biological system without the presence of glucose. When glucose is added to the system, the simulation results for the Z-spectra (d), corresponding MTR_{asym} spectra (e) and the AACID values at their associated pHs (f) are shown above. The dotted lines in panel c) and f) denoted the line of best fit.

Figure 1.6: The chemical structure of iopamidol, the 2 amide functional groups provide proton exchange sites (in red) with neighboring water.

Figure 1.7: Illustrative simulation results of a 3-pool model on the top row (a-c) and a 7-pool model in the bottom row (d-f). The resultant Z-spectra (a) along with their corresponding MTR_{asym} spectra (b) and the R_{ST} at their associated pH values (c) in a biological system without the presence of glucose. When glucose is added to the system, the simulation results for the Z-spectra (d), corresponding MTR_{asym} spectra (e) and the R_{ST} at their associated pHs (f) are shown above. The dotted lines in panel c) and f) denoted the line of best fit.

Figure 1.8: An illustrative simulation result of a 9-pool exchange model: the Z-spectra and their corresponding MTR_{asym} spectra at different pHs are shown in a) and b) respectively. pH vs. AACID and R_{ST} are plotted in c) and d) respectively.

Figure 1.9: Schematic of detecting coincidence events for two detectors. Signal 1 from Detector 1 results in a trigger pulse 1 which sets the start of check the coincidence window. Signal 2 from Detector 2 results in a trigger pulse 2. A coincidence circuit will check for

coincidence between the pulse 2 and pulse 1 ($\Delta t = t_2 - t_1$) and the coincidence window (timing resolution).

Figure 1.10: a) The chemical structure and of ^{18}F -FDG and its metabolism after entering the cell. It will go through the first step of glycolysis and be phosphorylated to ^{18}F -FDG-6-P and trapped inside the cell. b) A schematic of 2T3C for ^{18}F -FDG, $C_p(t)$ represent the radioactivity in the plasma as a function of time, $C_{ND}(t)$ represents the activity of free ^{18}F -FDG after entering the brain but before entering into the cells as a function of time. $C_S(t)$ represents the activity as function of time after ^{18}F -FDG enters the cell and later trapped inside the cell.

Figure 2.1: a) Study overview. Day 0 corresponds to the tumor cell implantation. A CT perfusion check was performed on Day 7 to monitor if the tumor had reached optimal size (diameter > 4 mm). An FDG-PET acquisition followed by CT perfusion experiment was carried out between Days 11 and 13. The glucoCEST experiment and hyperpolarized ^{13}C -pyruvate MRSI took place on the following day (Days 12 to 14). b) Dynamic CEST experiment. There were three CEST acquisitions: a baseline CEST acquisition (Pre), a second CEST acquisition during the first 30 minutes of glucose infusion (During 0-30 min) and a final CEST acquisition during the last 30 minutes of glucose infusion (During 30-60 min).

Figure 2.2: Example images and ROIs in a single rat. A T_2 -weighted 9.4 T MR image (T2W) was used as a reference to co-register CT perfusion maps (BF, BV, PS), FDG-PET, CEST maps (AUC_{MTR}), and hyperpolarized $[1-^{13}\text{C}]$ pyruvate MRSI (Lac:Pyr). The T2W image was subsequently used to delineate tumor (red dotted line) and contralateral brain tissue (blue dotted line), with the same ROI applied to all imaging measurements.

Figure 2.3: Average tumor size on first imaging day for PET and CT perfusion experiment and the next day for glucoCEST and hyperpolarized $[1-^{13}\text{C}]$ pyruvate. No statistical significance in tumor size were found between these two subsequent imaging days ($P = 0.54$). Error bars = standard deviation.

Figure 2.4: An illustrative example of blood glucose change during the 60-min constant infusion. Time 0 was defined as the time at the start of constant infusion of 20% glucose solution (1.5 g/kg) and after a bolus of 20% glucose solution (0.3 g/kg) was injected.

Figure 2.5: Illustrative examples of two different trends observed from the dynamic glucoCEST measurements: a) expected and b) unexpected change in AUC_{MTR} . The expected trend was observed in 5 subjects and is shown in c), where during-infusion AUC_{MTR} values are significantly higher than pre-infusion AUC_{MTR} . The unexpected trend was observed in 6 subjects and is shown in d), where during-infusion AUC_{MTR} is significantly lower ($n = 5$, grey-dotted line) than or is not significantly different ($n = 1$, red line, $P = 0.46$) from pre-infusion AUC_{MTR} . Error bars = standard deviation.

Figure 2.6: Mean values from ROIs defined in both tumor and contralateral brain tissue in CT perfusion maps (a) BF, b) BV and c) PS), d) FDG-PET (SUV), e) hyperpolarized $[1-^{13}\text{C}]$ pyruvate (Lac:Pyr) and f) glucoCEST (ΔCEST). A statistically significant ($P < 0.05$)

difference was found in BV, PS, SUV and Lac:Pyr between tumor and contralateral brain. No statistically significant difference was found in BF and Δ CEST between tumor and contralateral brain tissue. Error bars = standard deviation.

Figure 2.7: Mean values from ROIs defined in both tumor and contralateral brain tissue in AUC_{MTR} pre- and during-infusion (30-60 min). A statistically significant ($P < 0.05$) difference was found between tumor and contralateral side in AUC_{MTR} pre- and during glucose infusion.

Figure 2.8: Δ CEST vs. blood volume (a) and permeability-surface area product (b). Tumor SUV vs. blood flow (c) and permeability-surface area product (d). Tumor Lac:Pyr vs. blood volume (e) and permeability-surface area product (f). Solid line indicates the best fit and the dotted lines denote 95% confidence interval. Error bar = standard deviation.

Figure 2.9: Good colocalization of the tumor region is displayed in AUC_{MTR} and PS maps. Similarly, co-localization of potential necrosis is shown among AUC_{MTR} , BF and BV maps (red arrow).

Figure 3.1: The relationship between pH and AACID value from phantom measurements are plotted at glucose concentrations of 2.5 (a), 4.5 (b), 6 mmol/L (c) and combined (d). The lines of best fit are represented by the dotted line; the fitting equations, the one-way ANOVA result and the goodness-of-fit are shown at the top right corner of each plot. The error bars denote the standard deviation of AACID values from all pixels for individual tube.

Figure 3.2: The relationship between pH and AACID value from simulation using the 7-pool exchange model are plotted at glucose concentrations of 2.5 (a), 4.5 (b) and 6 mmol/L (c). The lines of best fit are represented by the dotted line, and the fitting equations and the goodness-of-fit are shown at the top right corner of each plot.

Figure 3.3: MTR_{asym} maps of phantom (6 mM) at the four main resonant frequencies of glucose as well as the amine and amide resonance frequencies.

Figure 3.4: The average pH_i before and during glucose infusion at tumoral, peritumoral and contralateral brain regions. The asterisk denotes the significant difference ($P < 0.05$), and the error bars denote the standard deviation.

Figure 3.5: An illustrative example of registered pH_i maps (pre- and during-infusion), FDG-PET and Lac:Pyr maps overlaid on T_2 -weighted MRI. Tumor, peritumor and contralateral brain regions are delineated by red-, beige- and blue-dotted lines, respectively.

Figure 3.6: The relationship between tumor Lac:Pyr and tumor baseline pH_i (a) peritumor baseline pH_i (b), tumoral ΔpH_i (c); and peritumoral ΔpH_i (d). Dotted lines indicate the 95% confidence interval, and the error bar denotes the standard deviation.

Figure 3.7: The relationship between tumor Lac:Pyr vs. pHG_i pre-infusion. Dotted lines indicate the 95% confidence interval, the error bar = standard deviation.

Figure 3.8: The Z-spectra from the phantom experiment and the Lorentzian fitting of the glucose peak at 2.18 ppm. The FWHM and amplitude increase as the pH increases from 6.2 to 7.4.

Figure 4.1: **a)** Study overview, Day 0 denotes the day of C6 glioma cell implantation. An MR tumor check took place on Day 7. The FDG-PET experiment was carried out on Day 11, with follow up CEST experiment on the morning of the next day (within 24 hours). **b)** Simultaneous AACID and acidoCEST experimental design. A bolus (0.05 ml) followed by the start of a constant infusion (3.3 gI/kg over 44 minutes) of 300 mgI/ml of iopamidol took place prior to the start of the CEST acquisition. A baseline CEST acquisition took place before the bolus injection of 20% D-glucose (0.3 g/kg), followed by another post-injection CEST acquisition.

Figure 4.2: pH_e vs. MTR_{asym} values at the resonance frequencies of the exchange protons on the two amide functional groups on iopamidol without **a.** and with **b.** the presence of glucose (6 mM). **c** pH_e vs. the corresponding R_{ST} value calculated using acidoCEST measurements obtained from the phantom experiments. Error bar = standard deviation.

Figure 4.3: Illustrative example of all registered images and ROIs for one rat. T_2 -weighted MRI acquired on the 9.4 T MRI is used as a reference to co-register CEST MRIs (**a**, **b**, **e** and **f**), FDG-PET images (**c** and **g**) and the corresponding H & E images with different magnifications (**d** and **h**). The tumor, peritumor and contralateral brain regions are delineated using the T_2 -weighted MRI with the red-, beige- and blue-dotted lines respectively.

Figure 4.4: Illustrative example of all registered images and ROIs for another rat. T_2 -weighted MRI acquired on the 9.4 T MRI is used as a reference to co-register CEST MRIs (**a**, **b**, **e**, **f** and **g**), FDG-PET images (**c** and **d**) and the corresponding H & E image (**h**). The tumor, peritumor and contralateral brain regions are delineated using the T_2 -weighted MRI with the red-, beige- and blue-dotted lines respectively. The red arrows indicate a potential co-localization of tumor necrosis between CEST MRI and histology.

Figure 4.5: An illustrative example of blood glucose changes 30 minutes after an injection of a bolus of 20% glucose-saline solution (0.3 g/kg of the rat).

Figure 4.6: Mean values from ROIs defined in tumor, peritumor and contralateral brain tissue in pH_i (**a**) and pH_e (**b**) at baseline and post-injection. Error bar = standard deviation.

Figure 4.7: Mean MRGlu measurement in the tumor, peritumor and contralateral brain regions. The error bar = standard deviation.

Figure 4.8: Tumor glycolytic measurement of MRGlu vs. tumor pH_i **a**, tumor pH_e **b**, tumor ΔpH_e **c**, and tumor ΔpH_i vs. peritumor ΔpH_e **d**. The dotted line indicates the 95% confidence interval, and the error bar denotes the standard deviation.

List of Appendices

Appendix A: Animal use protocol for Chapter 2, 3 and 4.

Appendix B: Copyright for Chapter 2: Multimodality In Vivo Imaging of Perfusion and Glycolysis in a Rat Model of C6 Glioma.

List of Acronyms

AACID: amine amide concentration independent detection

AcidoCEST: acido chemical exchange saturation transfer

ADP: adenosine diphosphate

AIF: arterial input function

ADC: analog-to-digital converter

ATP: adenosine triphosphate

AUC: area under the curve

B_0 : main magnetic field strength of MR

B_1 : radiofrequency magnetic field strength of MR

BF: blood flow

BV: blood volume

CEST: chemical exchange saturation transfer

CNS: central nervous system

CO₂: carbon dioxide

CSF: cerebrospinal fluid

CT: computed tomography

CTP: computed tomography perfusion

FDG: fluorodeoxyglucose

FDG6P: fluorodeoxyglucose-6-phosphate

FOV: field of view

GBM: glioblastoma multiforme

GCE: glucose contrast enhancement

GlucoCEST: glucose chemical exchange saturation transfer

H^+ : hydrogen proton

IRF: impulse residue function

Lac:Pyr: lactate-to-pyruvate ratio

LC: lumped constant

k_a : rate constant for the acid-catalyzed proton exchange

k_b : rate constant for the base-catalyzed proton exchange

k_{ex} : equilibrium exchange rate

k_i : influx constant

MCA: multichannel analyzer

MCT: monocarboxylate- H^+ efflux transporter

MRGlu: metabolic rate of glucose

MRI: magnetic resonance imaging

MRSI: magnetic resonance spectroscopy imaging

MTR_{asym} : magnetization transfer ratio asymmetry

PET: positron emission tomography

pH_e : extracellular pH

pH_i : intracellular pH

pHG: pH gradient across intra- to extracellular space

pHG_i : intracellular pH gradient from tumor to peritumor region

ppm: parts per million

PS: permeability area surface-area product

SUV: standardized uptake value

TAC: time-activity curve

TE: echo time

TR: repetition time

T₁: longitudinal relaxation time

T₂ : transverse relaxation time

2T3C: 2-tissue 3-compartment

Chapter 1

1 Introduction

This thesis explores the intrinsic relationship between cancer perfusion and cancer metabolism as well as the effect of tumor metabolism on tumor pH environments. We first evaluated whether glucose chemical exchange saturation transfer (glucoCEST) magnetic resonance imaging (MRI) is a perfusion or glycolysis measurement. In Chapter 2, we compared glucoCEST to perfusion measurements from computed tomography perfusion (CTP), and glycolysis measurements of standardized uptake value (SUV) from ^{18}F -fluorodeoxyglucose (FDG) positron emission tomography (PET) imaging and lactate-to-pyruvate ratio (Lac:Pyr) from hyperpolarized [$1\text{-}^{13}\text{C}$]pyruvate MR spectroscopy imaging (MRSI). In Chapter 3, we compared the tumor intracellular pH (pH_i) environment measured using amine and amide concentration independent detection (AACID) to tumor glycolysis measurement of SUV and Lac:Pyr. Finally, in Chapter 4, we compared both the tumor pH_i and extracellular pH (pH_e) environments to tumor glycolysis measurements obtained from dynamic FDG-PET. The purpose of this chapter is to provide an introduction and motivation for the presented research. Section 1.1 outlines the motivation and general organization of the thesis. A brief survey of glioblastoma multiforme, tumor metabolism and its pH environment is presented in Sections 1.2 and 1.3. An introduction to CEST theory and application to pH measurement is presented in Section 1.4 followed by discussion of PET imaging and PET analysis in Section 1.5. A brief discussion of CTP theory is in Section 1.6 and hyperpolarized [$1\text{-}^{13}\text{C}$]pyruvate MRSI is in Section 1.7.

1.1 Motivation and overview

Cancer cells have a complex microenvironment that helps to create optimal conditions for cancer proliferation. Nutrients such as glucose pass through a tortuous and leaky vascular structure developed by cancer cells, are distributed, and then transported inside the cancer cells to meet their metabolic demands. This leaky vasculature leads to a buildup in the

interstitial fluid pressure surrounding the tumor, which, along with the poorly organized vasculature, results in tumor hypoxia [1,2]. In the 1920s, Dr. Warburg and his colleagues discovered that cancer cells rely on glycolysis as their main source of energy production [3,4]. Cancer cells will upregulate glucose transporters and rely on glycolysis for energy production even with sufficient oxygen supply (known as aerobic glycolysis) [3,5]. Anaerobic glycolysis taking place in the cell cytosol is a less efficient means of energy production in contrast with oxidative phosphorylation (or PCA cycles) which takes place in the mitochondria. This is evident by comparing the number of adenosine triphosphate (ATP) produced at the end of each process, with 2 ATP produced from glycolysis and 38 ATP from the Krebs cycle. In fact, the majority of glucose will be converted into lactic acid via anaerobic glycolysis [4,6]. The reason behind this selective energy production method is still highly debated but it is widely believed that this is the result of evolution for cancer cell proliferation as the side products (proteins and enzymes) produced through glycolysis will aid in cancer cell proliferation [3]. As a consequence of the upregulation of glucose transporters and overreliance on glycolysis, elevated protons and acids are produced (as shown in **Figure 1.1**), resulting in a more acidic microenvironment for cancer cells. However, a lower pH environment would normally lead to intracellular acidosis which could eventually result in cell death or apoptosis. To avoid cell death, cancer cells, in turn, upregulate transporters (such as monocarboxylate-H⁺ efflux transporters) responsible for transporting acid and protons from the intracellular space to the extracellular space, and eventually achieve a pH gradient across the cell membrane i.e. a slightly more basic pH_i environment in combination with a more acidic pH_e environment and contributes to immune-resistance [7–9]. The acidic pH_e further contributes to tumor invasion to surrounding cells by damaging the extracellular matrix [4,7,8]. The relationship between cancer perfusion, metabolism and its pH environment are intricate and often closely interlinked. By evaluating their relationship, we can provide insight into tumor proliferation and potentially achieve a better treatment outcome. This thesis therefore aims to explore these intrinsic relationships and better understand the tumor microenvironment *in vivo* using a multimodal imaging approach.

1.2 Glioblastoma Multiforme (GBM)

Glioblastoma multiforme (GBM) is the most malignant type of brain tumor. It has an incidence of 4 per 100,000 people in Canada, and accounts for 12-15% of all intracranial tumors and 50-60% of astrocytic tumors [10]. Despite the advances in treatment modalities, including aggressive treatment methods combining surgery, chemotherapy, and radiotherapy, it remains largely incurable and has a low survival rate [10].

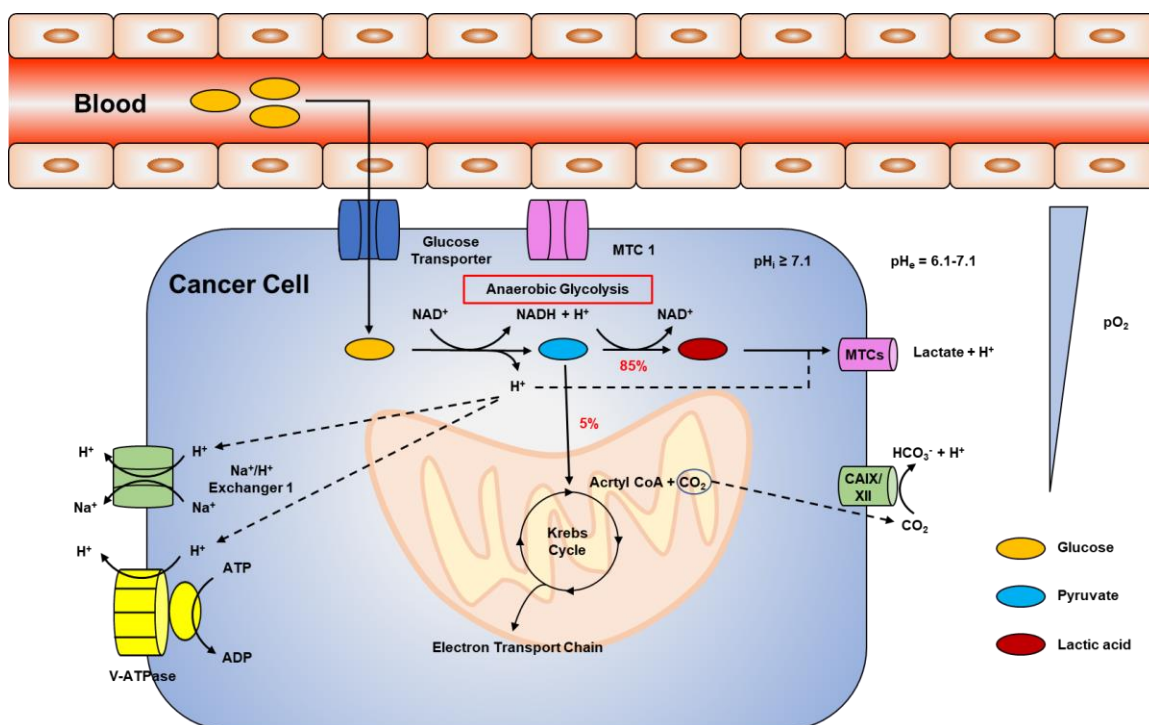


Figure 1.1: An illustrative figure of tumor metabolism. The majority of glucose transported into the cell will go through glycolysis and is converted into lactic acid. Lactic acid will be pumped out into the extracellular space leading to a more acidic pH_e versus a neutral or slightly basic pH_i.

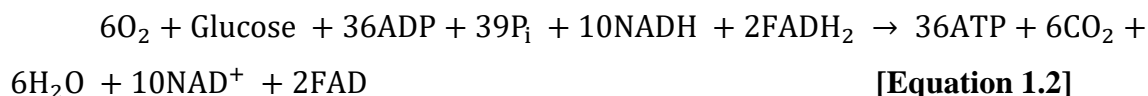
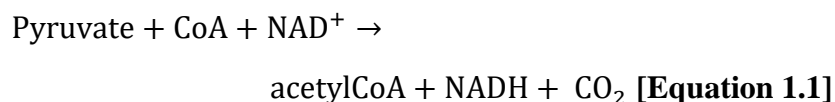
Glioma cells are cancer cells derived from glial cells, a type of non-neuronal cell that supports and protects neurons while also maintaining homeostasis in the central nervous system (CNS). The exact origin of glioma cells still remains uncertain, as neural stem cells, astrocytes and oligodendrocytes are all considered as possible precursors of glioma cells [11]. Astrocytoma is the most common type of glioma [12], and anaplastic astrocytoma, with a high degree of anaplasia, can infiltrate normal brain tissue diffusively and tends to

progress into GBM [13]. GBM is the most aggressive form of astrocytoma, and is made up of differentiated neoplastic astrocytes [14]. Elevated mitotic activity, angiogenesis and necrosis are regarded as hallmarks for GBM [14,15]. These are reflected by the complex metabolic and perfusion properties of GBM.

C6 cell lines were first developed in adult Wistar rat composing pleomorphic cells with distinctly shaped nuclei [16]. C6 glioma cells are spindle-like cells that possesses high similarity with human GBM, C6 rat model of glioma has also shown to be more superior than other rodent glioma models in terms of morphological characteristics [17,18]. C6 glioma cell implantation models have been developed using Wistar rats and the histological results have reflected similar features as human GBM i.e. with large necrosis and high mitotic index [19]. As a result, we used a C6 Wistar rat model of glioma in this thesis. However, C6 glioma cells might induce immune response mimicking certain anti-tumor response [20], therefore, the efficacy of immunotherapy should be carefully interpreted when using C6 glioma cells.

1.3 Cancer cell metabolism and its pH environment

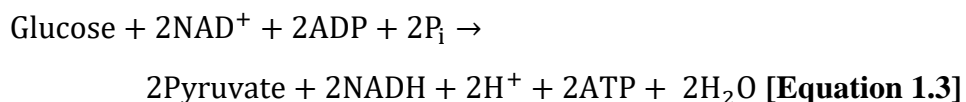
Glucose is the most important source for cellular energy production. In normal mammalian cells, glucose is used for an efficient energy production called the Krebs cycle and subsequent electron transport chain reactions under sufficient oxygen supply that takes place in the mitochondria inside of the cells. **Equation 1.1** indicates the reaction which connects glycolysis and the Krebs cycle. **Equation 1.2** indicates the overall energy production via the Krebs cycle [21].



where NAD^+ is nicotinamide adenine dinucleotide, CoA is coenzyme A, Acetyl-CoA is acetyl coenzyme A, NADH is the reduced form of NAD^+ , ADP is adenosine diphosphate

and ATP is adenosine triphosphate, FADH_2 is flavin adenine dinucleotide, FAD is flavin mononucleotide.

However, cancer cells mainly rely on the process of glycolysis (known as the Warburg effect) regardless of the surrounding oxygen environment, as shown in **Equation 1.3** and **Figure 1**, for energy production:



where ADP is adenosine diphosphate and P_i is inorganic phosphate.

Although glycolysis is a less efficient energy producing pathway compared to the Krebs cycle (producing only 2 ATP vs. 36 ATP produced in the Krebs cycle), cancer cells rely on glycolysis to create an optimal environment for them to proliferate, avoid detection from immune cells and avoid apoptosis [4,22]. As a result of this dependency on glycolysis, more H^+ protons and lactic acids are produced as by-products. They are transferred out of the cells to the extracellular space via proton and acid transporters such as monocarboxylate transporters (MCTs) to avoid apoptosis induced by intracellular acidosis [23]. As a result, a neutral pH or slightly alkaline pH environment is established in the intracellular space ≥ 7.1 [4,6,24,25], along with a slightly acidic extracellular pH environment ranging from 6.7 to 7.1 [4,22,25,26].

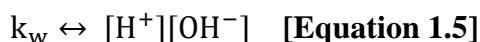
pH homeostasis is essential for the survival of human biological systems, with several systems involved simultaneously to ensure the proper pH balance is maintained. In metabolically active cells, the lactate and H^+ are side products from aerobic glycolysis and Krebs cycles and will accumulate in the intracellular space. The lactate and H^+ would lead to acidosis which will lead to apoptosis in the intracellular space of cells if left alone. As a result, transporters such as MCTs are activated after a more acidic intracellular environment is detected and facilitate transportation of the acid to the extracellular space. The acid will then be transported to the blood stream and neutralized by the liver and kidney. As a result, the system will maintain pH homeostasis to avoid cell damage in both the intra- and extracellular space. However, in the case of cancer cells, due to the over-reliance on glycolytic metabolism (Warburg effect), an excess amount of acid and H^+ are

produced by glycolysis in the cytosol. In combination with the poor perfusion environment from a tortuous vasculature established by cancer cells and the elevated number of proton transporters, a greater reduction in local pH will be induced.

Ionization or dissociation of water molecules to H^+ and OH^- occurs naturally:



This self-ionization process of water is reversible, and at equilibrium the activity of the dissociation process is defined as the product of the molar concentrations of the ions, symbolized by the ionization constant k_w .



Where $[H^+]$ and $[OH^-]$ are the molar concentrations of the ions.

Danish chemist Søren Peter Lauritz Sørensen introduced the concept of pH to measure the acidity or alkalinity in an aqueous solution [27]. pH is a logarithmic measurement, and it inversely indicates the concentration of H^+ in an aqueous solution as shown in **Equation 1.6**.

$$pH = -\log_{10}[H^+] \quad \text{[Equation 1.6]}$$

In the pH scale at 25 °C, a solution with pH less than 7 is regarded as acidic, pH of 7 is defined as neutral, and a pH greater than 7 is considered as basic. If intra- and extracellular $[H^+]$ can be measured in the biological tissue, the pH_i and pH_e can in turn be calculated using **Equation 1.6**.

Traditionally, pH values have been measured using microelectrodes based on a difference in potentials between the two electrodes [28]. pH can also be measured via positron emission tomography (PET), magnetic resonance spectroscopy imaging (MRSI) and immunohistochemistry [8,9,29]. However, these methods are either invasive or possess limited spatial resolution. Novel MRI imaging techniques provide the possibility of measuring the *in vivo* pH environments non-invasively and with high-resolution.

1.4 Magnetic Resonance Imaging

Magnetic resonance imaging (MRI) is a diagnostic imaging tool that is widely used in the clinical setting. It is able to image the magnetic dipole moment of hydrogen (H^+) as it interacts with the environment under a magnetic field. In an external magnetic field (B_0) the magnetic dipole moment will precess around the direction of B_0 at the Larmor frequency:

$$\omega_0 = \gamma B_0 \text{ [Equation 1.7]}$$

where γ is the gyromagnetic ratio associated with magnetic dipole moment of the corresponding proton.

Chemical shift is the resonant frequency of a nucleus relative to a standard in a magnetic field, and it is normally expressed in δ or $\Delta\omega$ with the unit of parts per million (ppm).

$$\text{ppm} = \frac{\text{Hz}}{\text{MHz}} \text{ [Equation 1.8]}$$

For CEST MRI, the water resonance frequency is used as a reference and assigned a value of 0 ppm [30,31], whereas in proton MRS the water resonant frequency is normally assigned at 4.75 ppm, and the reference at 0 ppm is tetramethylsilane [32–34].

1.4.1 Chemical exchange saturation transfer (CEST)

Chemical exchange saturation transfer (CEST) was first developed by Balaban and colleagues in 2000 [35]. It is based on the proton exchange between metabolites with low proton concentration (on the order of μM to mM) and the neighboring water pool which possesses a much larger proton concentration ($\sim 110 \text{ M}$) as shown in **Figure 1.2**. This exchange behavior occurs naturally, and the exchange rate from the metabolite to water is denoted as k_{XB} , where pool B is the water pool and pool x is the pool associated with the metabolite. Inversely, the proton exchange rate from the water pool to the metabolite is denoted as k_{BX} . Due to the significant difference in proton concentration between the metabolite pool and the water pool, the equilibrium exchange rate $k_{\text{ex}} = k_{XB} + k_{BX} \approx k_{XB}$.

To effectively detect signals using CEST, the metabolites of interest should have a slow to intermediate exchange regime with the equilibrium exchange rate (k_{ex}) $\leq \Delta\omega$ [30,31,36].

When a radiofrequency (RF) pulse is applied at the resonant frequency of the exchanging proton on the metabolite, saturation of the associated proton on the metabolite will be achieved and can be detected on the proton spectrum. The saturated proton from the metabolite can exchange with an unsaturated proton from the neighboring water pool, resulting in the saturation being transferred to the water pool. After applying the RF pulse for a certain amount of time (t_{sat}) the exchange will reach saturation (S_{sat}). This enables the indirect detection of endogenous or exogenous metabolites by measuring the signal saturation from proton exchange observed as a decrease in water signal after the exchange

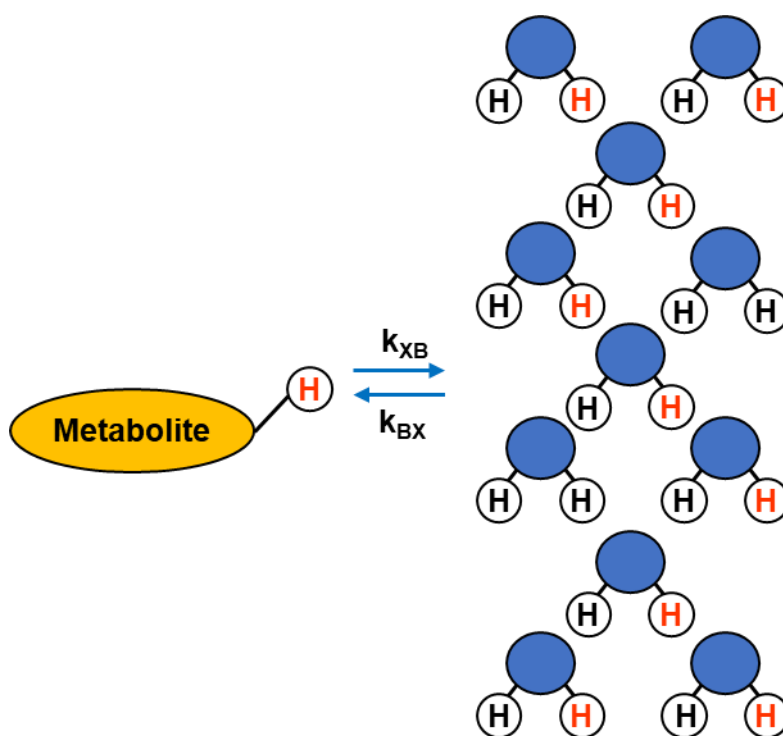


Figure 1.2: A pictorial representation of proton exchange between a metabolite and its neighboring water, this exchange behavior occurs naturally. After the saturation of the metabolite proton is achieved by on-resonance radiofrequency irradiation, the saturated proton can be exchanged with a water proton and in turn transfer the saturation to the water pool. The exchange rate from metabolite to the water pool is denoted as k_{XB} and the reverse exchange rate is denoted as k_{BX} . The protons in red denote the saturated protons, and the protons in black denote the unsaturated protons.

reaches saturation. The CEST or Z-spectrum is widely used to quantify metabolite CEST signals, it is plotted as the normalized magnetization of water (S_{sat}/S_0 , S_0 denotes the unsaturated signal) as a function of saturation offset ($\Delta\omega$). The magnetization transfer ratio asymmetry (MTR_{asym}) is used to minimize direct saturation on water proton as its effect is symmetrical with respect to the water saturation frequency (assigned as 0 ppm) as shown in **Equation 1.9**. It is important to note that the effect of magnetization transfer (MT) might not be symmetrical around the water peak for some CEST agents such as diamagnetic CEST (DIACEST) agents [37]. In addition, the nuclear overhauser effect (NOE) is also not symmetrical around the water peak [38], which can also contaminate the measurement of MTR_{asym} . However, it is still useful when comparing the difference between pre- and post-contrast assuming the effects on MT and NOE are constant [39]. The area under the curve (AUC) for the MTR_{asym} spectrum is associated with the concentration of the metabolite of interest within the range of its resonant frequencies. An illustrative example of a Z-spectrum and its corresponding MTR_{asym} spectrum can be found in **Figure 1.3**.

$$\text{MTR}_{\text{asym}} = \frac{S_{-\Delta\omega} - S_{\Delta\omega}}{S_0} \quad \text{[Equation 1.9]}$$

Where $S_{-\Delta\omega}$ and $S_{\Delta\omega}$ are the proton signals at $-\Delta\omega$ and $\Delta\omega$ respectively.

The Bloch-McConnell equation is commonly used to describe the proton exchange effect [40] as shown by **Equation 1.10**:

$$\frac{d\mathbf{M}}{dt} = \mathbf{A}\mathbf{M} + \mathbf{C} \quad \text{[Equation 1.10]}$$

with an analytical solution [40]:

$$\mathbf{M} = (\mathbf{M}_0 + \mathbf{A}^{-1}\mathbf{C})e^{\mathbf{A}t} - \mathbf{A}^{-1}\mathbf{C} \quad \text{[Equation 1.11]}$$

where \mathbf{M} is magnetization vector with dimensions that best describe the case-specific proton-exchange models, \mathbf{M}_0 is the thermal equilibrium magnetization vector, \mathbf{A} is a block matrix of associated coefficients for the solution and \mathbf{C} is a constant vector for the solution.

1.4.1.1 GlucoCEST

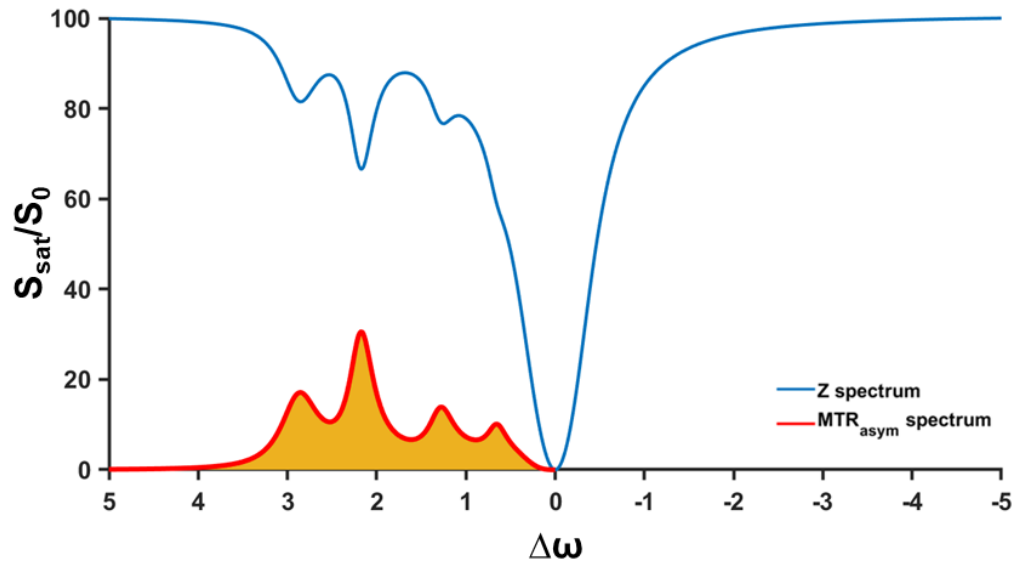


Figure 1.3: An illustrative figure of the Z-spectrum in blue and its associated MTR_{asym} spectrum in red for a biological system containing glucose. The shaded orange area represents the AUC for MTR_{asym} spectrum, and it is related to the concentration of glucose molecules.

CEST MRI can indirectly detect metabolites at low concentration via the proton exchange regime between the metabolites and water as mentioned above. D-glucose, the naturally occurring form of glucose molecules [41], is used as a primary energy source in most cancer types [3] and can be detected using CEST MRI *in vivo*.

In solution, D-glucose possesses two anomeric forms, α (36%) and β (64%) [41] as shown in **Figure 1.4**.

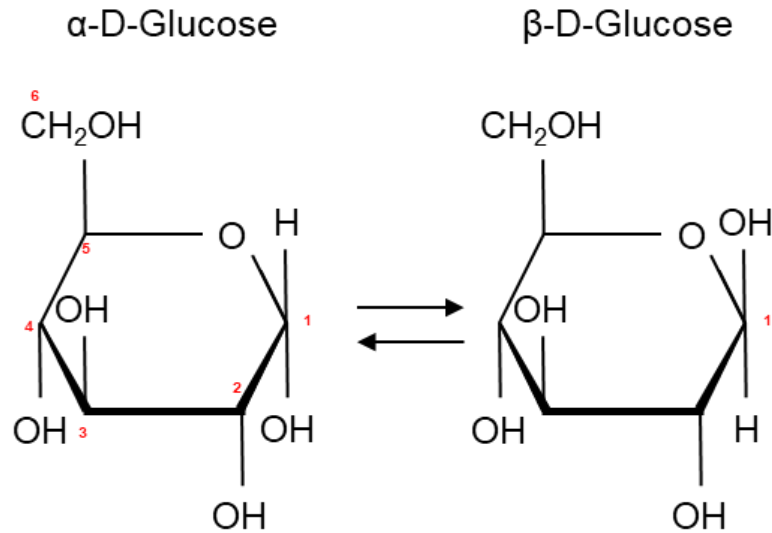


Figure 1.4: Two anomeric forms of D-glucose. Four resonant frequencies at 0.66, 1.28, 2.08 and 2.88 ppm are associated with these two forms of D-glucose.

Both configurations have a chemical shift from water of 0.66 ppm for the proton on the -OH on the 6th carbon atom; chemical shifts of 1.28 ppm for the protons on the 3 -OH groups at the position of 2, 3 and 4; and chemical shifts of 2.08 (α) or 2.88 (β) ppm for the proton on the hydroxyl group at position 1 depending on the anomeric forms. Chemical shift is independent of pH and temperature, therefore, 4 chemical shifts at 0.66, 1.28, 2.08 and 2.88 ppm can be detected from D-glucose molecules using CEST MRI as shown in **Figure 1.3**.

Two strategies have been developed to utilize D-glucose as a contrast agent for CEST MRI, either by measuring endogenous glucose or using D-glucose as a contrast agent to achieve glucose contrast enhancement (GCE) [42–44]. The *in vivo* glucoCEST signals are mainly derived from the endogenous glucose molecules present in the interstitial or extracellular space [43,45]. A Z-spectrum that consists of all resonant frequencies associated with the glucose molecule will be acquired. The corresponding MTR_{asym} will be derived, and the AUC will be calculated to represent the concentration of glucose. This has been used to monitor the immunotherapy treatment response targeting tumor glycolytic metabolism such as treatment with a mammalian target of Rapamycin inhibitor (rapamycin) [46]. GCE CEST requires an injection or infusion of D-glucose solution, and it has been used to

investigate tumor perfusion such as tumor blood flow and vascular permeability [42,45,47,48]. GCE is quantified by comparing the difference between post/during-infusion and pre-infusion MTR_{asym} spectra. Some groups have also proposed that it could be used to measure tumor metabolism [43,49].

1.4.1.2 CEST with pH

CEST MRI is based on the process of proton exchange. k_{ex} is pH sensitive and the effect of pH on k_{ex} can be generalized by **Equation 1.12a and 1.12b**:

$$\begin{aligned} k_{\text{ex}} &= k_a[\text{H}^+] + k_b[\text{OH}^-] + k_0 \text{ [Equation 1.12a]} \\ &= k_1 \cdot 10^{\text{pH}-7} + k_0 \text{ [Equation 1.12b]} \end{aligned}$$

where k_0 is rate constant for spontaneous proton exchange between water and the exchangeable proton on the metabolite, k_a is the rate constant for the acid-catalyzed proton exchange and k_b is the rate constant of the base-catalyzed proton exchange between water and metabolites with exchangeable protons and can be generalized by **Equation 1.12b** for base-catalyzed exchanges. k_{ex} will affect the magnitude of CEST as shown by the generalized analytical solution for the Bloch-McConnell equation [36,40,50]:

$$Z(\Delta\omega, t) = (P_{z\text{eff}}P_z Z_i - Z^{\text{ss}}(\Delta\omega))e^{-R_{1\rho}(\Delta\omega)t} + Z^{\text{ss}}(\Delta\omega) \text{ [Equation 1.13]}$$

$$Z^{\text{ss}}(\Delta\omega) = P_z \frac{R_1}{R_{1\rho}(\Delta\omega)} \text{ [Equation 1.14]}$$

where P_z is the projection factor on the z-axis of the rotating frame; P_{eff} is the projection factor on the z-axis of the effective frame, $P_z = P_{\text{eff}} \approx \cos\theta$, θ is the flip angle of the preparation pulse before and after continuous wave irradiation; Z_i is the initial Z-magnetization ($Z_i = M_i/M_0$); Z^{ss} is the steady-state Z-spectrum signal; and $R_{1\rho}$ is the longitudinal relaxation rate in the rotating frame ($R_{1\rho} = 1/T_{1\rho}$).

$$R_{1\rho}(\Delta\omega) = R_{\text{eff}} + f_b k_{\text{ex}} \frac{\omega_1^2}{\omega_1^2 + k_{\text{ex}}(k_{\text{ex}}^{-1} + R_{2b})} \text{ [Equation 1.15]}$$

R_{eff} is water proton relaxation rate in the rotating frame, f_b is the relative population fraction ($f_b = M_{0,b}/M_{0,a}$). [36,40,50].

In general, CEST can estimate the pH environment in which the proton exchange process takes place either by performing a phantom experiment to relate the CEST signal with the corresponding pH [31,51,52], or by isolating k_{ex} using an Omega plot derived from an experiment with varying B_1 [53]. However, proton exchange detected using CEST is a delicate process and can be affected by other factors such as temperature, solute proton concentration, amplitude of B_1 and the relaxation time constants for the bulk water (T_1 and T_2) [30,31].

1.4.1.3 Amine and amide concentration independent detection

(AACID)

Amine and amide concentration independent detection (AACID) was developed by exploiting the change in the exchange rate of amine and amide protons due to change in pH_i [51,54,55]. Endogenous amide and amine metabolites can be found in the intracellular space, and the proton exchange can be captured using CEST. Their signals can be seen on the Z-spectra or MTR_{asym} spectra at 3.5 and 2.75 ppm in an illustrative example as shown in **Figure 1.5a** and **b**. The k_{ex} for protons of amine and amide can be described using **Equation 1.16** and **Equation 1.17** [51]:

$$k_{amine} = 10^{pH-4.2} \text{ [Equation 1.16]}$$

$$k_{amide} = 5.75 \times 10^{pH-6.4} \text{ [Equation 1.17]}$$

A general analytical solution can be used to satisfy the Bloch-McConnell equation as mentioned above, and a 3-pool exchange model with the individual amine, amide and water

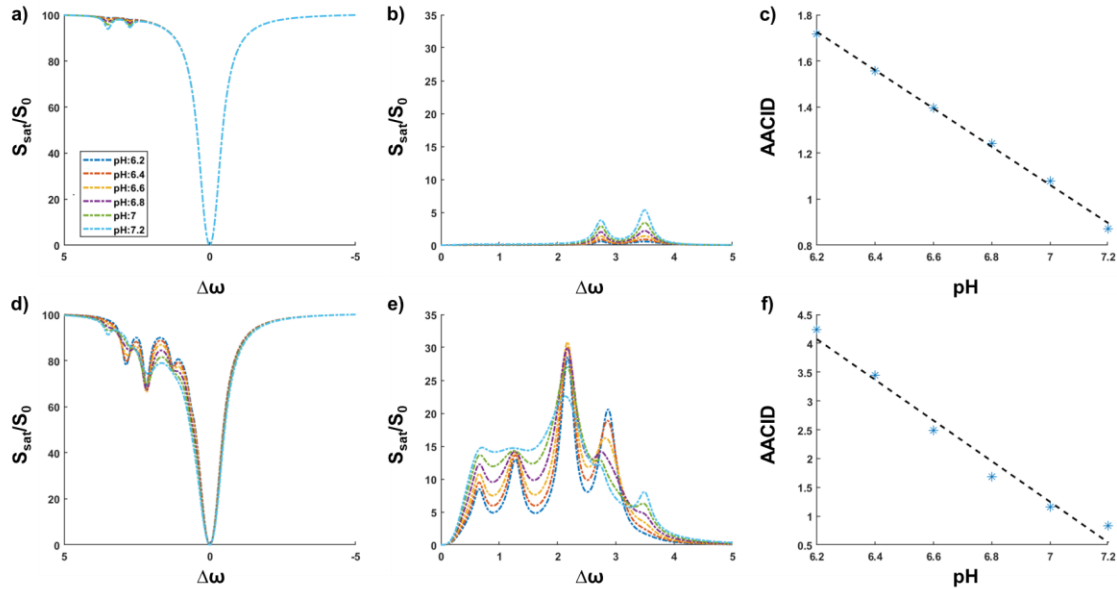


Figure 1.5: Illustrative simulation results of a 3-pool model on the top row (a-c) and a 7-pool model in the bottom row (d-f). The resultant Z-spectra (a) along with their corresponding MTR_{asym} spectra (b) and the AACID values at their associated pHs (c) in a biological system without the presence of glucose. When glucose is added to the system, the simulation results for the Z-spectra (d), corresponding MTR_{asym} spectra (e) and the AACID values at their associated pHs (f) are shown above. The dotted lines in panel c) and f) denote the line of best fit.

pools (as shown in **Figure 1.5a**) can be set up to simulate the CEST signals at various pHs. After calculating AACID using **Equation 1.18**, pH is plotted against its corresponding AACID values as shown in **Figure 1.5c**, a linear relationship can be found within tumor biological pH range [9,56]. A 7-pool exchange model is used to simulate a biological system containing glucose, as mentioned above 4 pools are associated with the 4 proton exchange sites on glucose, and the remaining 3 pools are amine, amide and water pools respectively. The Z-spectra and their corresponding MTR_{asym} spectra at their associated pHs are plotted in **Figure 1.5d** and **Figure 1.5e**, and the AACID with the presence of glucose is plotted against pH as shown in **Figure 1.5f**. The linear relationship between AACID and pH still stands even with glucose present when comparing **Figure 1.5c** and **Figure 1.5f**.

$$\text{AACID} = \frac{\text{Mz}(3.50 \text{ ppm}) \times (\text{Mz}(6 \text{ ppm}) - \text{Mz}(2.75 \text{ ppm}))}{\text{Mz}(2.75 \text{ ppm}) \times (\text{Mz}(6 \text{ ppm}) - \text{Mz}(3.50 \text{ ppm}))} \text{ [Equation 1.18]}$$

1.4.1.4 AcidoCEST

Similar to AACID, acidoCEST also takes advantages of the different proton exchange behavior under different pH environments for certain metabolites. Distinct from AACID, an exogenous contrast agent, iopamidol, is introduced [57]. Iopamidol, cannot go into the intracellular space, therefore, it is used to evaluate pH_e . The proton exchange of the protons on two amide groups (as shown in **Figure 1.6**) can be detected using CEST, and can be modeled using the following equations [57]:

$$k_{\text{amide}} = 1.2 \times 10^{\text{pH}-4.1} \text{ [Equation 1.19]}$$

$$k_{\text{amide}} = 1.2 \times 10^{\text{pH}-4.6} \text{ [Equation 1.20]}$$

Their CEST signals can be seen on the Z-spectra at 4.3 and 5.6 ppm as shown in **Figure 1.7a**. A similar 3-pool exchange model with pools associated with the 2 proton exchange sites on the amide functional groups on iopamidol and neighboring water molecules can be defined using the same Bloch-McConnell analytical solution described above. Meanwhile, a 7-pool exchange model can be used to simulate CEST signals with the presence of

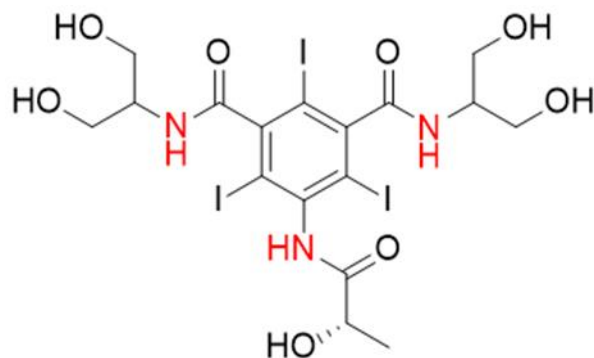


Figure 1.6: The chemical structure of Iopamidol, the two amide functional groups provide proton exchange sites (in red) with neighboring water.

glucose molecules similar to what has been described in **Section 1.4.1.3**. The Z and MTR_{asym} spectra are plotted under different pH conditions as shown in **Figure 1.7**. The

acidoCEST method utilizes a ratiometric measurement (R_{ST}) between the CEST singles of the two amides either using **Equation 1.21** derived in the original publication [57]:

$$R_{ST} = \log_{10} \frac{[(M_0 - M_S)/M_0](4.2 \text{ ppm})}{[(M_0 - M_S)/M_0](5.5 \text{ ppm})} \quad \text{[Equation 1.21]}$$

which indicates a linear relationship between pH and R_{ST} ; or using the simplified version of the equation with **Equation 1.22** as described by Longo et al [58] with good accuracy but an non-linear relationship between pH and R_{ST} .

$$R_{ST} = \frac{MTR_{\text{asym}}(4.2 \text{ ppm})}{MTR_{\text{asym}}(5.5 \text{ ppm})} \quad \text{[Equation 1.22]}$$

Both methods indicate a directly proportional relationship between acidoCEST and the corresponding pH within the tumor biological pH_e range [57,58]. The simplified method indicated by **Equation 1.22** is used to obtain a relationship between pH and acidoCEST measurements without and with the presence of glucose as shown in **Figure 1.7c** and **1.7f**. The relationship is not affected by the presence of glucose by comparing these two panels from **Figure 1.7**.

1.4.1.5 Simultaneously measuring pH_i and pH_e

The same analytical solution to Bloch-McConnell equation adapted from Zaiss et al [36,40,50,59] is used to simulate the possibility of measuring pH_i and pH_e simultaneously

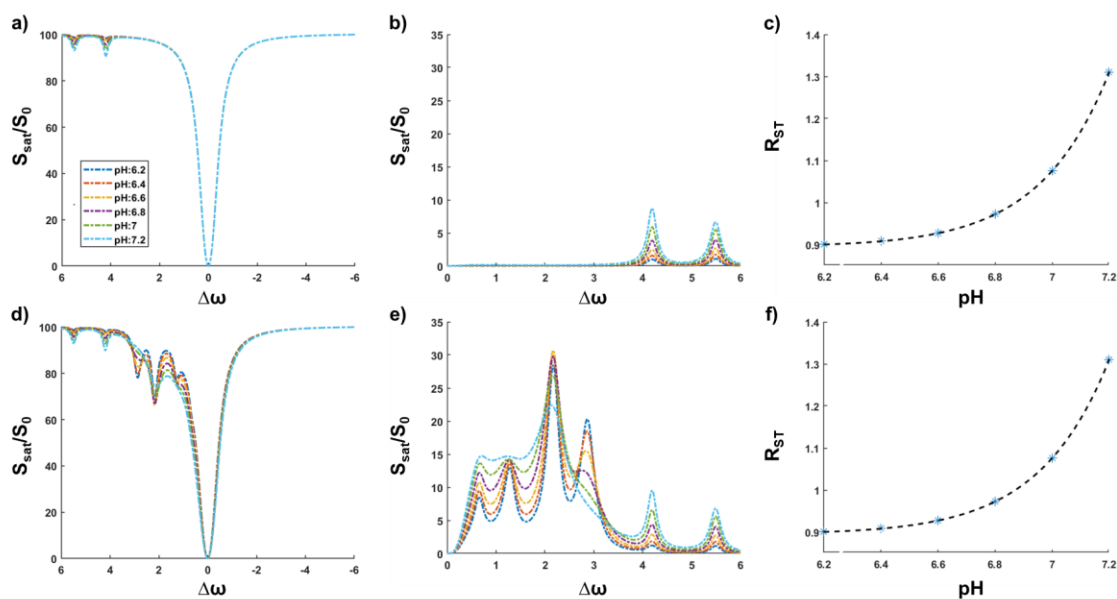


Figure 1.7: Illustrative simulation results of a 3-pool model on the top row (a-c) and a 7-pool model in the bottom row (d-f). The resultant Z-spectra (a) along with their corresponding MTR_{asym} spectra (b) and the R_{ST} at their associated pHs (c) in a biological system without the presence of glucose. When glucose is added to the system, the simulation results for the Z-spectra (d), corresponding MTR_{asym} spectra (e) and the R_{ST} at their associated pHs (f) are shown above. The dotted lines in panel c) and f) denote the line of best fit.

with the presence of glucose at different concentrations and with various pH environments in a biological system with the presence of endogenous amine, amide, and exogenous iopamidol using AACID and acidoCEST respectively.

A 9-pool model is used, pool A is the water pool, pool B, C, D, E are associated with the 4 proton exchanging sites on the glucose molecule, pool F is associated with endogenous amine, pool G is the endogenous amide pool, pool H and I are the proton exchange sites arising from the two amide functional groups on the iopamidol molecule as mentioned above.

As shown by the results of the simulation (in **Figure 1.8**), the presence of glucose solution does not possess a simple main effect on pH_i and pH_e measured using AACID (**Figure 1.8c**) and acidoCEST (**Figure 1.8d**) respectively, meanwhile, AACID and acidoCEST do not interfere with each other when measuring pH_i and pH_e when comparing to the results shown in **Figure 1.5f** and **Figure 1.7f**.

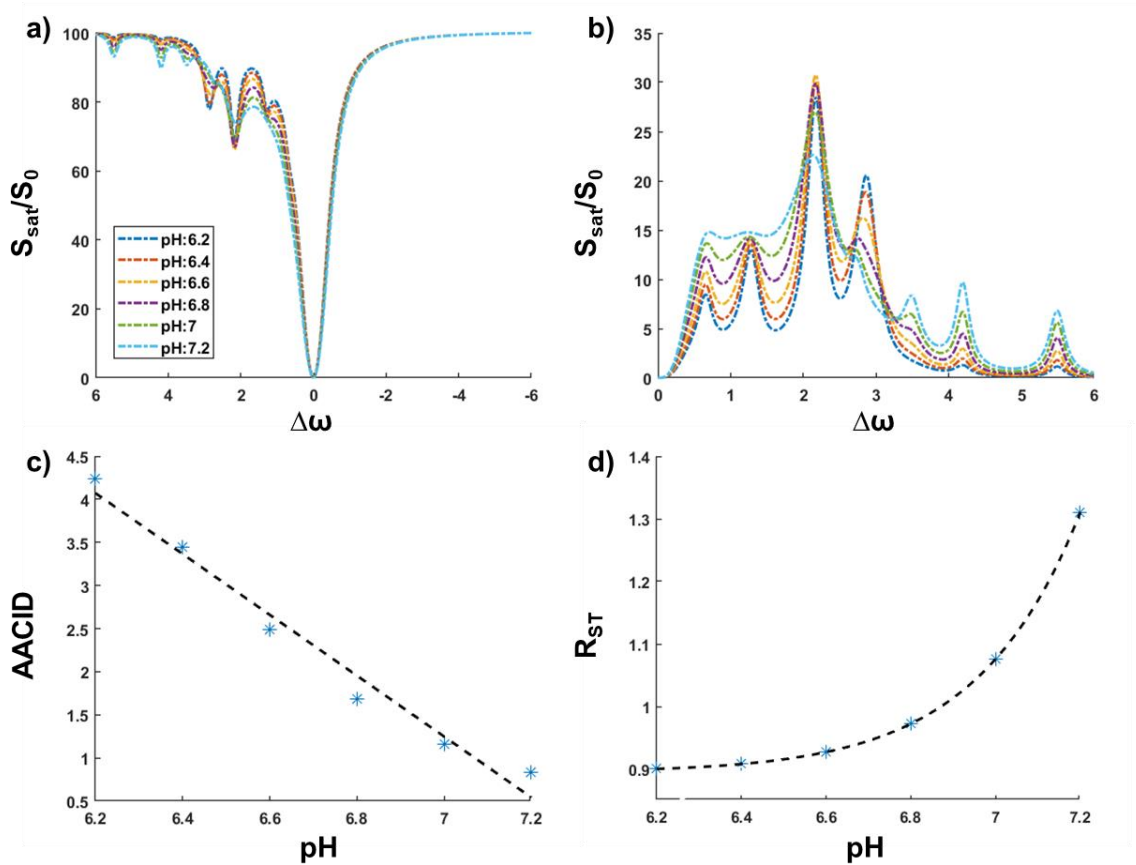


Figure 1.8: An illustrative simulation result of a 9-pool exchange model: the Z-spectra and their corresponding MTR_{asym} spectra at different pHs are shown in a) and b) respectively. pH vs. AACID and R_{ST} are plotted in c) and d) respectively.

1.4.2 Hyperpolarized $[1-^{13}\text{C}]$ pyruvate MRSI

Cellular anaerobic glycolysis can also be measured using magnetic resonance spectroscopy (MRS) using hyperpolarized $[1-^{13}\text{C}]$ pyruvate. In cancer, especially under hypoxic and lower pH_e environment, the majority of the glucose will go through anaerobic glycolysis. As a result, pyruvate is produced via glycolysis as shown in **Equation 1.3**, however most of the produced pyruvate is converted to lactate acids by lactate dehydrogenase as shown

in **Figure 1.1**, instead of being utilized for the Krebs cycle for more efficient energy production [3–6]. Hyperpolarized [1-¹³C]pyruvate MRSI takes advantage of this metabolic behavior. After injection, [1-¹³C]pyruvate is transported inside the cells using the monocarboxylate transporter (MCT) and then converted into [1-¹³C]lactate [60].

The first carbon on pyruvate can be labelled with ¹³C and hyperpolarized using a process to enhance the magnetization of the first carbon by increasing the degree of alignment with the magnetic field of the carbon nucleus [34,61]. The hyperpolarization of the carbon nucleus can be achieved using a method called dynamic nuclear polarization [32,33], through which the spin polarization from the electron is transferred to the nucleus mediated by microwave irradiation. In order to utilize the hyperpolarized [1-¹³C]pyruvate for *in vivo* use, a dissolution process needs to be performed, during which the hyperpolarized [1-¹³C]pyruvate is mixed with superheated buffer solution at high pressure. As a result of hyperpolarization using dynamic nuclear polarization, a 10,000-fold increase in the MRI signal from hyperpolarized [1-¹³C]pyruvate is achieved compared to thermal equilibrium [33,34].

MRSI is used to detect the signals from [1-¹³C]pyruvate as well as [1-¹³C]lactate to measure the cancer aerobic glycolytic metabolism. The ratio of lactate and pyruvate (Lac:Pyr) can be obtained by dividing the amplitude of the lactate peak over the amplitude of the pyruvate peak on the spectrum, and the regional map of Lac:Pyr as an evaluation of anaerobic glycolysis can be constructed.

1.5 Computed tomography perfusion

The perfusion properties of different tissues can be studied using perfusion imaging techniques by monitoring the passage of a contrast agent as it travels through these tissues [62]. A change of image intensity can be captured with perfusion imaging as the contrast agent passes through the vasculature. Computed tomography perfusion (CTP) is a well-established perfusion-imaging technique, using an iodinated contrasted agent to characterize the tissue perfusion properties. CT imaging is based on the x-ray attenuation through different tissues with signal intensity depending on the electron densities of

different tissue types (i.e., soft tissue or bone). The injected iodinated contrast agent produces distinct signal intensity as it traverses through the tissue.

To quantitatively evaluate the different tissue perfusion properties, the tracer kinetics of the contrast agent can be defined using a Johnson-and-Wilson model [63,64]. A tissue time-concentration curve $C_t(t)$ can be defined using the tissue image signal intensity as a function of time to represent the change in tissue contrast concentration over time. Similarly, an arterial input function $C_a(t)$ is defined as the change in image intensity at an input artery to the tissue (i.e., carotid artery as an input artery to study brain perfusion) as a function of time. Tissue perfusion characteristics such as blood flow (BF), blood volume (BV) and permeability-surface area product (PS) can be estimated from tracer kinetic analysis:

$$\begin{aligned} C_t(t) &= C_a(t) \otimes \text{BF} \cdot R(t) \\ &= \int_0^t C_a(\tau) \cdot [\text{BF} \cdot R(t - \tau)] d\tau \quad \text{[Equation 1.23]} \end{aligned}$$

where $R(t)$ is the impulse residue function (IRF) defined as the fraction of contrast that is contained in the tissue as a function of time after the contrast is injected instantaneously.

$R(t)$ is scaled by BF and defined as:

$$R(t) = \begin{cases} 1 & 0 \leq t \leq \frac{\text{BV}}{\text{BF}} \\ E e^{-\frac{\text{BF} \cdot E}{v_e} \left(t - \frac{\text{BV}}{\text{BF}}\right)} & t > \frac{\text{BV}}{\text{BF}} \end{cases} \quad \text{[Equation 1.24]}$$

v_e is the distribution volume of extravascular extracellular space per unit volume of tissue, and E is the extraction fraction that is described as the fraction of contrast that leaks into the interstitial space and is defined as:

$$E = 1 - e^{-\frac{\text{PS}}{\text{BF}}} \quad \text{[Equation 1.25]}$$

CTP measurements consist of two phases of imaging acquisition after a bolus injection of the iodinated contrast agent based on the BF-scaled IRF. The first phase involves rapid image acquisitions (1 – 2 s per image) capturing the first wash-in and wash-out process of the contrast agent to calculate BF and BV. BF can be solved by deconvolving the $C_a(t)$ with $C_t(t)$ using **Equation 1.23**, and BV is estimated as the area under the IRF during the first phase. The second phase consists of less frequent acquisitions (10 – 15 s per image) to

calculate PS. E is the height of IRF at the beginning of the second phase, and PS can then be solved from **Equation 1.25** with known E and BF.

1.6 Positron emission tomography

PET imaging is based on the interaction between an electron and a positron arising from the decay of a positron-emitting radionuclide. A small dose of radionuclide is injected into patients prior to a PET scan. The radionuclide will continue to decay as it moves through the blood stream until it reaches the designated target, releasing positrons that collide with nearby electrons in a process known as positron-electron annihilation. These interactions will emit a pair of 511 keV gamma photons that exit the body and are detected by the PET scanner [65–67].

1.6.1 PET basics:

Commonly used positron-emitting radioisotopes (such as ^{11}C , ^{13}N , ^{15}O and ^{18}F) are produced locally in a cyclotron due to their short half-life. These radioisotopes are then used to synthesize various radio-labeled compound or radiotracers based on the clinical need. The two photons will be detected by two detectors on the ring of PET scintillation detectors, the signals from the detectors are then amplified, digitized, and the digitized values histogrammed using a multi-channel analyzer. A coincidence window of Δt will be

set, where Δt defines the temporal or timing resolution (3-4 ns) for the two events to be registered as coincidence event. The acquired signal is stored in a list-mode data set

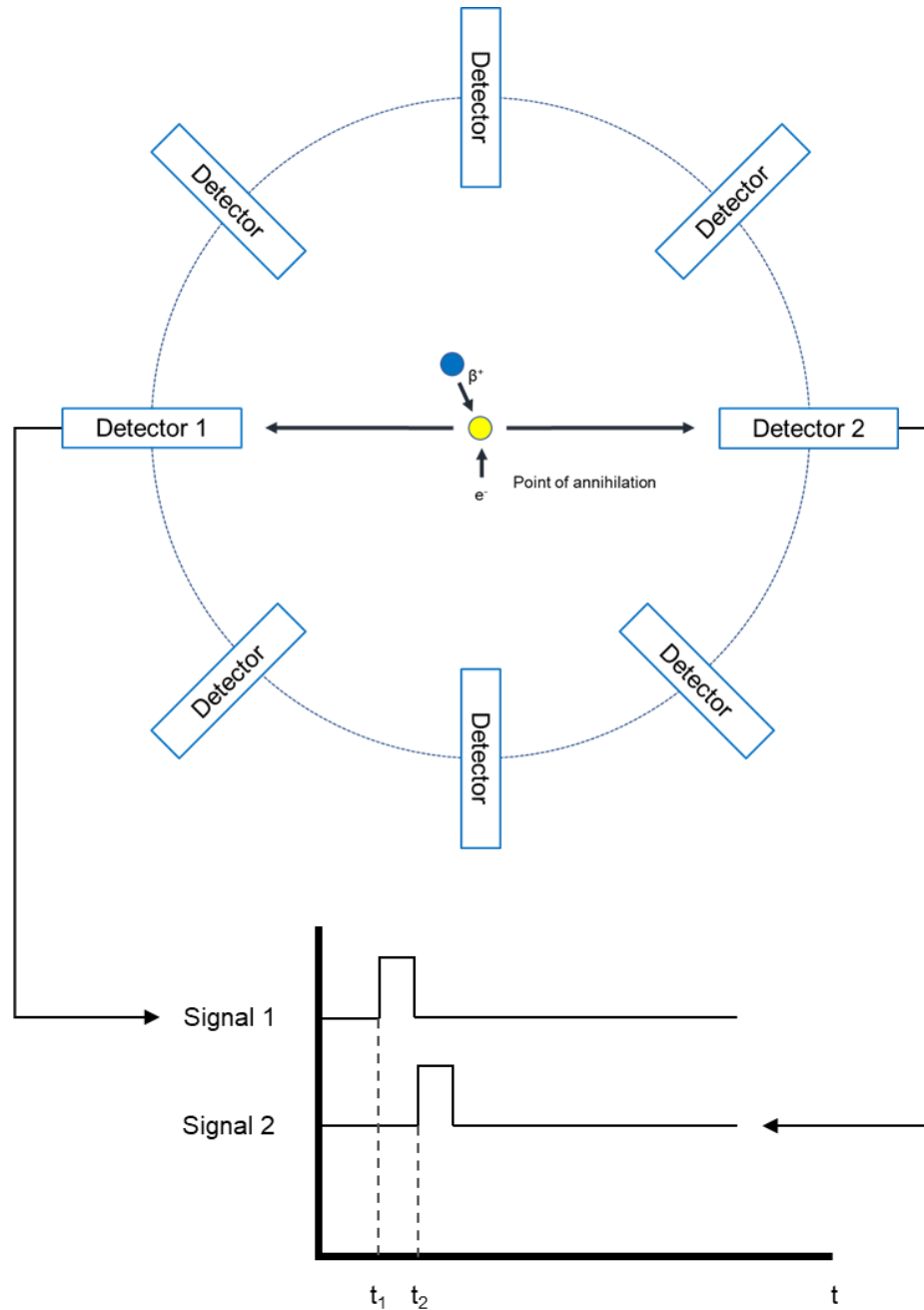


Figure 1.9: Schematic of detecting coincidence events for two detectors. Signal 1 from Detector 1 results in a trigger pulse 1 which sets the start of check the coincidence window. Signal 2 from Detector 2 results in a trigger pulse 2. A coincidence circuit will check for coincidence between the pulse 2 and pulse 1 ($\Delta t = t_2 - t_1$) and the coincidence window (timing resolution).

(containing detector locations and detection time for each coincidence event), processed into sinograms, and reconstructed into volumes portraying the distribution of PET tracer averaged over a period of time in a single frame or multiple frames. For a 3D acquisition, each frame of data can be binned into a set of N^2 oblique sinograms between detector rings, where N is the number of detector rings and a sinogram is a graph that plots the number of coincidences detected for each possible detector pair. Sinograms are corrected for random and scatter emission events before PET images are reconstructed using a filtered back projection reconstruction [68] or iteratively by comparing them to the sinograms of different theoretical volumes. For instance, the 3D ordered-subset expectation maximization followed by fast maximum *a posteriori* (OSEM3D/FMAP), works by dividing the measured sinograms into non-overlapping subsets and using only one subset at a time to minimize the difference between the measured subset and a theoretical subset that is based on the forward projection of a model image (OSEM3D), and then by maximizing a function that penalizes images that do not fit the data well (MAP) [69]. The standardized uptake value (SUV) is most commonly used to semi-quantify clinical PET signals with a single late-time-point activity normalized by the injected activity and the weight of the subject [66], calculated as:

$$\text{SUV} = \frac{\text{Activity}_{\text{region of interest}}}{\text{Activity}_{\text{injected}} \div \text{Weight}} \quad \text{[Equation 1.26]}$$

Depending on the kinetics of the ^{18}F -labeled tracer, static PET images may be acquired 30 to 120minutes after injection to disregard the perfusion effect of the tracers. PET images can also be analyzed using tracer kinetic modelling: kinetic modelling accounts for the effect of tracer pharmacokinetics (tracer delivery, clearance and target reaction), as a result, it can provide more accurate information about the target concentration (measured by volume of distribution) and influx/efflux rate constants [70,71].

1.6.2 [^{18}F]-Fluorodeoxyglucose (FDG)

FDG is the most commonly used PET radionuclide for cancer imaging. The structure of FDG is shown in **Figure 1.10a**. FDG is similar in structure to glucose, replacing the

hydroxyl group at the 2nd carbon location with an ¹⁸F, and it can be transported into cells using the same glucose transporters (GLUTs). After a bolus injection of FDG (in pmol), FDG will be transported into the cells and go through the first step of glycolysis in the cytoplasm, phosphorylated by hexokinase to FDG-6-phosphate (FDG6P), without continuing the rest of the glycolytic steps (as shown in **Figure 1.10a**). As a result, FDG6P will be trapped inside of the cells and provide signals which can then be detected with PET. The Patlak graphical analysis method assumes that the pharmacokinetics of FDG is irreversible [72], i.e. FDG6P will be trapped inside the cells after FDG is phosphorylated. However, a recent study has shown the reversibility of FDG6P trapping, where FDG6P could be fed into the pentose phosphate pathway by glucose-6-phosphate dehydrogenase, and in turn be transported out of the cell by GLUTs [73]. A Logan graphical analysis method could be employed to better model FDG pharmacokinetics, as it assumes reversible binding for radiopharmaceuticals [74]. Cancer cells are known to over-rely on glycolysis and have a higher glycolytic activity compared to normal mammalian cells [3,5,66,75], therefore, FDG can provide information on cancer glycolytic metabolism at a cellular level.

1.6.3 PET kinetic modeling

Tracer kinetic modelling has the practical purpose of condensing dynamic information into parameters describing the primary processes that affect tracer distribution. PET experiments can capture the dynamic changes in tracer concentration which do not get distributed instantaneously according to the quantity of the target reaction. Instead, the tracer dynamically experiences two or more processes including delivery, clearance, and the target reaction. As a result, the tracer undergoes dynamic change, and this can be seen by plotting the tracer radioactivity concentration against time to construct what is frequently referred to as a time-activity-curve (TAC).

To model the pharmacokinetic process of FDG, an irreversible two-tissue three compartment (2T3C) system [70,76] is commonly used as shown in **Figure 1.10b**.

FDG is transferred from plasma (first compartment) to the extravascular space including the extracellular space of the tissue of interest (second compartment) with the rate constant K_1 (mL/min/mL of tissue), and the reverse rate constant k_2 (min^{-1}). FDG is then transported from the second compartment to the intracellular space in the tissue of interest where it is phosphorylated by hexokinase to FDG-6-phosphate (FDG6P) with the rate constant k_3 (min^{-1}), FDG6P is trapped in the intracellular space without going through the subsequent steps of glycolysis.

FDG studies can be analyzed using the compartmental model with three rate constants and the combination of the rate constants or the net transfer rate (K_i) can be found [77]:

$$K_i = \frac{K_1 \times k_3}{k_2 + k_3} \quad \text{[Equation 1.27]}$$

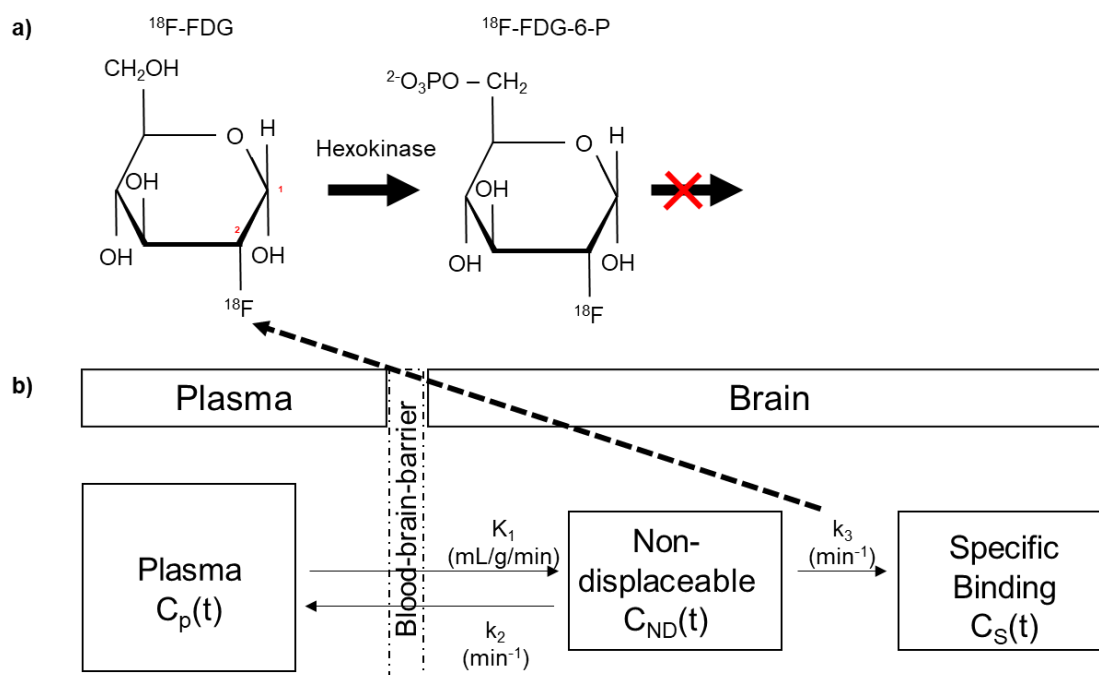


Figure 1.10: a) The chemical structure of ^{18}F -FDG and its metabolism after entering the cell, it will go through the first step of glycolysis and be phosphorylated to ^{18}F -FDG-6-P and is subsequently trapped inside the cell. b) A schematic of the 2T3C model for ^{18}F -FDG, $C_p(t)$ represent the radioactivity in the plasma as a function of time, $C_{ND}(t)$ represents the activity of free ^{18}F -FDG after entering the brain but before being trapped in the cells as a function of time. $C_S(t)$ represents the activity as a function of time after ^{18}F -FDG enters and is trapped inside the cell.

To simplify the 2T3C model estimation, Patlak graphical analysis was developed as a model independent graphical analysis method to estimate the net transfer rate for tracers with irreversible bindings i.e. without a reversible component [72,78]. An assumption needs to be met in order to use Patlak analysis: all reversible compartments must be in equilibrium with plasma, i.e. the concentration of radiopharmaceutical used in plasma and in the reversible tissue compartments must remain stable. The apparent distribution volume that is the ratio of tissue time-activity curve (TAC(t)) and arterial input function (AIF(t)), is plotted against the normalized plasma integral which is the ratio of the integral of AIF(t) and the AIF(t) as shown in **Equation 1.28**.

$$\frac{C_{ROI}(T)}{AIF(T)} = K_i \times \frac{\int_0^T AIF(t)dt}{AIF(T)} + Int \quad [\text{Equation 1.28}]$$

Where T denotes the time interval from the start to a specific frame, and Int denotes the y-intercept. When the equilibrium is reached, i.e., after the distribution volume of reversible compartments is effectively constant, the Patlak plot becomes linear, and the slope of the linear phase is K_i which can be in turn converted to the metabolic rate of glucose (MRGlu) using **Equation 1.29**:

$$MRGlu = K_i \times \frac{C_{Glucose\ Plasma}}{LC} \quad [\text{Equation 1.29}]$$

Where $C_{glucose\ plasma}$ is the concentration of glucose in the plasma, and LC is the lumped constant, a conversion factor to obtain estimation of the glucose metabolic rate from the glucose analog FDG [78,79]. Kinetic modeling with Patlak graphical analysis or compartmental modeling allows quantitative assessment of glucose utilization from FDG [79,80].

1.8 Objectives and Hypothesis

Chapter 2: To evaluate glucoCEST as a surrogate biomarker of tumor perfusion and/or tumor glycolysis, we compared various well-defined *in vivo* perfusion and glycolysis measurements in the C6 rat glioma model. Tumor perfusion maps such as blood flow (BF), blood volume (BV), and permeability surface-area product (PS) were derived with computed tomography perfusion (CTP) measurements acquired during a bolus injection of

iodinated contrast agent (Iovue). Glucose metabolism was evaluated with positron emission tomography (PET) and ^{18}F -fluorodeoxyglucose (FDG), a glucose analogue which is phosphorylated in the cell but does not go through subsequent steps of glycolysis. Anaerobic glycolysis was measured with MR spectroscopic imaging (MRSI) after an injection of hyperpolarized $[1-^{13}\text{C}]$ pyruvate.

We hypothesized that glucoCEST measurements of the change in glucoCEST signal during glucose infusion comparing to baseline (ΔCEST) is directly proportional to perfusion measurements. Tumor perfusion measurements of PS were also found to be directly proportional to tumor glycolytic measurement of Lac:Pyr. These results were published in *Molecular Imaging and Biology*:

Q. Qi et al., Multimodality In Vivo Imaging of Perfusion and Glycolysis in a Rat Model of C6 Glioma, *Mol Imaging Biol.* 2021, **23**: 516-526, DOI: 10.1007/s11307-021-01585-1.

Chapter 3: This experiment aimed to explore the relationship between tumoral and peritumoral pH_i and the change in pH_i after a glucose infusion using AACID CEST MRI, and tumoral glycolytic activity measured using FDG-PET and hyperpolarized $[1-^{13}\text{C}]$ pyruvate MRSI.

We hypothesized that tumoral and peritumoral pH_i are inversely proportional to tumor glycolysis measurements; and the change in tumoral and peritumoral pH_i induced by glucose infusion are directly proportional to tumor glycolysis measurements. These results were submitted to *Molecular Imaging in Biology*:

Q. Qi et al., Glucose Infusion Induced Change in Intracellular pH and Its Relationship with Tumor Glycolysis in a C6 Rat Model of Glioblastoma. *Mol Imaging and Bio*, submitted in November 2021.

Chapter 4: In this chapter we explored the feasibility of measuring tumor intracellular pH and extracellular pH simultaneously with AACID and acidoCEST respectively after a pH change was induced by a glucose injection. We also evaluated the correlations between tumor pH environments and tumor glycolysis measurements.

We expected that the change in pH_i and pH_e can be detected *in vivo* with CEST MRI, and we hypothesized that tumor pH_i is directly proportional to tumor glycolytic activity; and

tumor pH_e is inversely proportional to tumor glycolytic activity. These results will be submitted in early 2022 to an appropriate journal:

Q. Qi et al., Evaluation of the Change in Tumor Intra-/Extracellular pH Environment Induced by Glucose Injection and its Relationship with Tumor Glycolysis in a C6 Rat Model of Glioblastoma. To be submitted.

Chapter 5: In this concluding chapter, we discuss the key findings, limitations, and future directions to better investigate cancer perfusion, glycolysis, and its pH environment.

1.9 Reference

1. Ahir BK, Engelhard HH, Lakka SS. (2020) Tumor Development and Angiogenesis in Adult Brain Tumor: Glioblastoma. *Mol Neurobiol* 57(5):2461.
2. Jain RK, Di Tomaso E, Duda DG, et al. (2007) Angiogenesis in Brain Tumours. *Nat Rev Neurosci* 8(8):610-622.
3. Heiden MG, Cantley LC, Thompson CB. (2009) Understanding the Warburg Effect: The Metabolic Requirements of Cell Proliferation. *Science* 324(5930):1029-1033.
4. Corbet C, Feron O. (2017) Tumour acidosis: From the Passenger to the Driver's Seat. *Nat Rev Cancer*. 17(10):577-593.
5. Xu XD, Shao SX, Jiang HP, et al. (2011) Warburg Effect or Reverse Warburg Effect? A Review of Cancer Metabolism. *Oncol Res Treat* 38(3):117-122.
6. Webb BA, Chimenti M, Jacobson MP, et al. (2011) Dysregulated pH: A Perfect Storm for Cancer Progression. *Nat Rev Cancer* 11(9):671-677.
7. Thews O, Riemann A. (2019) Tumor pH and Metastasis: a Malignant Process beyond Hypoxia. *Cancer Metastasis Rev* 38 (1-2): 113-120.
8. Estrella V, Chen T, Lloyd M, et al. (2013) Acidity Generated by the Tumor Microenvironment Drives Local Invasion. *Cancer Res* 73(5):1524-1535.
9. Lim H, Albatany M, Martínez-Santesteban F, Bartha R, et al. (2018) Longitudinal Measurements of Intra-and Extracellular pH Gradient in a Rat Model of Glioma. *Tomography* 4(2): 46-54.
10. Glioblastoma (GB) – Brain Tumour Foundation of Canada. (2021) https://www.braintumour.ca/brain_tumour_types/glioblastoma-gb/.
11. Zong H, Verhaak RGW, Canolk P. (2012) The Cellular Origin for Malignant Glioma and Prospects for Clinical Advancements. *Expert Rev Mol Diagn* 12(4):383.
12. Louis DN, Ohgaki H, Wiestler OD, et al. (2007) The 2007 WHO Classification of Tumours of the Central Nervous System. *Acta Neuropathol* 114(2):97.
13. Tian Z, Chen C, Fan Y, et al. (2019) Glioblastoma and Anaplastic Astrocytoma: Differentiation Using MRI Texture Analysis. *Front Oncol* 9:876.
14. Hanif F, Muzaffar K, Perveen K, et al. (2017) Glioblastoma Multiforme: A Review

of its Epidemiology and Pathogenesis through Clinical Presentation and Treatment. *Asian Pac J Cancer Prev* 18(1):3.

15. Wen PY, Weller M, Lee EQ, et al. (2020) Glioblastoma in Adults: a Society for Neuro-Oncology (SNO) and European Society of Neuro-Oncology (EANO) Consensus Review on Current Management and Future Directions. *Neuro Oncol* 22(8):1073-1113.
16. Furnari FB, Fenton T, Bachoo RM, et al. (2007) Malignant Astrocytic Glioma: Genetics, Biology, and Paths to Treatment. *Genes Dev* 21(21):2683-2710.
17. Giakoumettis D, Kritis A, Foroglou N. (2018) C6 Cell Line: the Gold Standard in Glioma Research. *Hippokratia* 22(3):105.
18. Doblaz S, He T, Saunders D, et al. (2012) *In vivo* Characterization of Several Rodent Glioma Models by ¹H MRS. *NMR Biomed* 25(4):685-694.
19. Nagano N, Sasaki H, Aoyagi M, et al. (1993) Invasion of Experimental Rat Brain Tumor: Early Morphological Changes Following Microinjection of C6 Glioma Cells. *Acta Neuropathol* 86(2):117-125.
20. Parsa AT, Chakrabarti I, Hurley PT, et al. (2000) Limitations of the C6/Wistar Rat Intracerebral Glioma Model: Implications for Evaluating Immunotherapy. *Neurosurgery* 47(4):993-1000.
21. Martínez-Reyes I, Chandel NS. (2020) Mitochondrial TCA Cycle Metabolites Control Physiology and Disease. *Nat Commun* 11(1):1-11.
22. Webb BA, Chimenti M, Jacobson MP, et al. (2011) Dysregulated pH: a Perfect Storm for Cancer Progression. *Nat Rev Cancer* 11(9):671-677.
23. Felmler MA, Jones RS, Rodriguez-Cruz V, et al. (2020) Monocarboxylate Transporters (SLC16): Function, Regulation, and Role in Health and Disease. *Pharmacol Rev* 72(2):466-485.
24. Albatany M. (2018) Monitored Acute Pharmacologic Modulation of Glioblastoma pH Monitored by Chemical Exchange Saturation Transfer Magnetic Resonance Imaging. PhD Thesis.
25. Swietach P, Vaughan-Jones RD, Harris AL, et al. (2014) The Chemistry, Physiology and Pathology of pH in Cancer. *Philos Trans R Soc B Biol Sci.* 369(1638).
26. Hao G, Xu ZP, Li L. (2018) Manipulating Extracellular Tumour pH: an Effective Target for Cancer Therapy. *RSC Adv* 8(39):22182-22192.

27. Brewer PG. (2013) A Short History of Ocean Acidification Science in the 20th century: A Chemist's View. *Biogeosciences* 10(11):7411-7422.
28. Nath K, Nelson DS, Heitjan DF, et al. (2015) Effects of Hyperglycemia on Ionidamine-Induced Acidification and De-energization of Human Melanoma Xenografts and Sensitization to Melphalan. *NMR Biomed* 28(3):395-403.
29. Buxton RB, Alpert NM, Babikian V, et al. (1987) Evaluation of the $^{11}\text{CO}_2$ Positron Emission Tomographic Method for Measuring Brain pH. I. pH Changes Measured in States of Altered PCO_2 . *J Cereb Blood Flow Metab* 7(6):709-719.
30. Van Zijl PCM, Yadav NN. (2011) Chemical Exchange Saturation Transfer (CEST): What is in a Name and What isn't? *Magn Reson Med* 65(4):927.
31. Liu G, Song X, Chan K W Y, McMahon MT. (2013) Nuts and Bolts of Chemical Exchange Saturation Transfer MRI. *NMR Biomed* 26(7):810-828.
32. Babourina-Brooks B, Wilson M, Arvanitis TN, et al. (2014) MRS Water Resonance Frequency in Childhood Brain Tumours: a Novel Potential Biomarker of Temperature and Tumour Environment. *NMR Biomed* 27(10):1222.
33. Alger JR. (2000) Magnetic Resonance Spectroscopy. *Encycl Neurosci* 601-607.
34. Lim H. (2017) A Longitudinal Study of Tumour Metabolism Using Hyperpolarized Carbon-13 Magnetic Resonance Spectroscopic Imaging in a Preclinical Model of Glioma. PhD Thesis.
35. Ward KM, Aletras AH, Balaban RS. (2000) A New Class of Contrast Agents for MRI Based on Proton Chemical Exchange Dependent Saturation Transfer (CEST). *J Magn Reson* 143(1):79-87.
36. Zaiss M, Bachert P. (2013) Chemical Exchange Saturation Transfer (CEST) and MR Z-Spectroscopy *in vivo*: a Review of Theoretical Approaches and Methods. *Phys Med Biol* 58(22):R221.
37. Chan K W Y, Bulte J W M, McMahon MT. (2014) Diamagnetic Chemical Exchange Saturation Transfer (diaCEST) Liposomes: Physicochemical Properties and Imaging Applications. *Nanomed Nanobiotechnol* 6(1):111.
38. Jones CK, Huang A, Xu J, et al. (2013) Nuclear Overhauser Enhancement (NOE) Imaging in the Human Brain at 7 T. *Neuroimage* 77:114-124.
39. Zhou J, Lal B, Wilson DA, et al. (2003) Amide Proton Transfer (APT) Contrast for Imaging of Brain Tumors. *Magn Reson Med*. 50(6):1120-1126.
40. Zaiss M, Zu Z, Xu J, et al. (2015) A Combined Analytical Solution for Chemical

- Exchange Saturation Transfer and Semi-solid Magnetization Transfer. *NMR Biomed* 28(2):217-230.
41. Zaiss M, Anemone A, Goerke S, et al. (2019) Quantification of Hydroxyl Exchange of D-Glucose at Physiological Conditions for Optimization of glucoCEST MRI at 3, 7 and 9.4 Tesla. *NMR Biomed*. 32(9): e4113.
 42. Xu X, Yadav NN, Knutsson L, et al. (2015) Dynamic Glucose-Enhanced (DGE) MRI: Translation to Human Scanning and First Results in Glioma Patients. *Tomography* 1(2):105.
 43. Walker-Samual S, Ramasawmy R, Torrealdea F, et al. (2013) *In vivo* Imaging of Glucose Uptake and Metabolism in Tumors. *Nat Med* 19(8):1067-1072.
 44. Rivlin M, Navon G. (2019) Molecular Imaging of Tumors by Chemical Exchange Saturation Transfer MRI of Glucose Analogs. *Quant Imaging Med Surg* 9(10):1731-1746.
 45. Xu X, Chan KWY, Knutsson L, et al. (2015) Dynamic Glucose Enhanced (DGE) MRI for Combined Imaging of Blood-Brain Barrier Break Down and Increased Blood Volume in Brain Cancer. *Magn Reson Med* 1563:1556-1563.
 46. Xu X, Xu J, Knutsson L, et al. (2019) The Effect of the mTOR Inhibitor Rapamycin on glucoCEST Signal in a Preclinical Model of Glioblastoma. *Magn Reson Med* 81(6):3798.
 47. Xu X, Xu J, Laterra J, et al. (2019) Magnetic Resonance in Medicine CEST MRI of 3 - O - methyl - D - glucose Uptake and Accumulation in Brain Tumors. *Magn Reson Med* 81(3):1993-2000.
 48. Chan KWY, McMahon MT, Kato Y, et al. (2012) Natural D-Glucose as a Biodegradable MRI Contrast Agent for Detecting Cancer. *Magn Reson Med* 68(6):1764. d
 49. Wang J, Weygand J, Hwang KP, et al. (2016) Magnetic Resonance Imaging of Glucose Uptake and Metabolism in Patients with Head and Neck Cancer. *Sci Reports* 6(1):1-7.
 50. Zaiss M, Bachert P. (2013) Exchange-dependent Relaxation in the Rotating Frame for Slow and Intermediate Exchange – Modeling Off-resonant Spin-lock and Chemical Exchange Saturation Transfer. *NMR Biomed* 26(5):507-518.
 51. McVicar N, Li AX, Gonçalves DF, et al. (2014) Quantitative Tissue pH Measurement during Cerebral Ischemia using Amine and Amide Concentration-independent Detection (AACID) with MRI. *J Cereb Blood Flow Metab* 34(4):690-698.

52. Van Zijl PCM, Yadav NN. (2011) Chemical Exchange Saturation Transfer (CEST): What is in a Name and What isn't? *Magn Reson Med* 65(4):927-948.
53. Wu R, Xiao G, Zhou IY, et al. (2015) Quantitative Chemical Exchange Saturation Transfer (qCEST) MRI-Omega Plot Analysis of RF Spillover-corrected Inverse CEST Ratio Asymmetry for Simultaneous Determination of Labile Proton Ratio and Exchange Rate. *NMR Biomed* 28(3):376-383.
54. McVicar N, Li AX, Suchý M, et al. (2013) Simultaneous *in vivo* pH and Temperature Mapping using a PARACEST-MRI Contrast Agent. *Magn Reson Med*. 70(4):1016-1025.
55. Albatany M, Li A, Meakin S, Bartha R. (2018) Dichloroacetate Induced Intracellular Acidification in Glioblastoma: *in vivo* Detection Using AACID-CEST MRI at 9.4 Tesla. *J Neurooncol*. 136(2):255-262.
56. Albatany M, Ostapchenko VG, Meakin S, et al. (2019) Brain Tumor Acidification using Drugs Simultaneously Targeting Multiple pH Regulatory Mechanisms. *J Neuro-Oncology* 144(3):453-462.
57. Chen LQ, Howison CM, Jeffery JJ, et al. (2014) Evaluations of Extracellular pH within *in vivo* Tumors using Acidocest MRI. *Magn Reson Med* 72(5):1408-1417.
58. Longo DL, Bartoli A, Consolino L, et al. (2016) In vivo Imaging of Tumor Metabolism and Acidosis by Combining PET and MRI-CEST pH Imaging. *Cancer Res* 76(22):6463-6470.
59. Zaiss M, Anemone A, Goerke S, et al. (2019) Quantification of hydroxyl exchange of D-Glucose at physiological conditions for optimization of glucoCEST MRI at 3, 7 and 9.4 Tesla. *NMR Biomed* 32(9):1-14.
60. Bliemsrieder E, Kaissis G, Grashei M, et al. (2021) Hyperpolarized ¹³C Pyruvate Magnetic Resonance Spectroscopy for *in vivo* metabolic phenotyping of rat HCC. *Sci Reports* 11(1):1-9.
61. Wang ZJ, Ohliger MA, Larson PEZ, et al. (2019) Hyperpolarized ¹³C MRI: State of the art and Future Directions. *Radiology* 291(2):273-284.
62. Yeung TPC, Kurdi M, Wang Y, et al. (2014) CT Perfusion Imaging as an Early Biomarker of Differential Response to Stereotactic Radiosurgery in C6 Rat Gliomas. *PLoS One* 9(10):e109781.
63. Yeung TPC. (2014) Functional Imaging of Malignant Gliomas with CT Perfusion. PhD Thesis.
64. Lee TY, Purdie TG, Steart E. (2003) CT imaging of angiogenesis, *Q K Nucl Med*.

47(3):171-87.

65. Mukai H, Watanabe Y. (2021) Review: PET Imaging with Macro- and Middle-sized Molecular Probes. *Nucl Med Biol* 92:156-170.
66. Gallamini A, Zwarthoed C, Borra A. (2014) Positron Emission Tomography (PET) in Oncology. 14:1821-1889.
67. Vaquero JJ, Kinahan P. (2015) Positron Emission Tomography: Current Challenges and Opportunities for Technological Advances in Clinical and Preclinical Imaging Systems. *Annu Rev Biomed Eng.* 17:385.
68. Jha AK, Purandare NC, Shah S, et al. (2014) PET Reconstruction Artifact can be Minimized by using Sinogram Correction and Filtered Back-Projection Technique. *Indian J Radiol Imaging* 24(2):103.
69. Liu X, Comtat C, Michel C, Kinahan P, et al. (2001) Comparison of 3-D reconstruction with 3D-OSEM and with FORE+OSEM for PET. *IEEE Trans Med Imaging.*;20(8):804-814.
70. Anderson DH. (1983) Compartmental Modeling and Tracer Kinetics. Springer Science & Business Media.
71. Watabe H, Ikoma Y, Kimura Y, et al. (2006) PET Kinetic Analysis-- Compartmental Model. *Ann Nucl Med* 20(9):583-588.
72. van den Hoff J, Hofheinz F, Oehme L, et al. (2013) Dual time point based Quantification of Metabolic Uptake Rates in 18F-FDG PET. *EJNMMI Res* 3(1):1-11.
73. Yang DM, Palma D, Louie A, et al. (2019) Assessment of Tumour Response after Stereotactic Ablative Radiation Therapy for Lung Cancer: A Prospective Quantitative hybrid 18F-fluorodeoxyglucose-positron emission tomography and CT perfusion study. *J Med Imaging Radiat Oncol* 63(1):94-101.
74. Logan J. (2000) Graphical Analysis of PET Data Applied to Reversible and Irreversible Tracers. *Nucl Med Biol.* 27(7):661-670.
75. Padma MV, Said S, Jacobs M, et al. (2003) Prediction of Pathology and Survival by FDG PET in Gliomas. *J Neurooncol* 64(3):227-237.
76. Gunn RN, Gunn SR, Cunningham VJ. (2001) Positron Emission Tomography Compartmental Models. *J Cereb Blood Flow Metab* 21(6):635-652.
77. Keramida G, Hunter J, Peters AM. (2016) Hepatic Glucose Utilization in Hepatic Steatosis and obesity. *Biosci Rep* 36(6):402.

78. Tokugawa J, Ravasi L, Nakayama T, et al. (2007) Operational Lumped Constant for FDG in Normal Adult Male Rats. *J Nucl Med* 48(1):94-99.
79. Backes H, Walberer M, Endepols H, et al. (2011) Whiskers Area as Extracerebral Reference Tissue for Quantification of Rat Brain Metabolism Using 18 F-FDG PET: Application to Focal Cerebral Ischemia. *J Nucl Med* 52:1252-1260. doi:10.2967/jnumed.110.085266
80. Barrio JR, Huang SC, Satyamurthy N, et al. (2020) Does 2-FDG PET Accurately Reflect Quantitative In Vivo Glucose Utilization? *J Nucl Med* 61(6):931-937.

Chapter 2

Multimodality In Vivo Imaging of Perfusion and Glycolysis in a Rat Model of C6 Glioma

Qi Qi, Matthew S. Fox, Heeseung Lim, Robert Bartha, Lisa Hoffman, Timothy J. Scholl, Ting-Yim Lee, Jonathan D. Thiessen

Molecular Imaging and Biology. February 2021, **23**: 516-526, DOI: 10.1007/s11307-021-01585-1

Abstract

Chemical exchange saturation transfer MRI using an infusion of glucose (glucoCEST) is sensitive to the distribution of glucose in vivo; however, whether glucose contrast enhancement (GCE) from glucoCEST is more related to perfusion or glycolysis is still debatable. In this Chapter, we compared glucoCEST to computed tomography perfusion (CTP), [^{18}F] fluorodeoxyglucose positron emission tomography (FDG-PET), and hyperpolarized [$1\text{-}^{13}\text{C}$] pyruvate magnetic resonance spectroscopy imaging (MRSI) in a C6 rat model of glioma to determine if glucoCEST is more strongly correlated with measurements of perfusion or glycolysis. This study determined that glucoCEST is more strongly correlated to measurements of perfusion than glycolysis. GlucoCEST measurements have additional confounds, such as sensitivity to changing pH, that merit additional investigation.

2.1 Introduction

Glioblastoma multiforme (GBM) is both the most common and the most aggressive type of malignant brain tumor. Regardless of technical advances, the median survival period for patients who are diagnosed with GBM, remains approximately 12-15 months [1]. Angiogenesis, the formation of blood vessels, is regarded as one of the hallmarks of GBM. These newly formed vessels facilitate the delivery of nutrients such as glucose to cancer

cells, contributing to the observed increase in tumor metabolism (glycolysis) and ultimately, tumor proliferation [2]. Inevitably, measurements of tumor perfusion and glucose metabolism are interrelated, and are important imaging biomarkers for predicting tumor cell proliferation and assessing treatment response. Chemical exchange saturation transfer (CEST), a magnetic resonance imaging (MRI) technique, may be used to monitor both tumor perfusion and glucose metabolism [3]. In particular, CEST is sensitive to endogenous glucose, potentially allowing us to monitor the change in metabolite concentration over time after an injection of glucose (glucoCEST) [4,5]. Originally, researchers proposed that the change in concentration monitored using glucoCEST in the tumor region was associated with glucose metabolism [6,7]. However, recent studies have shown that these changes are also sensitive to tumor perfusion [8,9].

To evaluate glucoCEST as a surrogate biomarker of tumor perfusion and/or tumor glycolysis, we compared various well-defined *in vivo* perfusion and glycolysis measurements in the C6 rat glioma model. Tumor perfusion maps such as blood flow (BF), blood volume (BV) and permeability surface-area product (PS) were derived with computed tomography perfusion (CTP) measurements acquired during a bolus injection of iodinated contrast agent (Isovue). Glucose metabolism was evaluated with positron emission tomography (PET) and ^{18}F -fluorodeoxyglucose (FDG), a glucose analogue which is phosphorylated in the cell but doesn't go through subsequent steps of glycolysis. Aerobic glycolysis was measured with MR spectroscopic imaging (MRSI) after an injection of hyperpolarized [1- ^{13}C]pyruvate.

2.2 Methods

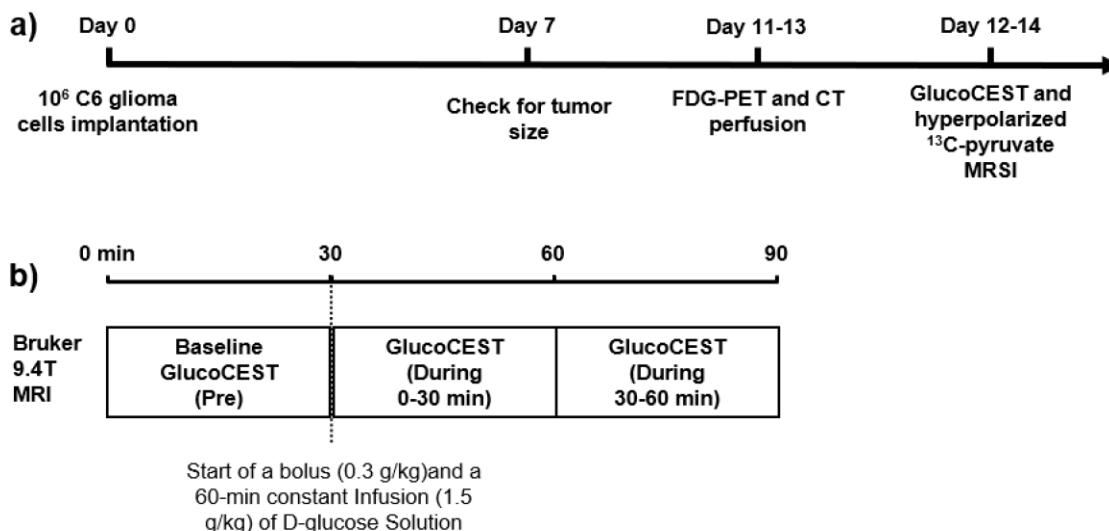


Figure 2.1: **a)** Study overview. Day 0 corresponds to the tumor cell implantation. A CT perfusion check was performed on Day 7 to monitor if the tumor had reached optimal size (diameter > 4 mm). An FDG-PET acquisition followed by CT perfusion experiment was carried out between Days 11 and 13. The glucoCEST experiment and hyperpolarized ^{13}C -pyruvate MRSI took place on the following day (Days 12 to 14). **b)** Dynamic CEST experiment. There were three CEST acquisitions: a baseline CEST acquisition (Pre), a second CEST acquisition during the first 30 minutes of glucose infusion (During 0-30 min) and a final CEST acquisition during the last 30 minutes of glucose infusion (During 30-60 min).

The experimental timeline is shown in **Figure 2.1a**. In short, C6 glioma tumor cells were implanted on Day 0. A CT perfusion check was performed on Day 7 to check if the diameter of the tumor has reached 4 mm [10-12]. FDG-PET followed by CT perfusion acquisition were performed between Day 11-13 after C6 cell implantation. GlucoCEST MRI followed by hyperpolarized $[1-^{13}\text{C}]$ pyruvate MRI experiments were performed on the next day immediately prior to euthanization. All imaging experiments took place within a span of 24 hours for each animal: FDG-PET and CT perfusion in the afternoon/evening, followed by 9.4T MRI (glucoCEST) and 3T MRI (hyperpolarized MRSI) in the morning/afternoon of

the subsequent day. All procedures were performed in compliance with the Canadian Council for Animal Care and approved by the Western University Animal Care Committee.

2.2.1 C6 glioma model

Male Wistar rats (Charles River, Canada, age 8 to 10 weeks at surgery) weighing on average 401 ± 42 g ($N = 11$) were used in this study. The animals were induced with 5% isoflurane and were maintained at 2-3% for all surgical and imaging procedures.

C6 glioma cells (CCL-107, American Type Culture Collection, Manassas, VA) were cultivated in F12k 15% horse serum, 2.5% bovine serum, and 1% penicillin-streptomycin. Animals were placed into a stereotactic surgical frame during C6 glioma cell implantation. The animals were anesthetized with 2% isoflurane and were injected with Metacam (Boehringer Ingelheim Vetmedica Inc, Duluth, US, 10 mg/kg). The bregma was exposed after a scalp incision; a 1-mm-diameter burr hole was drilled at a point 1 mm anterior and 3 mm right of the bregma. A total of 10^6 C6 glioma cells suspended in 10 μ L were slowly injected over a period of 5 minutes at a depth of 3–4 mm from the skull surface with a Hamilton syringe. The burr hole was sealed with bone wax, and the scalp was closed with sutures. The subjects were recovered and returned to animal care housing where they received an additional subcutaneous injection of Metacam (10mg/kg) 12 hours after surgical recovery.

2.2.2 CT perfusion imaging and analysis

Detailed CT perfusion acquisition and analysis procedures can be found in previous research publications [10,11]. In short, a non-contrast CT scan was performed prior to the perfusion scan to identify sixteen slices covering the entire brain with each section 1.25 mm thick (GE Discovery RCT). CT perfusion data were acquired over two back-to-back time periods. A fine temporal resolution (1.4 s intervals) was used during the first time period (32 s duration) and a coarse temporal resolution (15 s intervals) was used in the second period (165 s duration). 2-3 s after the start of the first phase a bolus of contrast (Isovue,

Bracco Diagnostics Inc, Vaughan, Canada, 300 mg iodine/mL, 2.5 mL/kg body weight) was injected into a lateral tail vein at a rate of 0.13 mL/s using a syringe pump (New Era Pump Systems, Inc, Farmingdale, NY, USA). The scan parameters were 80 kVp, 120 mAs, 10 cm field-of-view with a high-definition bone filter. A change of CT number as a function of time can be measured using the dynamic series of CTP images. The subjects were able to proceed to the subsequent experiments when the axial diameter of the tumor reached 4 mm [11,12]. The CT perfusion measurements that were used in the perfusion analysis were acquired Day 11-13 on a clinical CT scanner (Discovery 750 HD, GE Healthcare, Waukesha, WI) after a 75-minute dynamic FDG-PET acquisition.

CT Perfusion 5 (GE Healthcare) was used to generate maps of BF, BV, and PS. The time attenuation curve (TAC) from the carotid artery was selected as the arterial input. The arterial TAC was deconvolved with tissue TACs measured from 2×2 pixel blocks of CT images using the Johnson-Wilson model to calculate maps of BF, BV, and PS [12,13]. As described in **Chapter 1**, the tissue-enhancement curve can be expressed as the convolution between the blood flow-scaled impulse residue function (IRF), $BF \cdot R(t)$, and the arterial TAC, $C_a(t)$. The shape of the BF-scaled IRF has two distinct phases, and it is solved by deconvolving the arterial TAC with the tissue-enhancement curve. The plateau of the BF-scaled IRF defines the BF, while the area under the first phase of the BF-IRF is the BV. The second phase of the BF-scaled IRF starts at the height of the extraction fraction, which is the fraction of contrast agent that leaks into the interstitial space. The second phase of the BF-scaled IRF decays with time, and PS can be calculated as $PS = -BF \times \ln(1 - E)$, E is the extraction fraction.

2.2.3 FDG-PET imaging

The FDG-PET acquisition took place 11-13 days after the surgery on a small animal PET system (Inveon DPET, Siemens Healthineers, Knoxville, TN, USA). The blood glucose level of each subject was tested using a glucometer prior to FDG-PET acquisition (CONTOUR meter, Ascensia Diabetes Care, Parsippany, NJ, USA). A 75-minute emission

scan was performed with a timing window of 3.432 ns and 350-640 keV discrimination energy range. Longitudinal PET data were binned into successive time intervals comprised of 10 frames of 30 s, 5 frames of 60 seconds, 10 frames of 300 seconds and 1 frame of 900 seconds, totaling 75 minutes. An iterative, 3D ordered subset expectation maximization (OSEM3D) reconstruction was used to generate dynamic images for all frames with 2 iterations and 18 subsets. Approximately 30 s after the acquisition had started, a bolus of ^{18}F -FDG (31.5 ± 3.1 MBq) was injected through a lateral tail vein. Anatomical CT images acquired after the PET acquisition were used to generate attenuation corrected PET images. The CT images were co-registered with the PET images using ASIPro (Siemens Healthineers, Knoxville, TN, USA). The co-registered CT images were used to generate a mu-map by converting Hounsfield units into linear attenuation coefficients for 511 keV gamma rays. The mu-map was then converted into an attenuation sinogram. The PET images were reconstructed using the attenuation sinogram to create the attenuation corrected PET images.

Standardized uptake values (SUV) were calculated using the last 15 minutes of the dynamic PET images as a surrogate for glucose metabolism. SUV was defined as $\text{SUV} = \text{Activity Concentration of ROI} / (\text{Injected Dose} / \text{Weight of the Subject})$ [14].

2.2.4 Dynamic glucoCEST imaging

MRI was acquired on a 9.4-T small animal MRI (Agilent, Palo Alto, CA, USA) the day after PET/CT (12 – 14 days after the surgery). Axial T_2 -weighted images using a 2-dimensional fast spin-echo (FSE) sequence (repetition time, $\text{TR} = 3000$ ms; echo time, $\text{TE} = 10$ ms; effective $\text{TE} = 40$ ms; echo train length = 4; number of slices = 29; slice thickness = 1 mm; field-of-view, $\text{FOV} = 3.84 \times 3.84$ cm; matrix size = 128×128 ; acquisition time ≈ 3 min) were acquired first to locate the slice axially that contained the largest tumor cross-section. CEST spectra were acquired using a continuous wave pre-saturation pulse (saturation time, $\text{TS} = 5$ s; B_1 saturation pulse amplitude = $1.6 \mu\text{T}$; offset frequency pulse alternated between negative and positive, from $-5/+5$ to 0 ppm with 0.2

ppm steps) preceding a series of FSE images acquired on the axial slice that contained the largest tumor cross-section (TR = 3 s, effective TE = 40 ms, echo train length = 32, slice thickness = 2 mm, FOV = 3.84 x 3.84 cm FOV, matrix size = 128 x 128; acquisition time \approx 30 min). Three spectra were obtained from three consecutive 30 min CEST acquisitions. The first CEST spectrum was acquired prior to a 20% D-glucose infusion. A bolus of 20% D-glucose solution (0.3 g/kg) was injected at the end of the first spectrum acquisition, following by a 60-minute constant infusion of the same 20% D-glucose solution (1.5 g/kg/hour). The acquisition of the second and third CEST spectra corresponded to the first and second half of the constant infusion of glucose, respectively. The CEST imaging workflow is illustrated in **Figure 2.1b**.

All CEST data were analyzed using MATLAB 2018b. A mask of the brain was delineated using the T₂-weighted MR images and applied to the CEST images. A smoothing spline with a fitting parameter of 0.998 was used to generate Z-spectra at each pixel using all 53 CEST images. B₀ correction was performed by shifting the frequency associated with the Z-spectra minima to 0 ppm. A magnetization transfer ratio asymmetry (MTR_{asym}) spectrum [15] at each pixel was calculated as shown in **Equation 2.1**.

$$\text{MTR}_{\text{asym}} = \frac{S(-\Delta\omega) - S(\Delta\omega)}{S_0} \quad [2.1]$$

The area under the curve (AUC) was calculated using MTR_{asym} (AUC_{MTR}) values from 1.2 to 2.8 ppm [6] and the relative change after glucose infusion was calculated as ΔCEST (see **Equation 2.2**). Note that AUC_(during-infusion) corresponds to the last 30 minutes of the glucose infusion (the third CEST spectra), as a different imaging protocol was used in some of the experiments while the blood glucose was still increasing in the first 30 minutes of the

$$\Delta\text{CEST} = \frac{\text{AUC}_{(\text{during-infusion})} - \text{AUC}_{(\text{pre-infusion})}}{\text{AUC}_{(\text{during-infusion})}} \quad [2.2]$$

glucose infusion.

2.2.5 Hyperpolarized [1-¹³C]pyruvate

Detailed hyperpolarization and imaging procedures can be found in Lim *et al.* [16]. Rats were transported to a GE Discovery MR750 3.0-T MRI (General Electric Healthcare, Waukesha WI, U.S.A.) under anesthesia with 2% isoflurane immediately after the glucose CEST experiment. An FSE sequence (80 x 80 mm FOV, 0.3-mm in-plane resolution, 3-mm slice thickness, TR = 4000 ms, TE = 85 ms, 16 echo trains and 9 averages) was used to acquire axial T₂-weighted ¹H images which were later used to determine the axial slice(s) that contained the tumor and located at the approximate the same location using the CEST slice information. ProHance gadolinium contrast agent (Bracco Diagnostics, Monroe Township, NJ, USA) was added at a concentration of 1 mM to [1-¹³C]pyruvic acid (Sigma Aldrich, Miamisburg OH, USA), and the sample was hyperpolarized using a HyperSense dynamic nuclear polarizer (DNP, Oxford Instruments, Abingdon, UK). The resulting buffered hyperpolarized [1-¹³C]pyruvate solution (80 mM) had a final volume of ~4 ml with a pH of 7.4 at 37°C. A 3-ml volume of hyperpolarized [1-¹³C]pyruvate solution was rapidly transferred to the MRI where it was injected through a lateral tail vein of the rat in a single 12-second bolus. After waiting a further 13 seconds for circulation and metabolism, ¹³C spectra in the axial plane (12 x 12 spectral imaging matrix, TR=80 ms, bandwidth = 5 kHz, 2048 pts, flip angle = 10°) were acquired using a 2D chemical shift imaging with a free induction decay, chemical shift imaging (FID-CSI) pulse sequence (60 x 60 mm FOV, slice thickness approximately equal to the tumor extent). One FID-CSI with 144 spectra was acquired in each animal with a total scan time of 12 seconds. Regional maps of the ratio of lactate to pyruvate (Lac:Pyr) were calculated using a customized MATLAB script [16]. The animal was euthanized immediately after the experiment.

2.2.6 Benchtop blood glucose measurement

The blood glucose change was measured by sampling blood from a rat tail artery (weight = 508 g) with a glucometer (Contour 7152B, Bayer HealthCare, Leverkusen, Germany) on the benchtop using the same glucose infusion protocol as the glucoCEST experiment.

Baseline blood glucose was measured before the injection of 20% glucose solution (0.3 g/kg) and the start of a 60-min constant infusion (1.5 g/kg). The blood glucose of the subject was measured every 5 minutes after the start of glucose infusion.

2.2.7 ROI selection and image registration

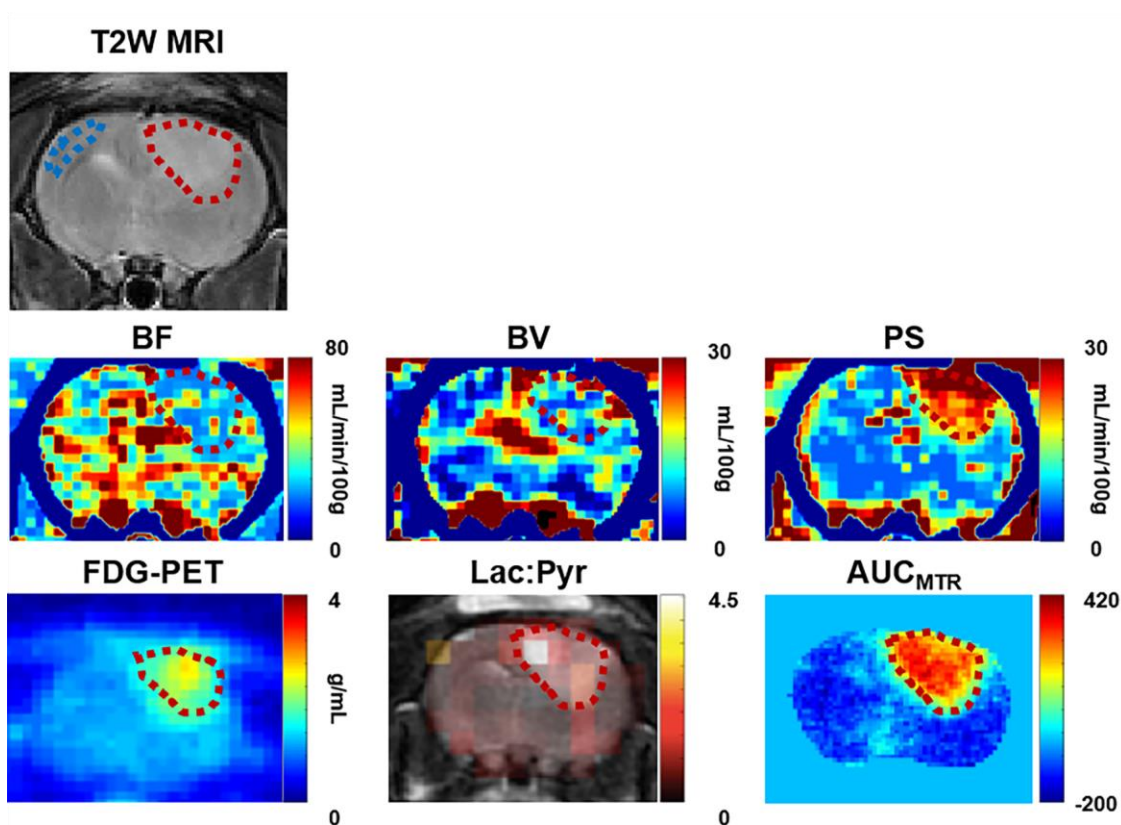


Figure 2.2: Example images and ROIs in a single rat. A T_2 -weighted 9.4 T MR image (T2W) was used as a reference to co-register CT perfusion maps (BF, BV, PS), FDG-PET, CEST maps (AUC_{MTR}), and hyperpolarized $[1-^{13}C]$ pyruvate MRSI (Lac:Pyruvate). The T2W image was subsequently used to delineate tumor (red dotted line) and contralateral brain tissue (blue dotted line), with the same ROI applied to all imaging measurements.

Tumor volume was measured on both imaging days using CT perfusion and T_2 -weighted MRI datasets, respectively. T_2 -weighted MRI was used as guidance for manual delineation of tumor and contralateral brain regions. All voxels that contained tumor were included in the tumor ROIs. The T_2 -weighted MRI was also used as a reference to co-register the CT

perfusion, CEST, FDG-PET and hyperpolarized [$1\text{-}^{13}\text{C}$]pyruvate images using 3D Slicer (www.slicer.org). Manual rigid registration relied on anatomical landmarks identified in both T_2 -weighted images (e.g. major white matter features such as the corpus callosum, ventricles, and brain surface), features in the anatomical and perfusion CT (tumour, brain surface, and skull), and uptake in the FDG-PET volume (tumour uptake and normal uptake in the brain, Harderian glands, and surrounding tissue). The T_2 -weighted image from the 9.4T MRI was subsequently used for ROI delineation and applied to all of the co-registered parameter maps (CEST, MRSI, CTP, and FDG-PET). The average BF, BV and PS values from CT perfusion measurements; average ΔCEST measurement from glucoCEST; SUV from FDG-PET; and Lac:Pyr ratios from hyperpolarized [$1\text{-}^{13}\text{C}$]pyruvate MRSI in tumor and contralateral brain regions were extracted. An example of registered images and ROIs are shown in **Figure 2.2**.

2.2.8 Statistical analysis

Paired T-tests were used to compare the similarity of CT perfusion, CEST, FDG-PET and hyperpolarized [$1\text{-}^{13}\text{C}$]pyruvate measurements between the tumor and contralateral brain regions. Paired T-tests were also performed on the voxel-wise AUC_{MTR} values in the tumor pre-infusion and during-infusion in order to determine significant changes in AUC_{MTR} during glucose infusion in each subject. The Pearson correlation between average tumoral CT perfusion parameters, ΔCEST measurement from glucoCEST, SUV from FDG-PET and Lac:Pyr ratios from hyperpolarized [$1\text{-}^{13}\text{C}$]pyruvate MRSI were evaluated using IBM SPSS version 22. A P value ≤ 0.05 was considered statistically significant.

2.3 Results

2.3.1 Tumor size

As shown in **Figure 2.3**, the average tumor volume on the day of PET and CT perfusion measurements was $98.4 \pm 37.5 \text{ mm}^3$ (measured using PS and contrast-enhanced images from CT perfusion), and the average tumor volume on the day of CEST and hyperpolarized $[1-^{13}\text{C}]$ pyruvate measurements was $99.4 \pm 39.5 \text{ mm}^3$ (measured in 9.4T T₂-weighted MRI), with no significant difference in volume between the two imaging days based on a paired t-test ($P = 0.54$).

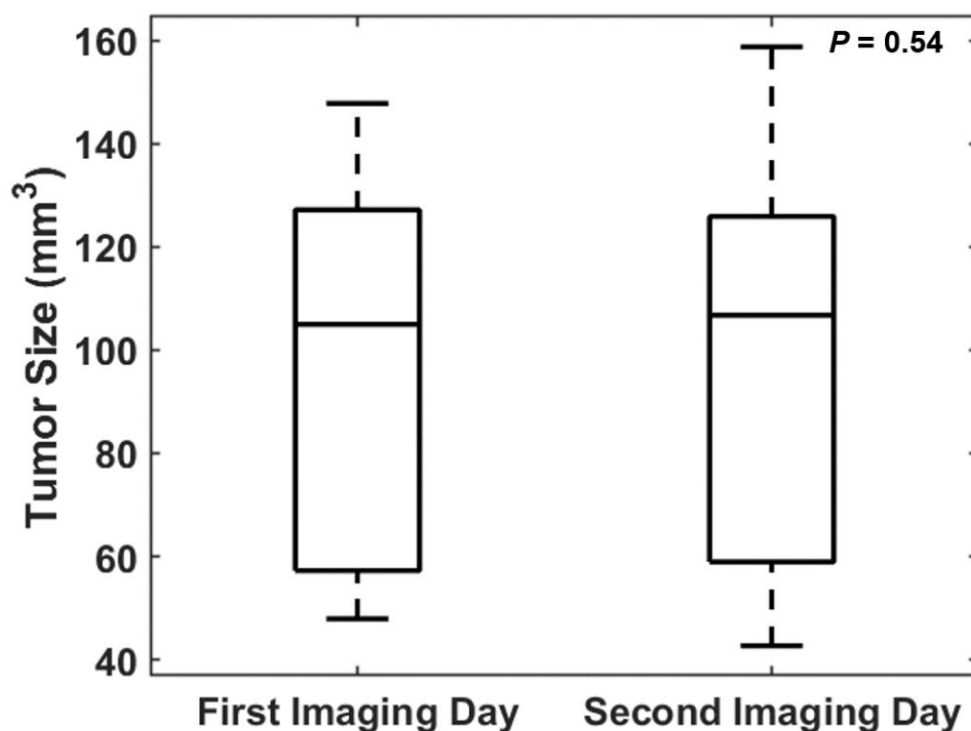


Figure 2.3: Average tumor size on first imaging day for PET and CT perfusion experiment and the next day for glucoCEST and hyperpolarized $[1-^{13}\text{C}]$ pyruvate. No statistical significance in tumor size were found between these two subsequent imaging days ($P = 0.54$). Error bars = standard deviation

2.3.2 Blood glucose measurements

Benchtop measurements of blood glucose as a function of time during the glucose infusion protocol are plotted in **Figure 2.4**. The baseline blood glucose of the subject was 7.3 mmol/L and slowly increased to >20 mmol/L during the 60-minute constant infusion. Blood glucose was 7.6 ± 1.8 mmol/L prior to the FDG-PET and CT perfusion measurements and 6.7 ± 1.3 mmol/L prior to the CEST and hyperpolarized [$1\text{-}^{13}\text{C}$]pyruvate measurements.

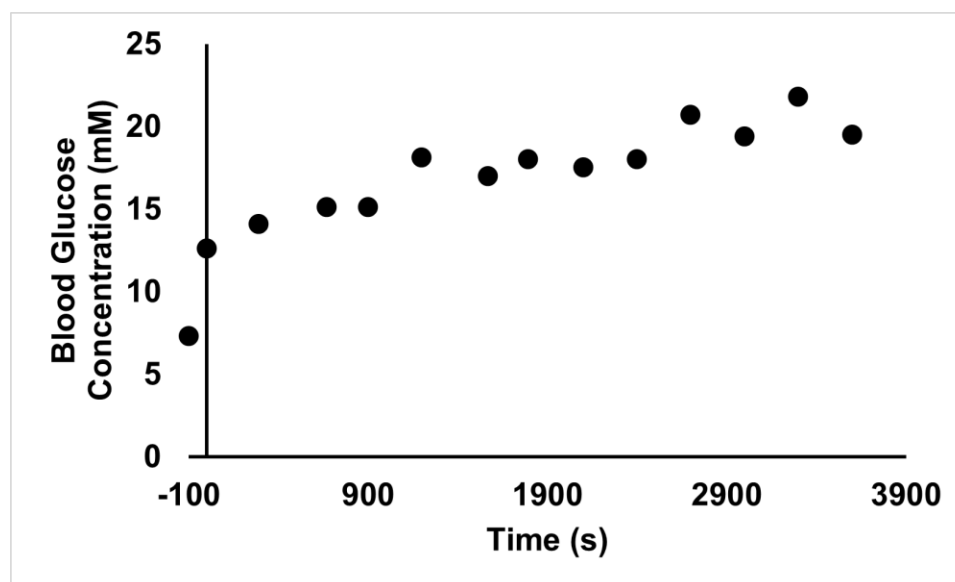


Figure 2.4: An illustrative example of blood glucose change during the 60-min constant infusion. Time 0 was defined as the time at the start of constant infusion of 20% glucose solution (1.5 g/kg) and after a bolus of 20% glucose solution (0.3 g/kg) was injected.

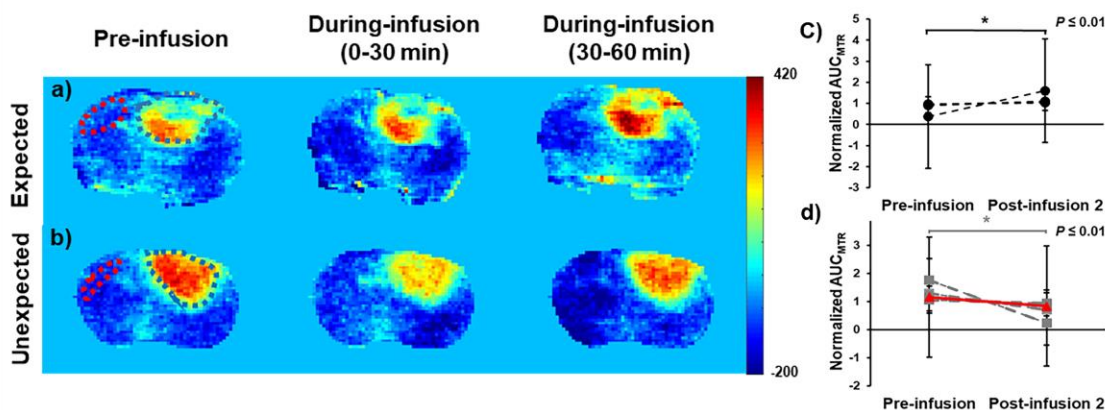


Figure 2.5: Illustrative examples of two different trends observed from the dynamic glucoCEST measurements: **a)** expected and **b)** unexpected change in AUC_{MTR} . The expected trend was observed in 5 subjects and is shown in **c)**, where during-infusion AUC_{MTR} values are significantly higher than pre-infusion AUC_{MTR} . The unexpected trend was observed in 6 subjects and is shown in **d)**, where during-infusion AUC_{MTR} is significantly lower ($n = 5$, grey-dotted line) than or is not significantly different ($n = 1$, red line, $P = 0.46$) from pre-infusion AUC_{MTR} . Error bars = standard deviation.

2.3.3 Dynamic CEST trends

No significant change in applied frequency shifts ($P = 0.52$) was found between pre- (-0.09 ± 0.05 ppm) and during glucose infusion (-0.10 ± 0.04 ppm). Two different trends were observed in the dynamic CEST results (**Figure 2.5**). A significantly increased AUC_{MTR} in the tumor region at 30-60 minutes during-infusion compared to the pre-infusion AUC_{MTR} was denoted as an expected trend ($n = 5$). Significantly decreasing ($n = 5$) or no significant change ($n = 1$) in AUC_{MTR} in the tumor region was denoted as an unexpected trend.

2.3.4 Tumor vs. contralateral brain tissue

After comparing CEST, perfusion and glycolysis measurements: no statistically significant difference was found in BF and Δ CEST between tumor and contralateral brain tissue ($P =$

0.069 and 0.45 respectively) as shown in **Figure 2.6a and 2.6f** (the pixel-wise Δ CEST values in contralateral region that were more than 2 standard deviations away from the mean were discarded as noise); statistically significant increases in BV ($P < 0.05$), PS ($P < 0.001$), SUV ($P < 0.001$) and Lac:Pyr ($P < 0.001$) were found in the tumor region vs.

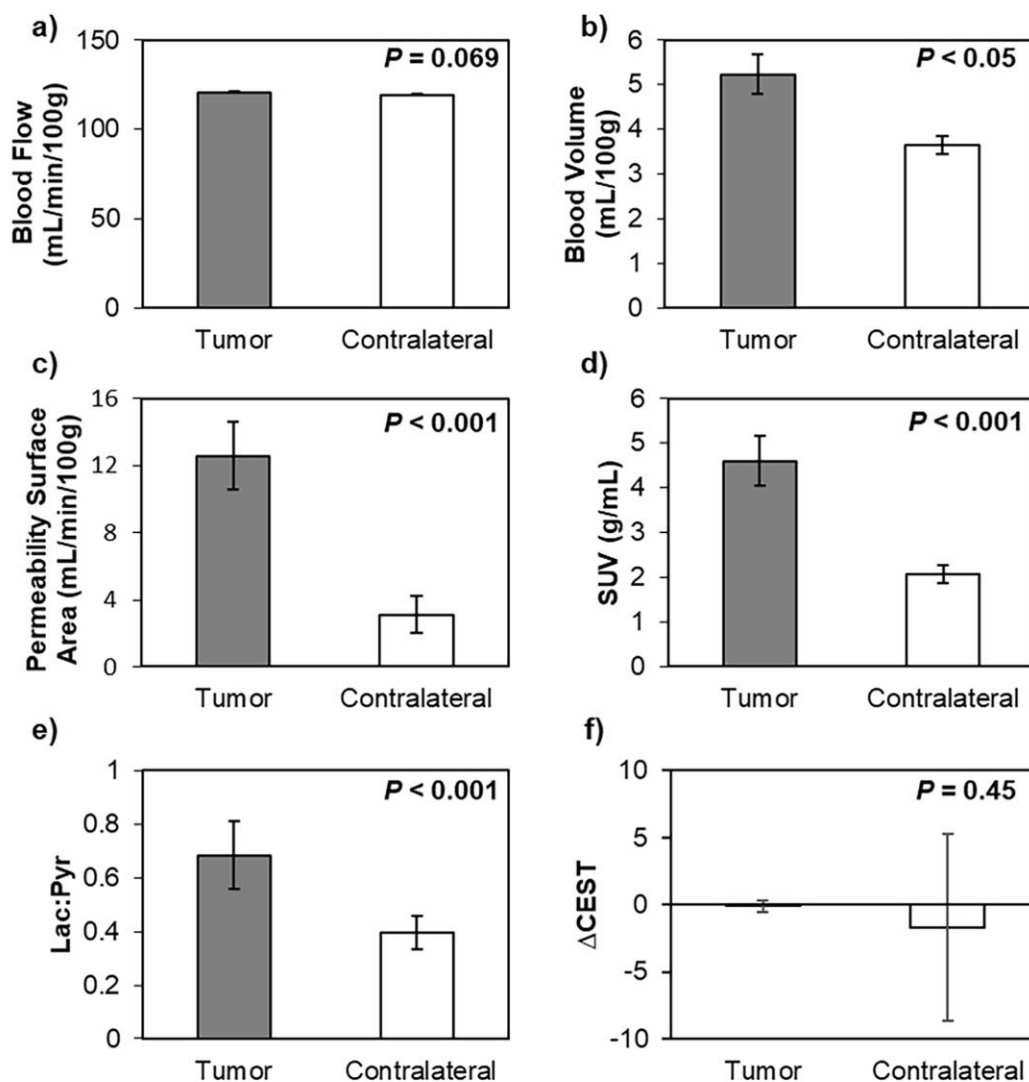


Figure 2.6: Mean values from ROIs defined in both tumor and contralateral brain tissue in CT perfusion maps (a) BF, b) BV and c) PS), d) FDG-PET (SUV), e) hyperpolarized [^{13}C]pyruvate (Lac:Pyr) and f) glucoCEST (Δ CEST). A statistically significant ($P < 0.05$) difference was found in BV, PS, SUV and Lac:Pyr between tumor and contralateral brain. No statistically significant difference was found in BF and Δ CEST between tumor and contralateral brain tissue. Error bars = standard

contralateral brain tissue as shown in **Figure 2.6b–e**. The tumor AUC_{MTR} in both pre- and during-infusion were significantly higher than the contralateral side ($P < 0.001$) as shown in **Figure 2.7**.

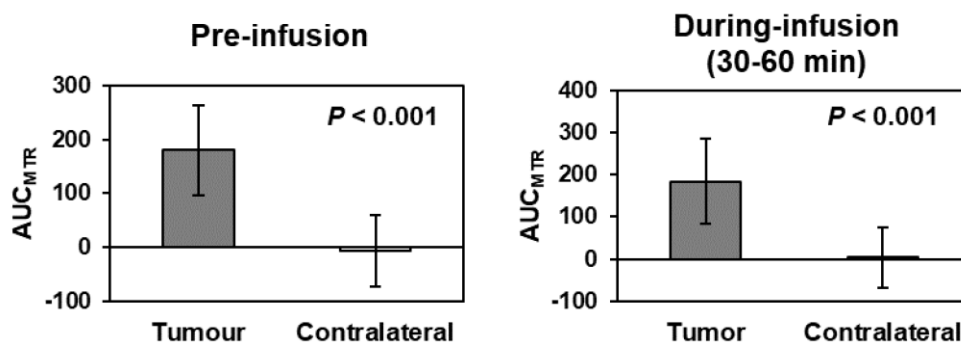


Figure 2.7: Mean values from ROIs defined in both tumor and contralateral brain tissue in AUC_{MTR} pre- and During-infusion (30-60 min). A statistically significant ($P < 0.05$) difference was found between tumor and contralateral side in AUC_{MTR} pre- and during glucose infusion.

2.3.5 CEST vs. perfusion and glycolysis

Δ CEST measurements had statistically significant and strong correlations with CT perfusion measurements of BV (0.74, $P = 0.01$) and PS (0.55, $P = 0.04$) however, no statistically significant correlations were found between BF and Δ CEST ($P = 0.27$). The Pearson correlation coefficients between Δ CEST and CT perfusion measurements are shown in **Table 2.1**. Δ CEST was directly proportional with BV and PS as shown in **Figure 2.8a** and **2.8b** respectively.

No statistically significant correlations between Δ CEST and glycolysis measurements using FDG-PET or hyperpolarized $[1-^{13}\text{C}]$ pyruvate were found (**Table 2.1**).

2.3.6 Glycolysis vs. perfusion measurements

As shown in **Table 2.1**, statistically significant moderate correlations between FDG-PET measurements of SUV and CT perfusion measurements of BF (0.49, $P = 0.02$) and PS (0.58,

$P = 0.005$) were found. SUV was directly proportional with BF and inversely proportional with PS as shown in **Figure 2.8c** and **2.8d** respectively.

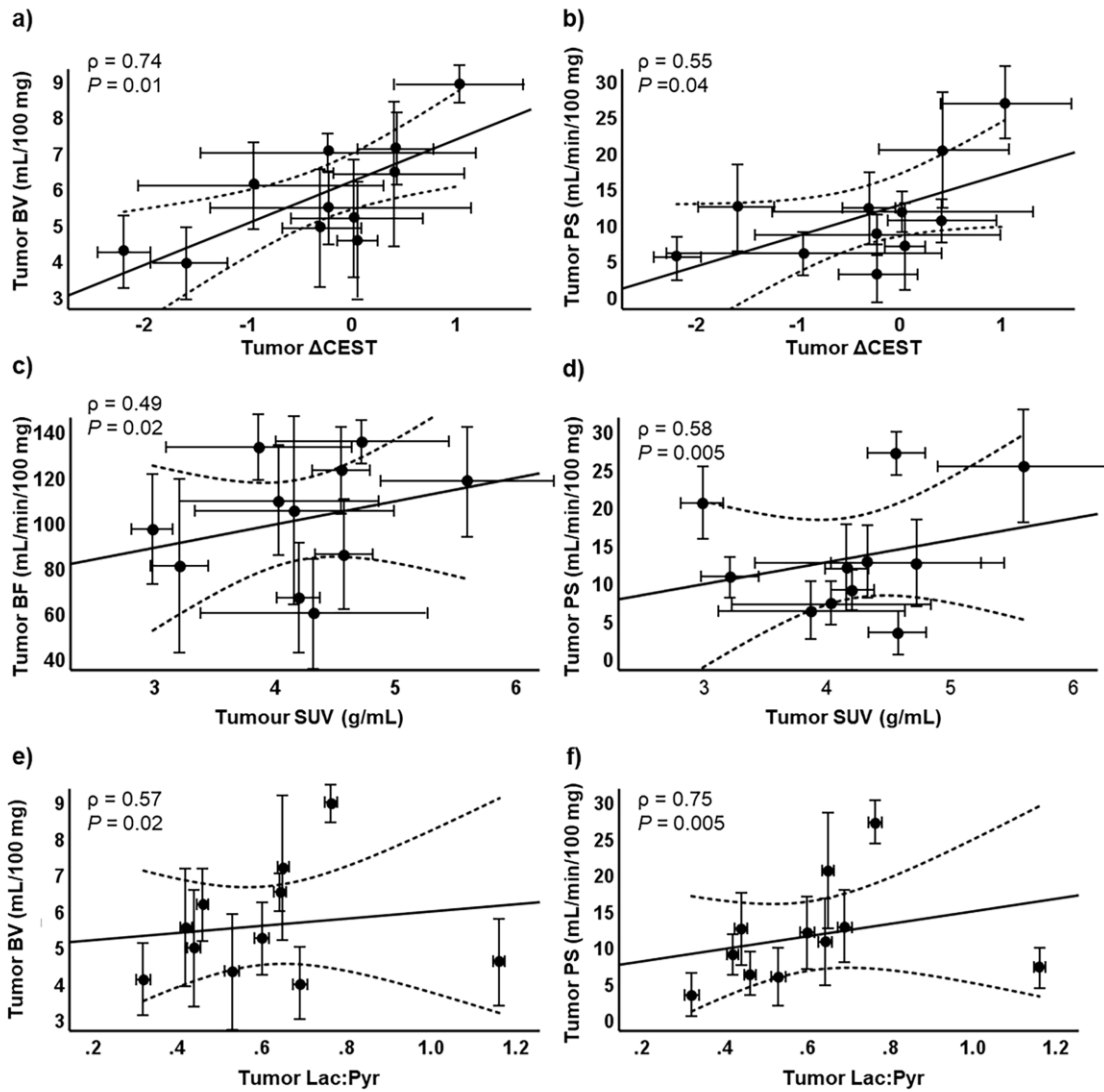


Figure 2.8: Δ CEST vs. blood volume (**a**) and permeability-surface area product (**b**). Tumor SUV vs. blood flow (**c**) and permeability-surface area product (**d**). Tumor Lac:Pyr vs. blood volume (**e**) and permeability-surface area product (**f**). Solid line indicates the best fit and the dotted lines denote 95% confidence interval. Error bar = standard deviation.

Statistically significant moderate correlations between hyperpolarized $[1-^{13}\text{C}]$ pyruvate measurements of Lac:Pyr and CT perfusion measurements of BV (0.57 , $P = 0.02$) and PS (0.75 , $P = 0.005$) were also found (**Figure 2.8e** and **2.8f**).

As expected, there was a statistically significant moderate correlation between Lac:Pyr and SUV (0.56, $P = 0.038$).

It is important to note that the blood glucose conditions were different prior to the two glycolysis measurements: the average blood glucose level was 7.6 ± 1.8 mmol/L before FDG-PET acquisition, whereas the average blood glucose level was above 33 mmol/L prior to hyperpolarized $[1-^{13}\text{C}]$ pyruvate MRSI.

Table 2.1: Pearson correlation coefficients between CT perfusion (BF, BV and PS), FDG-PET (SUV), hyperpolarized $[1-^{13}\text{C}]$ Pyruvate (Lac:Pyr) and glucoCEST (Δ CEST) measured in the tumor. * indicates P value < 0.05 .

N = 11	BV				
BF	0.15	BF			
PS	0.57	0.33	PS		
SUV	0.32	0.49*	0.58*	SUV	
Lac:Pyr	0.57*	0.26	0.75*	0.56*	Lac:Pyr
Δ CEST	0.74*	0.24	0.55*	-0.23	0.28

2.3.7 Expected vs Unexpected group

As indicated in **Table 2.2**, in the expected group, a significant correlation between Δ CEST and PS was found (0.60, $P = 0.032$), but no significant correlations were found between other measurements. No significant correlations were found in the unexpected group, as shown in **Table 2.3**.

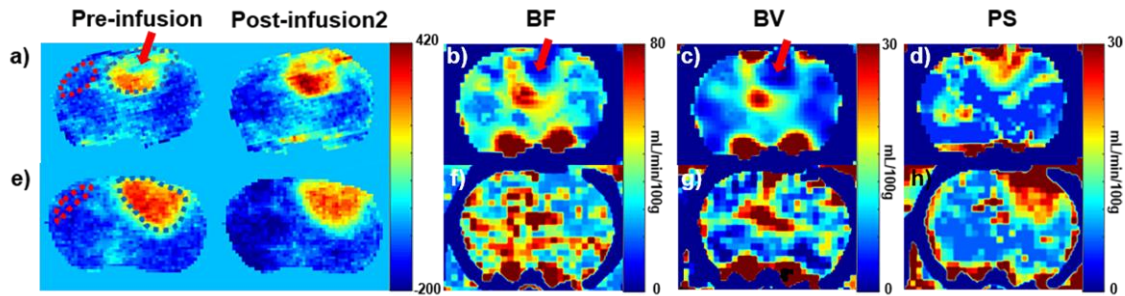


Figure 2.9: Good colocalization of the tumor region is displayed in AUC_{MTR} and PS maps. Similarly, co-localization of potential necrosis is shown among AUC_{MTR} , BF and BV maps (red arrow).

Table 2.3: Pearson correlation coefficients between CT perfusion (BF, BV and PS), FDG-PET (SUV), hyperpolarized $[1-^{13}C]$ Pyruvate (Lac:Pyr) and glucoCEST (Δ CEST) measured in the tumor for the unexpected group. * indicates P value < 0.05 .

N = 5	BV				
BF	0.12	BF			
PS	0.81	-0.29	PS		
SUV	0.75	0.36	-0.79	SUV	
Lac:Pyr	-0.10	-0.25	0.51	0.37	Lac:Pyr
Δ CEST	0.54	0.20	0.61	-0.32	0.55

Table 2.2: Pearson correlation coefficients between CT perfusion (BF, BV and PS), FDG-PET (SUV), hyperpolarized $[1-^{13}C]$ Pyruvate (Lac:Pyr) and glucoCEST (Δ CEST) measured in the tumor for the expected group. * indicates P value < 0.05 .

N = 5	BV				
BF	-0.32	BF			
PS	0.57	0.33	PS		
SUV	-0.64	0.18	0.55	SUV	
Lac:Pyr	0.11	-0.18	0.51	0.45	Lac:Pyr
Δ CEST	0.23	-0.18	0.60*	-0.43	0.15

2.4 Discussion:

In this study, the association between perfusion and glycolysis was investigated *in vivo* in the C6 rat model using CTP, FDG-PET, glucose CEST, and hyperpolarized [1-¹³C]pyruvate MRSI. All imaging experiments were performed within 24 hours and the tumor size did not significantly change within the 24-hour span.

Tumor Δ CEST values were both significantly correlated and directly proportional to CT perfusion measurements of BV and PS. Increased BV in the tumor would correspond to a higher blood fraction in the measurement, where glucose concentration will be the highest, and a corresponding increase in glucose available to the tumor – both reflected by increased Δ CEST values. Tumor PS represents the leakiness of the tumor. Higher PS or leakiness would lead to increased glucose delivery throughout the constant infusion of glucose. No significant correlation was found between tumor Δ CEST measurements and tumor perfusion measurements of BF. This could be due to tumor heterogeneity as brain tumors will contain a mixture of viable, hypoxic and necrotic regions [17]. The AUC_{MTR} maps generated both pre- and during-infusion of glucose most strongly resembled the PS maps, as illustrated in **Figure 2.9**. According to previous work, lower intensity regions on BV and BF maps are associated with tumor necrosis [10], however, only one subject had an AUC_{MTR} that resembled tumor necrosis co-localized with reduced BV and BF indicative of possible necrosis within the tumor region (**Figure 2.9 a-c**). Studies have shown CEST can distinguish tumor necrosis based on decreased MTR values from amide, attributed to decreased endogenous proteins and peptides in necrotic tissue [17, 18]. CEST measurements from this study could potentially identify tumor necrosis more accurately compared to our CTP measurements of BF and BV as MRI has superior soft tissue contrast [19]. No significant correlations were found between Δ CEST and tumor glycolysis measurements of SUV or Lac:Pyr ratio. Previous studies have suggested that D-glucose CEST enhancement comes from plasma and extracellular/extravascular spaces [6,21], whereas SUV and Lac:Pyr ratios will correspond to glucose transport and metabolism in the cell. Our study provides important additional evidence that D-glucose enhanced

Δ CEST is more sensitive to perfusion changes than glycolysis. However, CEST measurements of the immediate response during glucose infusion was missing because CEST experiments for the first 30 minutes of the glucose infusion were performed with two different protocols.

The tumor perfusion measurements of PS significantly correlated with glycolysis measurements of SUV and Lac:Pyr ratio. PS or leakiness is also related to the aggressiveness of the tumor [22]. Higher PS values (i.e. leakier tumors) are associated with more aggressive tumors and more aggressive tumors would have a higher metabolism, hence a directly proportional relationship was found between tumor PS and glycolysis measurements. A moderate but significant correlation was found between tumor BF and SUV and tumor BV and Lac:Pyr ratio. Higher tumor blood flow and blood volume could indicate increased vascularity, allowing more nutrients to be transferred to the tumor for glycolysis. Due to the sequential design of the study, glucose conditions before FDG-PET (normoglycemic) were distinct from the hyperpolarized [1-¹³C]pyruvate experiment (hyperglycemic) since it was conducted on the next day and immediately followed the glucose CEST experiment, as a result, Lac:Pyr and SUV provided different glycolysis measurements. In a recent study by Hundshammer *et al.* investigating a subcutaneous breast cancer model in rats, there was moderate correlation between SUV_{mean} and the Lac:Pyr (0.41) that improved when looking at tumors with similar apparent diffusivity coefficients (0.59) [23]. This is quite similar to the correlation we found between SUV and Lac:Pyr (0.56) in our glioma model. Glucose and pyruvate take distinct metabolic pathways [23], which may help explain the moderate but not strong correlation between the two measurements. In our study, hyperglycemia, tumor glycolytic activity and lactate production will be elevated during the hyperpolarized [1-¹³C]pyruvate experiment, while mitochondrial activity and lactate oxidation will be suppressed [24, 25]. Because of the hyperglycemic conditions, more pyruvate produced from glycolysis will be produced and later converted to lactate acid, which may help explain the slightly stronger correlation we found between Lac:Pyr and SUV.

The dynamic changes of AUC_{MTR} for all subjects are shown in **Figure 2.5c**. Two different trends were found from the dynamic CEST experiment as shown in **Figure 2.5a** and **2.5b**. The expected trend illustrated an increasing intensity over the time of glucose infusion in the tumor region, assuming the glucose solution would act as either a glucose metabolism or perfusion contrast agent. An increase of glucose CEST signal in the tumor region was expected due to the increased glucose concentration caused by a constant infusion of glucose. Dynamic CEST maps at later infusion times appear to enhance the boundary between necrotic and viable tumor areas as shown in **Figure 2.5a**. The glucose infusion captured the leaky vessels of the viable tumor region, helping to facilitate glucose perfusion and enhancing the contrast between viable tumor and necrotic tumor areas. In some cases, however, the CEST map would decrease after the start of the glucose infusion (**Figure 2.5b**). The mechanisms for the unexpected decrease in CEST signal need to be elucidated in future studies but may be related to the complex vascularity of the tumor, the insulin response and/or changes in tumor pH induced by the glucose infusion.

There are several limitations for this experiment. Large tumors will often encompass the ventricles, as a result, the ROI defined using the T_2 -weighted MRI will contain CSF. The inclusion of CSF in tumor ROIs could lead to underestimation of all measurements in the tumor regions as CSF is distinct from the contrast agent in the blood vessels and tissue. Although histology was not performed, in a previous study using the same C6 tumor model [10] we demonstrated the relationship between tumor perfusion measurements and tumor hypoxia and necrosis using CT perfusion and corresponding histology data. We found that CT perfusion measurements of BF and BV are associated with tumor necrosis and hypoxia: regions with higher values of BF and BV representing viable tumor would surround regions with lower values of BF and BV, which were associated with lack of vascularization due to tumor hypoxia, necrosis or fibrosis [26]. T_2 -weighted MRI offers better soft tissue contrast and resolution for tumour delineation; however, the delineated region could potentially include non-tumor features such as edema [27]. Fasting was not done prior to FDG-PET or subsequent glucoCEST and hyperpolarized $[1-^{13}C]$ pyruvate MRSI experiments, instead, blood glucose was monitored and confirmed to be within the

normoglycemic range prior to both imaging experiments. Although this could potentially decrease FDG uptake [28], there is evidence that glucose loading conditions may actually increase the conspicuity of brain tumors as normal brain uptake is decreased but gliomas continue to utilize FDG, even in hyperglycemic conditions [29]. Fasting for an extended period of time in small animals may also have more significant deleterious consequences than in humans, particularly if repeated for two days in a row for both imaging experiments [30]. Finally, in humans, FDG uptake has been shown to be approximately the same across brain regions in hypo- and normo-glycemic conditions [31]. Ultimately, we chose to monitor blood glucose instead of applying a fasting protocol prior to both imaging days in this fragile animal model. Blood glucose levels were comparable prior to the start of both imaging experiments and FDG uptake was conspicuous in the tumor relative to the surrounding brain tissue.

Although the imaging measurements were conducted within 24 hours, they were in the span of two days and on multiple scanners, as a result, the tumor perfusion and glycemic environment was not identical during the measurements. During the hyperpolarized [1-¹³C]pyruvate MRSI experiment, the subject will have received a relatively large injected volume that includes both the previous constant infusion of glucose and a bolus of [1-¹³C]pyruvate (approximately 6 ml total). Hypervolemia could lead to an elevated BV and PS [32,33], however BF should not be significantly affected [32]. Renal function such as the glomerular filtration rate will be elevated during glucose infusion [34] in order to compensate for the volume increase. The study plan was designed to follow the radiation safety protocol at different sites, as a result, the subjects had to be housed at our PET facility overnight to allow the radioactivity to decay before the subjects could be transferred to the MR facility. A hybrid PET/MR system could be used in the future to provide simultaneous measurement under the same tumor microenvironment. Meanwhile, there are a number of factors that could affect the CEST signal, including pH [35,36]. A lower pH environment would be induced by hyperglycemia [37] and in turn will lead to decreased CEST signal [6]. The glucose CEST measurements (AUC_{MTR}) during the constant infusion of glucose would have been underestimated due to pH reduction under hyperglycemic conditions. The

effect of hyperglycemia on the tumor pH environment induced by a constant infusion of glucose needs to be further investigated. One approach may be to use pH-sensitive CEST acquisitions such as acidoCEST [38,39] or amine and amide concentration-independent detection (AACID) [40] in conjunction with an infusion of glucose. The role that mammalian Target of Rapamycin (mTOR) plays in glucoCEST was not identified in this study. mTOR is upregulated in aggressive tumors and leads to elevated glucose uptake [41]. During the last half of the infusion protocol (during-infusion), tumor metabolism is likely to have plateaued as excess amounts of glucose are introduced into the system. In this scenario, glucoCEST would predominantly reflect perfusion effects. Xu et al. also concluded that glucoCEST signal originates mainly from the extravascular/extracellular space and blood vessels [41]. There are a couple of additional limitations using D-glucose as a contrast agent for CEST signal enhancement. The metabolism of glucose in cells will decrease glucoCEST signal as the metabolites from glycolysis cannot be detected with CEST [42]. In addition, insulin response to high blood glucose concentration will limit the amount of detectable free glucose in blood [42,43].

2.5 Conclusions

Dynamic glucose CEST measurements of tumor Δ CEST was significantly correlated with tumor perfusion measurements of BV and PS but not tumor glycolysis measurements of SUV and Lac:Pyr, suggesting that glucose CEST imaging using Δ CEST functions primarily as a perfusion tracer. Conversely, tumor glycolysis measurements of SUV and Lac:Pyr were significantly correlated with perfusion measurements of PS, reflecting increased tumor leakiness in tumors with higher glycolytic metabolism. Confounding these results is the fact that hyperglycemia induced by a constant infusion of glucose during dynamic CEST experiments may lead to a more acidic pH environment and give rise to underestimation of CEST measurements. Subsequently, in approximately half of the dynamic glucose CEST experiments, there was a drop in CEST signal post-glucose infusion. Although glucose CEST measurements may yield additional novel information

about tumor status, the complicated dependency of glucose CEST signal on a variety of factors would benefit from additional *in vivo* mechanistic studies.

2.6 Reference

1. Wen PY, Kesari S (2008) Malignant Gliomas in Adults. *N Engl J Med* 359: 492–507.
2. Jain RK, di Tomaso E, Duda DG, et al. (2007) Angiogenesis in Brain Tumors. *Nat Rev Neurosci* 8 (8): 610–22.
3. Sagiya K, Mashimo T, Togao O, et al. (2014) *In Vivo* Chemical Exchange Saturation Imaging Allows Early Detection of a Therapeutic Response in Glioblastoma. *Proc Natl Acad Sci USA* 111 (12): 4542-4547.
4. Chan KW, McMahon MT, Kato Y, et al. (2012) Natural D-glucose as a Biodegradable MRI Contrast Agent for Detecting Cancer. *Magn Reson Med* 68(6): 1764-1773.
5. Torrealdea F (2016) Investigation of Brain Tumor Metabolism Using Naturally Occurring Chemical Exchange Saturation Transfer Agents with Magnetic Resonance Imaging. PhD Thesis, University College London, UK.
6. Walker-Samuel S, Ramasawmy R, Torrealdea F, et al. (2013) *In Vivo* Imaging of Glucose Uptake and Metabolism in Tumors. *Nature Med* 19 (8): 1067-1072.
7. Jin T, Mehrens H, Hendrick KS and Kim SG (2014) Mapping Glucose Uptake with Chemical Exchange-sensitive Spin-lock Magnetic Resonance Imaging. *J of Cerebral & Metabolism* 34: 1402-1410.
8. Xu X, Yadav N, Knutsson L, et al. (2015) Dynamic Glucose-enhance (DGE) MRI: Translation to Human Scanning and First Results in Glioma Patients. *Tomography* 1 (2): 105-114.
9. Jin T, Lordanova B, Hitchens TK, et al. (2018) Chemical Exchange-Sensitive Spin-Lock (CESL) MRI of Glucose and Analogs in Brain Tumors. *Magn Reson Med* 80: 488-495.
10. Qi Q, Yeung TPC, Lee TY, Bauman G, et al. (2016) Evaluation of CT Perfusion Biomarkers of Tumor Hypoxia. *PLoS One* 11 (4): e0153569.
11. Yeung TPC, Wang Y, He W, et al. (2015) Survival Prediction in High-Grade Gliomas Using CT Perfusion Imaging. *J Neurooncol* 123: 93–123.
12. Yeung TPC, Bauman G, Yartsev S, et al. (2015) Dynamic Perfusion CT in Brain Tumors. *Eur J Radiol* 84 (12): 2386-2392.
13. Lee TY, Purdie TG and Stewart E (2003) CT Imaging of Angiogenesis. *QJ Nucl Med* 41: 171-187.

14. Tahari AK, Chien D, Azadi J, et al. (2014) Optimum Lean Body Formulation for Correction of Standardized Uptake Value in PET Imaging. *JNM* 55: 1481-1484.
15. Liu G, Song X, Chan KW, et al. (2013) Nuts and bolts of chemical exchange saturation transfer MRI. *NMR Biomed.* 26(7): 810-828.
16. Lim, H (2017) A Longitudinal study of tumor metabolism using hyperpolarized carbon-13 magnetic resonance spectroscopic imaging in a preclinical model of glioma. PhD Thesis, Western University, London.
17. Bonavia R, Inda M, Cavanee WK, et al. (2011) Heterogeneity maintenance in glioblastoma: a social network. *Cancer Res* 71: 4055–4060.
18. Mehrabian H, Desmon KL, Soliman H, et al. (2017) Differentiation between radiation necrosis and tumor progression using chemical exchange saturation transfer. *Clin Cancer Res* 2017; 23: 3667-3675.
19. Zhou J, Tryggstad E, Wen Z, et al. (2010) Differentiation between glioma and radiation necrosis using molecular magnetic resonance imaging of endogenous proteins and peptides. *Nat Med* 17(1): 130-134
20. Hogeboom WR, Hoekstra HJ, Mooyaart EI, et al. (1991) MRI and CT in the preoperative evaluation of soft-tissue tumors. *Arch Orthop Trauma Surg* 110: 162-164
21. Xu X, Chan K, Knutsson L, et al. (2015) Dynamic glucose enhanced (DGE) MRI for combined imaging of blood-brain barrier break down and increased blood volume in brain cancer. *Magn Reason Med* 74: 1556–1563.
22. Cao Y, Nagesh V, Hasmstra D, et al. (2006) The extent and severity of vascular leakage as evidence of tumor aggressiveness in high-grade gliomas. *Cancer Res* 66 (17): 8912-8917.
23. Hundershammer C, Braeuer M, Müller CA, et al. (2018) Simultaneous characterization of tumor cellularity and the Warburg effect with PET, MRI and hyperpolarized ¹³C-MRSI. *Theranostics* 8 (17): 4765-4780.
24. Twarock S, Reichert C, Peters U, et al. (2017) Hyperglycemia and aberrated insulin signaling stimulate tumor progression via induction of extracellular matrix component hyaluronan. *Int. J. Cancer* 141: 791-804.
25. Lund J, Ouwens DM, Wettergreen M, et al. (2019) Increased glycolysis and higher lactate production in hyperglycemic myotubes. *Cells* 8 (9): 1101. <https://doi.org/10.3390/cells8091101>.
26. Hsu T, Nguyen-Tran HH, and Trojanowska M. (2019) Active roles of dysfunctional vascular endothelium in fibrosis and cancer. *J Biomed Sci* 26: 86.

27. Blystad I, Warntjes JBM, Smedby Ö, et al. (2017) Quantitative MRI for analysis of peritumoural edema in malignant gliomas. *PLoS ONE*. 12(5): e0177135. <https://doi.org/10.1371/journal.pone.0177135>
28. Furger BJ, Czernin J, Hildebrandt, et al. (2006) Impact of animal handling on the results of ^{18}F -FDG PET study in mice. *J Nucl Med* 47 (6): 999-1006.
29. Kim, D, Ko HY, Lee S, et al. (2020) Glucose loading enhances the value of ^{18}F -FDG PET/CT for the characterization and delineation of cerebral gliomas. *Cancers* 12 (7). <https://doi.org/10.3390/cancers12071977>
30. Jensen, TL, Kiersgaard MK, Sørensen DB, et al. (2013) Fasting of mice: a review. *Lab Anim* 47 (4): 225–40.
31. Sarikaya I, Albatineh AN, and Sarikayaa A. (2020) Effect of various blood glucose levels on regional FDG uptake in the brain. *Asia Ocean J Nucl Med Biol* 8 (1): 46–53.
32. Todd MM, Weeks JB, Warner DS (1993) The influence of intravascular volume expansion on cerebral blood flow and blood volume in normal rats. *Anesthesiology* 78: 945-953.
33. Cole DJ, Drummond JC, Mastumura JS, et al. (1990) Hypervolemic-hemodilution and hypertensive during temporary middle cerebral artery occlusion in rats: the effect on blood-brain barrier permeability. *Can. J. Neurol. Sci.* 17: 372-377.
34. Christiansen JS, Frandsen M, and Parving HH. (1981) Effect of intravenous glucose infusion on renal function in normal man and insulin-dependent diabetics. *Diabetologia* 21: 368-373.
35. van Zijl PCM and Yadav NN (2011) Chemical exchange saturation transfer (CEST): What is in a name and what isn't? *Magn. Reson. Med* 65 (4): 927-948.
36. Sun PZ and Sorensen AG (2008) Imaging pH using the chemical exchange saturation transfer (CEST) MRI: Correction of concomitant RF irradiation effects to quantify CEST MRI for chemical exchange rate and pH. *Magn. Reson. Med* 60 (2): 390-397.
37. Roszinski S, Wiedemann G, Jiang SZ, et al. (1991) Effects of hyperthermia and/or hyperglycemia on pH and pO_2 in well oxygenated xenotransplanted human sarcoma. *Inl. J. Radiat Oncol Biol Phys* 20 (6): 1273-1280.
38. Chen LQ, Howison CM, Jeffery JJ, et al. (2014) Evaluation of extracellular pH within *in vivo* tumors using acidoCEST MRI. *Magn. Reson. Med* 72 (5): 1408-1417.
39. Longo DL, Bartoli A, Consolino L, et al. (2016) In vivo imaging of tumor metabolism and acidosis by combining PET and MRI-CEST pH imaging. *Can Res* 76(22): 6463-6470.

40. McVicar N, Li A, Gonçalves DF, et al. (2014) Quantitative tissue pH measurement during cerebral ischemia using amine and amide concentration-independent detection (AACID) with MRI. *J. Cereb Blood Flow Metab* 34 (4): 690-698.
41. Xu X, Xu J, Knutsson L, et al. (2019) The effect of the mTOR inhibitor rapamycin on glucoCEST signal in a preclinical model of glioblastoma. *Magn Reson Med* 81(6): 3798-3807.
42. Nasrallah FA, Pages G, Kuchel PW, et al. (2013) Imaging brain deoxyglucose uptake and metabolism by glucoCEST MRI. *J. Cereb Blood Flow Metab* 33: 1270-1278.
43. Sehgal AA, Li Y, Lal B, et al. (2018) CEST MRI of 3-O-methyl-D-glucose and accumulation in brain tumors. *Magn. Reson. Med.* 81: 1993-2000.

Chapter 3

Glucose Infusion Induced Change in Intracellular pH and Its Relationship with Tumor Glycolysis in a C6 Rat Model of Glioblastoma

Qi Qi, Matthew S. Fox, Heeseung Lim, Rebecca Sullivan, Alex Li, Miranda Bellyou, Lise Desjardins, Andrew McClennan, Robert Bartha, Lisa Hoffman, Timothy J. Scholl, Ting-Yim Lee, Jonathan D. Thiessen

Submitted to *Molecular Imaging and Biology* in November 2021.

Abstract

In the previous chapter, we explored the relationship between tumor perfusion and its glycolytic metabolism. In this chapter, we explore the relationship between tumor glycolysis and its intracellular pH (pH_i) environment. The reliance on glycolytic metabolism is a hallmark of tumor metabolism. Excess acid and protons are produced, leading to an acidic tumor environment. Therefore, in this chapter, we explored the relationship between the tumor glycolytic metabolism and tissue pH by comparing ^{18}F -fluorodeoxyglucose positron emission tomography (FDG-PET) and hyperpolarized $[1\text{-}^{13}\text{C}]\text{pyruvate}$ MR spectroscopy imaging (MRSI) to chemical exchange saturation transfer (CEST) MRI measurements of tumor pH_i . We found that pH_i measurements using amine and amide concentration independent detection (AACID) CEST MRI detected the changes in pH_i induced by glucose infusion. Significant correlations between tumor glycolytic measurement of Lac:Pyru and tumoral and peritumoral pH_i and ΔpH_i reveal the intrinsic relationship between tumor glycolytic metabolism and the tumor pH environment as well as the peritumor pH environment.

3.1 Introduction

Tumor pH and metabolism are intrinsically related. Changes in the tumor pH environment as a result of metabolism could provide crucial information on its aggressiveness and progression [1–4]. In general, the tumor extracellular pH (pH_e) environment is more acidic than intracellular pH (pH_i) as a result of the overreliance on aerobic glycolysis, through which excess lactic acid and H^+ are produced and transported to the extracellular space to maintain a more alkaline pH_i , which avoids apoptosis [1,2,5,6]. pH_e can be measured *in vivo* using techniques such as pH probes, chemical exchange saturation transfer (CEST) in conjunction with exogenous contrast agents, and magnetic resonance spectroscopy imaging (MRSI) using hyperpolarized bicarbonate [3,5–7]. However, the *in vivo* information on pH_i is often missing as it is challenging to obtain information from the intracellular space. Importantly, an alteration in tumor pH_i could provide crucial information about treatment response [6,10]. Previously, an infusion of glucose was found to decrease extracellular pH in human tumor xenografts [8]. In fact, most tumors rely on aerobic glycolysis for energy production (also known as “the Warburg effect”), resulting in increased production of H^+ and lactate acid that are extruded to the extracellular space [4]. Tumoral and peritumoral regions are intrinsically related, with tumor metabolism also able to alter the peritumoral pH microenvironment. pH in the peritumoral region could potentially indicate the level of tumor activity or aggression [3]. Lower pH_i in the peritumoral region could be due to a high concentration of hydrogen ions produced by highly active tumor cells.

A CEST MRI method based on the distinct CEST responses of the endogenous amide and amine proton that are available in tumor intracellular space enables the measurement of *in vivo* pH_i [11]. Amide and amine concentration independent detection (AACID) was developed exploiting the change in exchange rate of amide and amine protons due to change in pH_i [11]. The ratio of amide-to-amine CEST effect can be calculated and then related to pH_i [10,11], where higher AACID values are associated with lower pH_i .

Tumor glycolytic metabolism can be evaluated with positron emission tomography (PET) and ^{18}F -fluorodeoxyglucose (FDG), a glucose analogue that is phosphorylated to FDG-6-

phosphate (FDG6P) after the first step of glycolysis but doesn't go through subsequent steps. As a result, FDG6P becomes trapped inside cells. Anaerobic glycolysis can also be measured with magnetic resonance spectroscopy imaging (MRSI) by monitoring the conversion of lactose to pyruvate during anaerobic glycolysis to lactate after an injection of hyperpolarized [1-¹³C]pyruvate [12].

The purpose of this study was to explore the relationship between tumoral, peritumoral pH_i and the change in pH_i after a glucose infusion using AACID CEST MRI, and tumoral glycolytic activity measured using FDG-PET and hyperpolarized [1-¹³C]pyruvate MRSI. Intracellular pH measurements were made following perfusion of glucose and related to previously published measures of glycolysis [13]. We hypothesized that tumoral and peritumoral pH_i are inversely proportional to tumor glycolysis measurements; and the change in tumoral and peritumoral pH_i induced by glucose infusion are directly proportional to tumor glycolysis measurements.

3.2 Methods

3.2.1 Experiment design

Detailed experimental protocols and procedures can be found in Chapter 2 [13]. All procedures were performed in compliance with the Canadian Council for Animal Care and approved by the Western University Animal Care Committee. In short, C6 glioma tumor cells were implanted on Day 0 followed by a CT perfusion check on Day 7 to confirm tumor growth (tumor longest axis ≥ 4 mm) [13,14]. After confirming the longest axis of tumor had reached 4 mm, the FDG-PET experiment was performed between Day 11-13 after C6 cell implantation. MRI experiments (CEST followed by hyperpolarized [1-¹³C]pyruvate MRSI) were performed on the next day immediately prior to euthanasia with all imaging experiments taking place within a span of 24 hours for each animal.

3.2.2 C6 glioma model

A detailed description of the C6 glioma model can be found in previous publications [13,14].

Male Wistar rats (Charles River, Canada, age 8 to 10 weeks at surgery) weighing on average 401 ± 42 g ($N = 11$) were used in this study. The animals were induced with 5% isoflurane and were maintained at 2% during the surgery. A burr hole was drilled at a point 1 mm anterior and 3 mm to the right of the bregma after an incision on the skull to expose the bregma. 1 million C6 glioma cells (CCL-107, American Type Culture Collection, Manassas, VA) were cultured [13,15] and injected at the location of the burr hole at a depth of 3-4 mm from the skull surface with a Hamilton syringe. The burr hole was filled with bone wax and the incision was sutured. Animals were recovered and returned to animal facility for housing after the surgeries.

3.2.3 FDG-PET imaging

The detailed PET procedure can be found in Chapter 2 [13]. In short, all PET acquisitions were performed using a small animal PET system (Inveon DPET, Siemens Healthineers, Knoxville, TN, USA). The blood glucose of each subject was measured and reported in previous work [13] by taking blood from a lateral tail vein prior to an injection. Each subject was injected with a bolus of ^{18}F -FDG (31.5 ± 3.1 MBq) intravenously 30 s after the start of the 75 min dynamic PET acquisition. The PET data was reconstructed using a CT-based attenuation correction map and an iterative, 3D ordered subset expectation maximization with 2 iterations and 18 subsets.

Standardized uptake values (SUV) were calculated using the last 15 minutes of the PET images as a measurement of glycolysis [13,16].

3.2.4 Dynamic CEST imaging

A detailed description of the CEST procedure can also be found in a previous publication [13]. The dynamic CEST MRI was acquired on a 9.4-T small animal MRI (Agilent, Palo Alto, CA, USA) on the morning after the PET acquisition (12 – 14 days after the surgery). MR images were acquired on a 9.4 T small animal MRI scanner (Agilent, Palo Alto, CA, USA) equipped with a 15-cm gradient coil set of 450 mT/m strength, Bruker Avance MRI III console with software package of Paravision-6 (Bruker BioSpin Corp, Billerica, MA). Standard anatomical T₂-weighted images were used for tumor detection. The axial T₂-weighted images were acquired using a 2-dimensional TurboRARE pulse sequence with parameters: TR/TE = 5000/40 ms, FOV = 38.4 × 38.4 mm², matrix size = 192 × 192, 31 slices with slice thickness = 1 mm. Upon initial tumor detection, a 2 mm-slice from the T₂-weighted images with maximum tumor coverage was selected for CEST imaging. CEST imaging was acquired using a 2-dimensional RARE pulse sequence (TR/TE = 10000/25 ms, FOV = 38.4 × 38.4 mm², matrix size = 96 × 96, slice thickness = 2 mm) preceded by a continuous RF pulse with amplitude 1.5-μT and duration 4 s. The CEST images were acquired at different saturation frequencies (-5.0 to 5.0 ppm with 0.2 ppm-increment), -1000 and 1000 ppm images were acquired as reference, total 53 images). Three consecutive spectra were obtained with 30 min per CEST acquisition. A baseline CEST spectrum was acquired prior to an infusion. A bolus of 20% by weight of D-glucose and saline solution (0.3 g/kg) was injected after the baseline CEST spectrum, followed by a 60-minute constant infusion of the same 20% D-glucose solution (1.5 g/kg/hour). The acquisition of the second and third CEST spectra were associated with the first and second half of glucose constant infusion with 30-minute duration each, respectively. The third CEST spectrum was denoted as “During infusion” and used to compare with the baseline CEST spectrum to examine the effect of glucose infusion on pH_i using AACID. The CEST signal from glucose may be not relevant to the AACID evaluation as only amine and amide resonant frequencies were used for analysis.

3.2.5 Hyperpolarized [1-¹³C]pyruvate

Detailed procedures for hyperpolarized [1-¹³C]pyruvate MRSI can be found in previous publications [12,13].

Briefly, the hyperpolarized [1-¹³C]pyruvate MRSI experiment took place immediately after the CEST experiment on a GE Discovery MR750 3.0 T MRI (General Electric Healthcare, Waukesha WI, USA). An FSE sequence was used to locate and acquire an axial T₂-weighted MRI of the same slice used for the CEST acquisition (80 × 80 mm FOV, 0.3-mm in-plane resolution, 3-mm slice thickness, TR = 4000 ms, TE = 85 ms, 16 echo trains, number of averages = 9). A volume of 3 mL hyperpolarized [1-¹³C]pyruvate solution was injected through a rat lateral tail vein by a single bolus in 12 s. Axial ¹³C spectra was acquired using a 2D free induction decay chemical shift imaging (FID-CSI) pulse sequence (FOV = 60 × 60 mm, slice thickness approximately equal to the tumor extent, 12 × 12 spectral imaging matrix, TR = 80 ms, bandwidth = 5 kHz, 2048 pts, flip angle = 10°) 13 s after injection to complete the circulation and metabolism of hyperpolarized [1-¹³C]pyruvate. Each FID-CSI containing 144 spectra was acquired within a total scan time of 12 s. Maps of the ratio of lactate to pyruvate (Lac:Pyr) were derived as a measurement of anaerobic glycolytic metabolism using a customized MATLAB script [12,13]. The animal was euthanized immediately at the end of the experiment.

3.2.6 Phantom preparation

Phantoms were made following the recipe from McVicar et al. [11] to imitate physiological protein and glucose concentration in rodent and human brain. Bovine serum albumin powder (BSA, Sigma-Aldrich, St. Louise, Missouri, US) and glucose powder (D-(+)-glucose, Sigma-Aldrich, St. Louise, Missouri, US) were prepared in pH buffer solutions to achieve 10% BSA and the required glucose concentrations (2.5, 4.5 and 6 mM). A series of pH buffers were made by adding HCl and NaOH to 1x phosphate-buffered saline (PBS) solution to obtain physiological pH levels of 6.2, 6.4, 6.6, 6.8, 7.0, 7.2 and 7.4. The pH values were measured by using a benchtop pH meter (Accumet Basics AB15 pH meter, Fisher Scientific, Waltham, Massachusetts, US). Three phantoms at glucose concentration of 2.5, 4.5 and 6 mM were made to mimic extracellular tissue glucose concentrations

during normo- to hyperglycemic conditions in rat brain [17]. Each phantom contains 7 NMR tubes (3 mm diameter, Sigma-Aldrich, St. Louise, Missouri, US) held by a custom 3D printed holder. The NMR tubes contain mixtures at pH of 6.2, 6.4, 6.6, 6.8, 7.0, 7.2 and 7.4. Phantoms were scanned using the same imaging protocol as the *in vivo* CEST experiment as described above.

3.2.7 Simulation

A 7-pool model was used to simulate AACID CEST signal (based on code available at cest.org), with the analytical solution derived from Bloch-McConnell equations as described by Zaiss et al. [18,19]. 4 pools were associated with glucose at resonant frequencies of 0.66, 1.29, 2.18 and 2.88 ppm (Pool B, D, E, F respectively), 1 pool was associated with amine at 2.75 ppm (Pool G), 1 pool was for amide at 3.5 ppm (Pool H), and the water pool was set at 0 ppm (Pool A). The macromolecule effect and nuclear overhauser effect (NOE) were neglected from the simulation. The exchange rates at different pH's for glucose at 4 resonant frequencies were defined using **Equation 3.1** according to Zaiss et al [18,19]:

$$k_{XA} = k_{x1} \cdot 10^{\text{pH}-7} + k_{x0} \quad [3.1]$$

Where k_{BA} , k_{DA} , k_{EA} and k_{FA} ($x = B, D, E$ and F) are the proton exchange rates for the 4 corresponding exchanging protons on D-glucose, and the exchange rates for amine and

$$k_{\text{amine}} = 10^{\text{pH}-4.2} \quad [3.2]$$

amide at different pHs were defined as **Equation 3.2** and **3.3** based on McVicar et al [11].

$$k_{\text{amide}} = 5.75 \times 10^{\text{pH}-6.4} \quad [3.3]$$

Relevant simulation parameters are listed in **Table 3.1**.

Table 3.1: Parameters used for the 7-pool BM simulation.

Parameter	Value
T_1	2.002 s
T_2	0.2 s
B_0	9.4 T
B_1	1.5 μ T
Glucose concentration	2.5, 4.5 and 6 mM
k_{B1}	1467 Hz
k_{B0}	617 Hz
k_{D1}	3580 Hz
k_{D0}	800 Hz
k_{E1}	2804 Hz
k_{E0}	669 Hz
k_{F1}	8543 Hz
k_{F0}	675 Hz

3.2.8 CEST imaging analysis

Custom scripts were written using MATLAB 2018b (MathWorks, Natick, Massachusetts USA) for all CEST analysis. A mask of the brain was delineated using the T_2 -weighted MR images and applied to the CEST images. The Z-spectra were fitted with method described in a previous publication [13], briefly, the data from each voxel was smoothed with a smoothing spline fit of a fitting parameter of 0.998. The frequency associated with the minima of Z-spectra were shifted to 0 ppm for B_0 correction. Magnetization transfer ratio asymmetry (MTR_{asym}) spectra were calculated as shown in **Equation 3.4**.

$$\mathbf{MTR}_{\text{asym}} = \frac{S(-\Delta\omega) - S(\Delta\omega)}{S_0} \quad [3.4]$$

Using the $\mathbf{MTR}_{\text{asym}}$ spectra, a Lorentzian line was fitted at the visible resonance frequencies of glucose, amine and amide. The amplitude and fullwidth half maximum (FWHM) were obtained from these Lorentzian curves, however, the effect of NOE was not identified in this estimation.

AACID maps were generated using a custom MATLAB script, with AACID values calculated based on **Equation 3.5** using method developed by McVicar et al [11].

$$\mathbf{AACID} = \frac{\mathbf{Mz}(3.50 \text{ ppm}) \times (\mathbf{Mz}(5 \text{ ppm}) - \mathbf{Mz}(2.75 \text{ ppm}))}{\mathbf{Mz}(2.75 \text{ ppm}) \times (\mathbf{Mz}(5 \text{ ppm}) - \mathbf{Mz}(3.50 \text{ ppm}))} \quad [3.5]$$

3.2.9 Estimation of pH_i using AACID

The CEST data from the phantom was analyzed using the same method described above, the AACID values were calculated, and the relationships between AACID and pH were evaluated and plotted at the three concentrations of 2.5, 4.5 and 6 mM that is comparable to brain glucose concentration during normoglycemia to hyperglycemia *in vivo* [17]. A linear relationship was fitted, and the goodness-of-fit (R^2) was reported between pH and

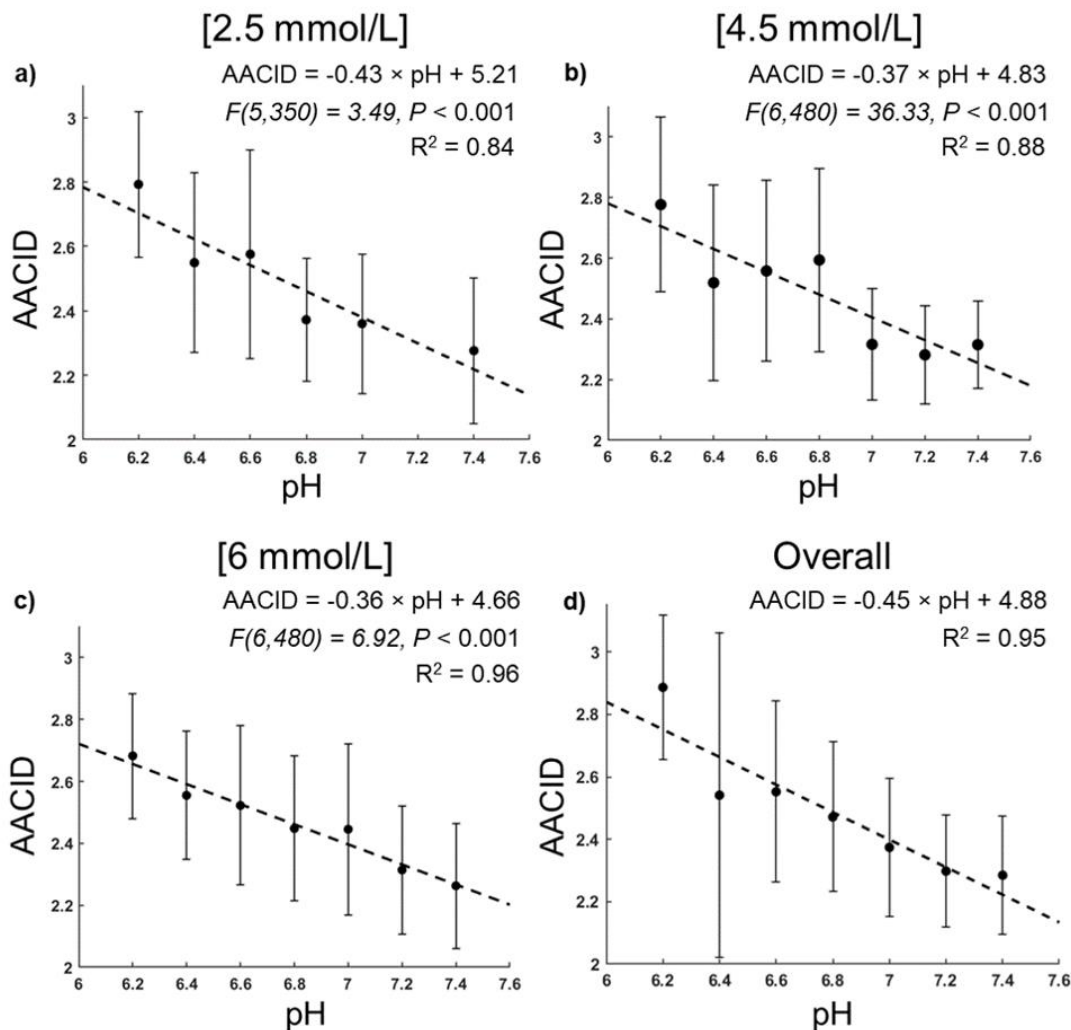


Figure 3.1: The relationship between pH and AACID value from phantom measurements are plotted at glucose concentrations of 2.5 (a), 4.5 (b), 6 mmol/L (c) and combined (d). The lines of best fit are represented by the dotted line; the fitting equations, the one-way ANOVA result and the goodness-of-fit are shown at the top right corner of each plot. The error bars denote the standard deviation of AACID values from all pixels for individual tube.

AACID values at these glucose concentrations as shown in **Figure 3.1**. Differences between the linear correlation of pH and AACID were compared at the different glucose concentrations to determine whether glucose concentration affected the AACID measurements. The phantom calibration data were then used to estimate pH_i from the *in vivo* AACID values. The NOE effect was minimal to AACID calculation [11] in both

phantom and *in vivo* experiments and neglected as AACID is independent of NOE as shown in **Equation 3.5**.

The change in pH_i (ΔpH_i) and the baseline intracellular pH gradient (pHG_i) are defined by **Equations 3.6** and **3.7** respectively:

$$\Delta\text{pH}_i = \text{pH}_i (\text{During}) - \text{pH}_i (\text{Pre}) \quad [3.6]$$

$$\text{pHG}_i = \text{pH}_i (\text{Tumor}) - \text{pH}_i (\text{Peritumor}) \quad [3.7]$$

3.2.10 ROI selection and image registration

A detailed description of ROI analysis and image registration can be found in a previous publication [13]. T_2 -weighted MRI was used as guidance for manual delineation of tumor, peritumor (3 mm away from the tumor boundary [15,20]) and contralateral brain regions. All voxels that contained tumor on the T_2 -weighted MRI were included in the tumor ROIs. The T_2 -weighted MRI was also used as a reference for manual rigid co-registration of CEST, FDG-PET and hyperpolarized $[1-^{13}\text{C}]$ pyruvate images using 3D Slicer (www.slicer.org). ROI delineations using the T_2 -weighted image from the 9.4 T MRI were applied to all of the co-registered parameter maps (CEST, MRSI, and FDG-PET). The average tumoral, peritumoral and contralateral brain pH_i and ΔpH_i from CEST; tumor SUV from FDG-PET; and tumor Lac:Pyr ratios from hyperpolarized $[1-^{13}\text{C}]$ pyruvate MRSI were extracted.

3.2.11 Statistical analysis

One-way ANOVA tests were performed to investigate the simple main effect of pH on AACID and the simple main effect of glucose concentration on AACID values. A two-tailed paired-sample T-test was performed to investigate the differences between tumor, peritumor and contralateral brain pH_i measurements. The Pearson correlations between averaged tumor Lac:Pyr, SUV, and pH_i for tumoral and peritumoral tissues were evaluated using IBM SPSS version 22. A P value ≤ 0.05 was considered statistically significant.

3.3 Results:

3.3.1 AACID vs. pH from simulation

From the three glucose concentrations ranging from normoglycemia to hyperglycemia, inversely proportional relationships between pH and AACID were found among all three as shown in **Figure 3.2**, with a higher AACID value associated with a lower pH value. R^2 of the linear fitting from simulation at glucose concentration of 2.5 (**a**), 4.5 (**b**) and 6 mM (**c**) are 0.99.

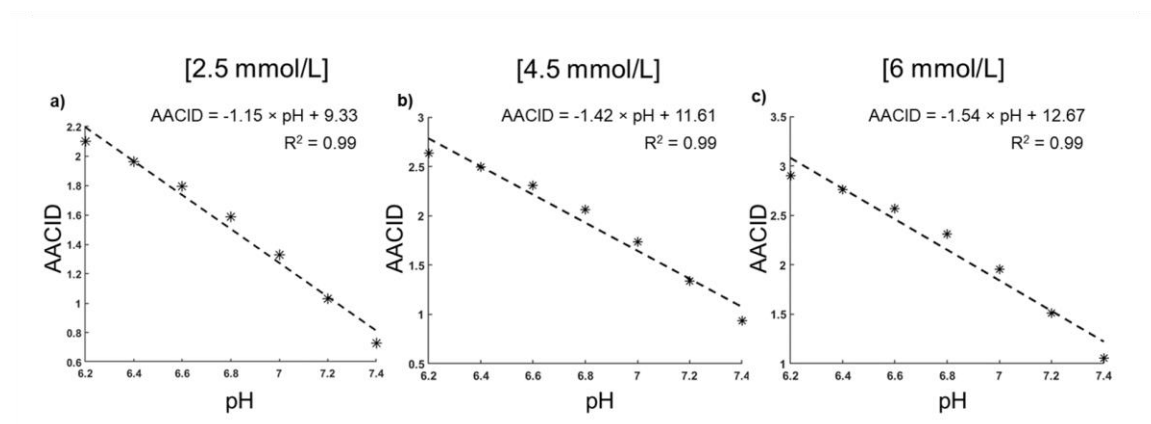


Figure 3.2: The relationship between pH and AACID value from simulation using the 7-pool exchange model are plotted at glucose concentrations of 2.5 (**a**), 4.5 (**b**) and 6 mmol/L (**c**). The lines of best fit are represented by the dotted line, and the fitting equations and the goodness-of-fit are shown at the top right corner of each plot.

3.3.2 CEST signal at relevant metabolite resonance frequencies

An illustrative example of the phantom MTR_{asym} maps at resonance frequencies of glucose, amide and amine are shown in **Figure 3.3**.

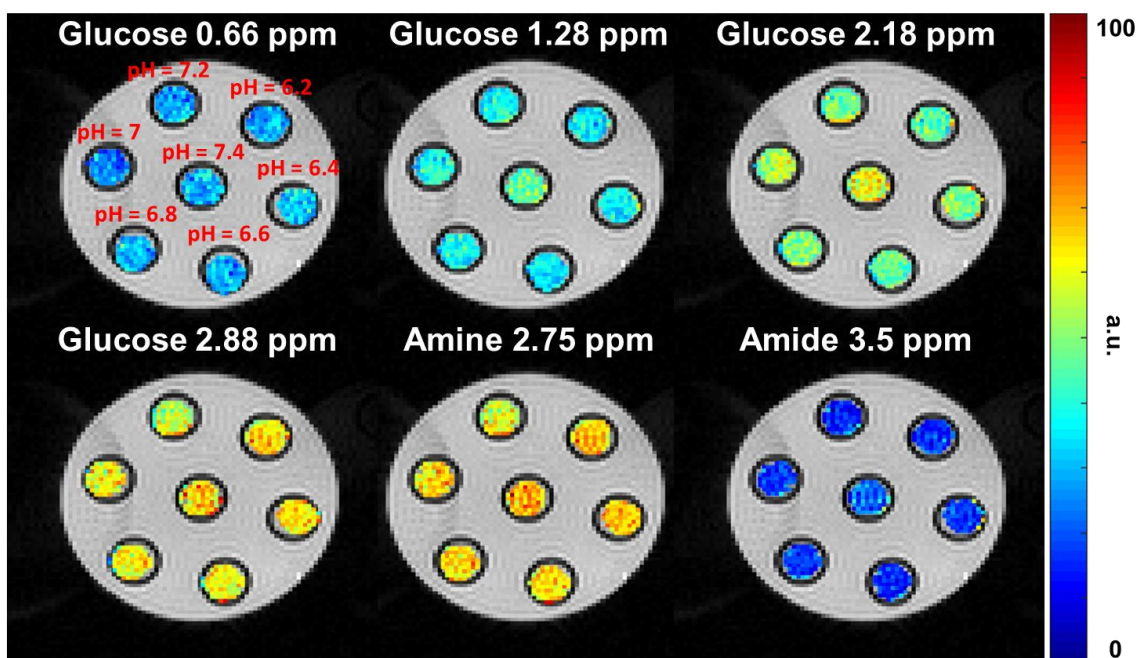


Figure 3.3: MTR_{asym} maps of phantom (6 mM) at the four main resonant frequencies of glucose as well as the amine and amide resonant frequencies.

3.3.3 AACID value vs. pH from phantom

From normoglycemia to hyperglycemia using the same concentration as the simulation, an inversely proportional relationship between pH and average AACID values are shown in **Figure 3.1** demonstrating a higher AACID value is associated with a lower pH under all three glucose concentrations. An inversely proportional relationship between AACID values and pH was found among all three glucose concentrations as shown in **Figure 3.1**, the slopes, the y-intercepts, and the R^2 at each concentration also are displayed. A one-way ANOVA test indicated a simple main effect of pH on AACID value ($P < 0.05$). Glucose

concentration did not indicate a simple main effect on AACID values ($P > 0.05$) from the one-way ANOVA test. As a result, the slope and intercept from the overall fitting were used to obtain an overall estimation of pH_i independent of glucose concentration (**Figure 3.1d**).

3.3.4 Comparison among phantom and *in vivo* AACID values

The *in vivo* AACID values displayed a similar range as AACID values acquired from phantom measurements as shown in **Table 3.2**. The *in vivo* AACID values were calibrated using the AACID values acquired from the phantom scan, and the resulting average pH_i using the phantom calibration.

3.3.5 pH_i change during glucose infusion

The average pH_i before and during glucose infusion in tumoral, peritumoral and contralateral tissue regions are shown in **Figure 3.4**. Co-registered pH_i maps, SUV and Lac:Pyr images are shown in **Figure 3.5**.

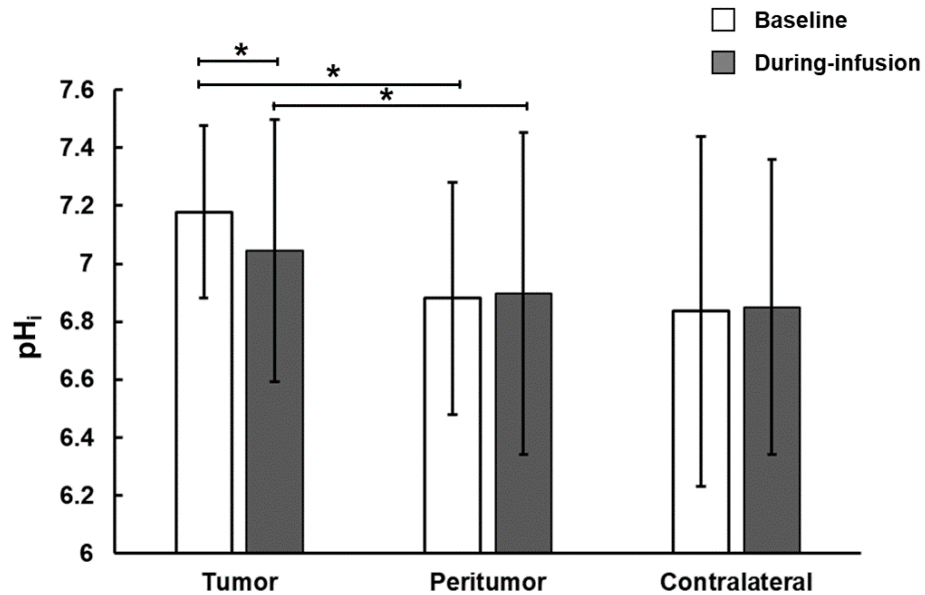


Figure 3.4: The average pH_i before and during glucose infusion at tumoral, peritumoral and contralateral brain regions. The asterisk denotes the significant difference ($P < 0.05$), and the error bars denotes the standard deviation.

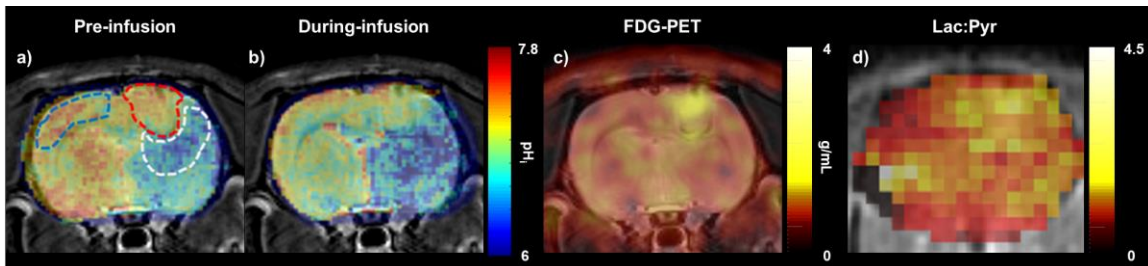


Figure 3.5: An illustrative example of registered pH_i maps (pre- and during-infusion), FDG-PET and Lac:Pyr maps overlaid on T₂-weighted MRI. Tumor, peritumor and contralateral brain regions are delineated by red-, beige- and blue-dotted lines, respectively.

Table 3.2: Range of AACID values from *in vivo* and phantom measurements.

	AACID range
in vivo pre-infusion	0 - 2.89
in vivo post-infusion	0 - 3.52
Phantom [2.5 mmol/L]	0 - 3.40
Phantom [4.5 mmol/L]	0 - 3.05
Phantom [6 mmol/L]	0 - 2.91

After comparing the pH_i pre- and during infusion using a two-tailed paired-sample T-test, a significant difference was found in the tumoral region ($P < 0.01$), whereas no significant change was found in the peritumoral ($P = 0.93$) or the contralateral brain region ($P = 0.30$). The tumoral pH_i are significantly higher than peritumoral pH_i before ($P < 0.01$) and during ($P = 0.04$) glucose infusion. However, the contralateral brain pH_i is not significantly different from either tumoral (pre-infusion: $P = 0.14$; during-infusion: $P = 0.89$) or peritumoral (pre-infusion: $P = 0.85$; during-infusion: $P = 0.43$) regions.

3.3.6 Tumor glycolysis measurements vs. *in vivo* pH_i

Significant correlations between tumor Lac:Pyr and baseline tumoral pH_i ($\rho = -0.58$, $P = 0.04$) and peritumoral pH_i ($\rho = -0.66$, $P = 0.03$) are shown in **Figure 3.6 a)** and **b)**. Higher tumor Lac:Pyr is associated with lower tumoral and peri-tumoral pH_i. Significant correlation was also found between tumor Lac:Pyr and pHG_i from tumor-peritumor regions ($\rho = 0.57$, $P = 0.05$, **Figure 3.7**). Higher tumor Lac:Pyr leads to higher pH_i gradient (tumor pH_i > peritumor pH_i).

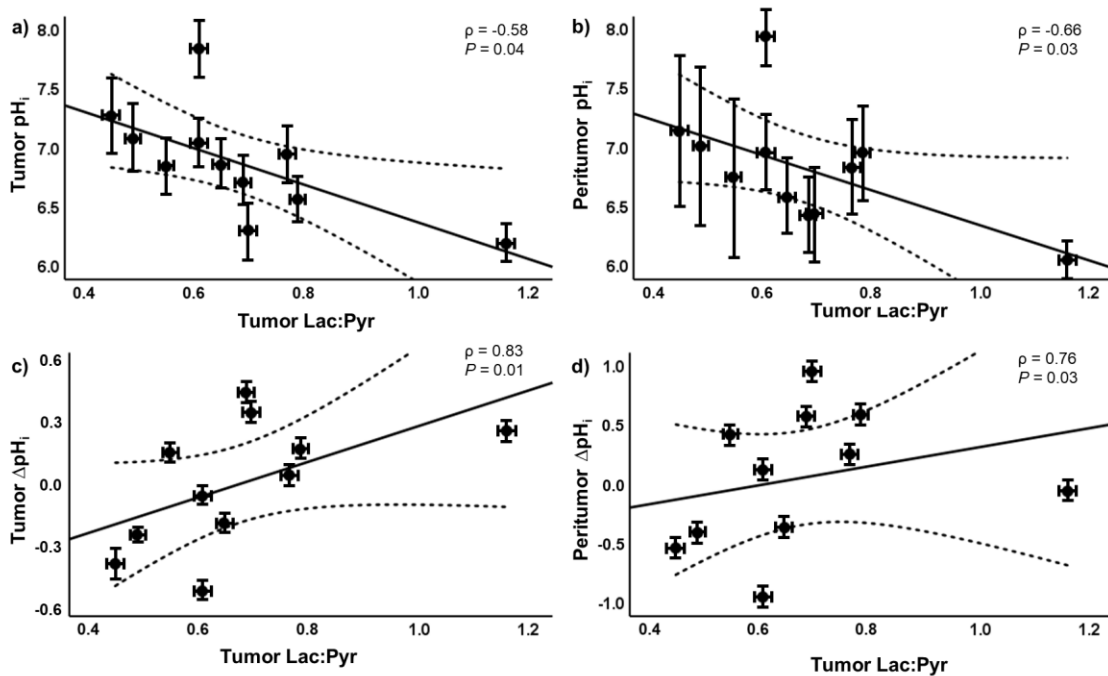


Figure 3.6: The relationship between tumor Lac:Pyr and tumor baseline pH_i (a) peritumor baseline pH_i (b), tumoral Δ pH_i (c); and peritumoral Δ pH_i (d). Dotted lines indicate the 95% confidence interval, and the error bar denotes the standard deviation.

Significant correlations between tumoral Lac:Pyr and tumoral, peritumoral Δ pH_i ($\rho = 0.83$, $P = 0.01$; $\rho = 0.76$, $P = 0.03$ respectively) were also found as shown in **Figure 3.6 c)** and **d)**. Higher tumor Lac:Pyr leads to a greater increase in pH_i in tumoral and peritumoral regions during glucose infusion. However, no significant correlation was found between

tumoral or peritumoral ΔpH_i with tumor SUV ($\rho = -0.45$, $P = 0.17$; $\rho = -0.6$, $P = 0.051$ respectively) as shown in **Table 3.3**.

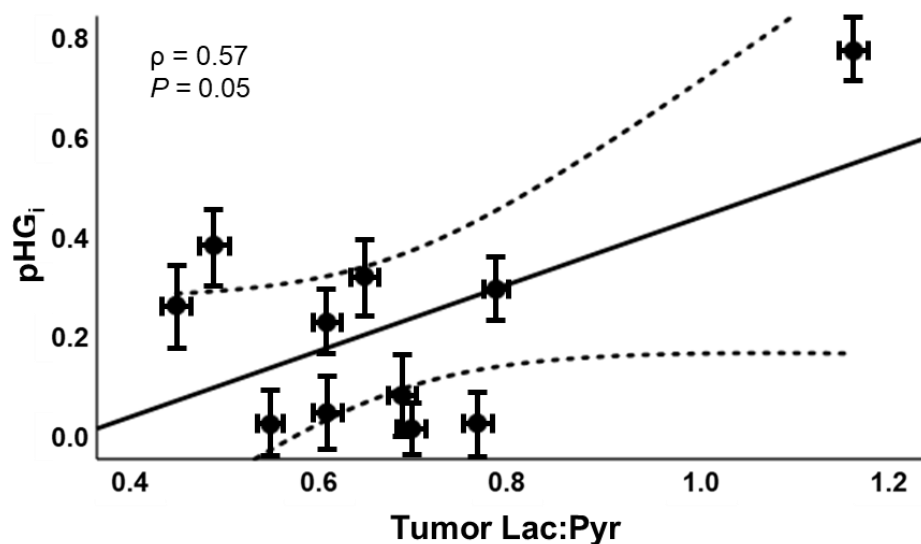


Figure 3.7: The relationship between tumor Lac:Pyruvate vs. pHG_i pre-infusion. Dotted lines indicate the 95% confidence interval, the error bar = standard deviation

Table 3.3: Pearson's correlation among tumor glycolysis measurements (SUV and Lac:Pyruvate) and tumor and peritumor baseline pH_i , pHG_i and ΔpH_i induced by glucose infusion. The asterisk indicates a statistical significance of $P < 0.05$.

$N = 11$	pH_{i_t}	pH_{i_p}	pHG_i	ΔpH_{i_t}	ΔpH_{i_p}
SUV	-0.33	-0.27	0.16	-0.45	-0.51
Lac:Pyruvate	-0.58*	-0.66*	0.57*	0.83*	0.76*

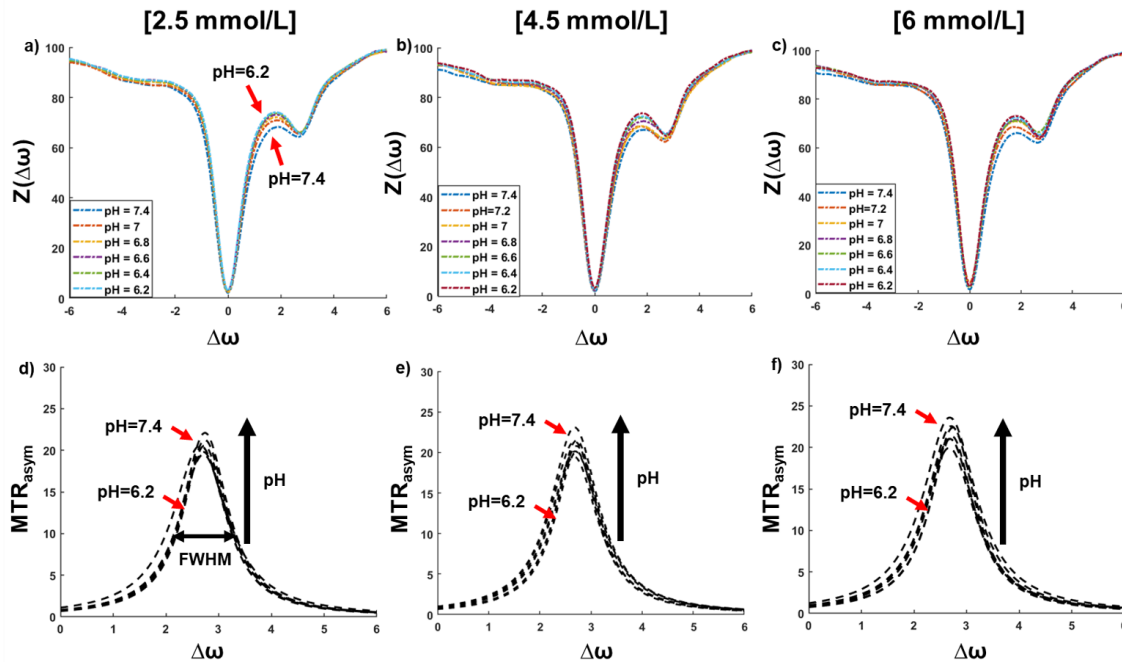


Figure 3.8: The z-spectra from the phantom experiment and the Lorentzian fitting of the glucose peak at 2.18 ppm. The FWHM and amplitude increase as the pH increases from 6.2 to 7.4.

3.4 Discussion:

Both phantom and simulation results indicated the inversely proportional relationship between pH and AACID values remains under normoglycemic to hyperglycemic conditions (as shown in **Figure 3.2** and **3.3**), where higher AACID values are associated with lower pH values. These results agreed with previous publications [10,11]. The results from both the phantom experiment and simulation confirmed that the relative change of AACID values before and after the glucose infusion captured the pH_i change *in vivo*. The one-way ANOVA test from the phantom measurements indicated a simple main effect of pH on AACID values but the glucose concentration did not have a simple main effect on the AACID values. This potentially indicates that AACID values are independent of metabolite concentration, even in the presence of a metabolite (glucose) with a resonant frequency close to amine. Although no simple main effect was found when evaluating

AACID values measured with different glucose concentrations, the slopes and y-intercepts are different when simulating three different concentrations of glucose. Because of the lack of significant effect of glucose concentration on AACID values, we combined the data from all phantom experiments to create an overall estimate of the slope and intercept to relate AACID to pH_i . It is worth noting that the slope and y-intercept from the current fitting are distinct from the reported slope (-0.64) and y-intercept (6.5) without the presence of glucose from the original AACID publication that used a FSE sequence of the same B_1 and RF duration [11]. Overall, although the glucose concentration does not have a simple main effect on AACID, a calibration experiment with customized phantom mimicking the experimental microenvironment would ensure the accuracy of pH_i measurements using AACID CEST MRI.

The Lorentzian fitted lines on the MTR_{asym} spectra from the phantoms, showed an increase in the FWHM for glucose peaks was observed as pH increased (**Figure 3.8**). In a previous study, the direct proportional relationship between FWHM of MTR_{asym} and the k_{ex} of the corresponding metabolite was demonstrated [21]. The increasing FWHM as pH increased from 6.2 to 7.4 confirmed the k_{ex} approximation using **Equation 3.1** for simulation.

As reported from a previous publication, the baseline blood glucose of this set of rats was 7.3 mmol/L and slowly increased to > 20 mmol/L when using the same infusion protocol on the benchtop [13]. This corresponds to brain glucose concentrations of approximately 1.8 mmol/L at baseline and > 5 mmol/L during infusion according to the estimation given by Silver et al. [17], these glucose concentrations are comparable to the values used in the simulation and the phantom study. The pre-infusion tumor pH_i derived using the phantom calibration is 7.17 ± 0.29 , which is close to a previous study using the same tumor type and similar time post-surgery ($\text{pH}_i \approx 7.3$) [6]. AACID CEST was able to capture the changes in tumoral pH_i induced by glucose infusion, with pH_i in the tumor region significantly lower during-infusion (7.03 ± 0.45) than pre-infusion. However, no significant changes of pH_i in peritumoral or contralateral brain regions were found. Decreased pH_i after a glucose infusion can be attributed to the Warburg effect, with elevated glycolytic activity, especially

under hyperglycemic conditions, resulting in the production of excess H^+ and lactate [2–4]. Peritumoral and contralateral brain cells do not rely on glycolysis as the main energy production mechanism, possibly explaining why there was no significant change in the pH environment during glucose infusion. The peritumoral pH_i before and during glucose infusion was significantly lower than tumoral pH_i – this may also be a result of aberrant tumor metabolism. As mentioned above, surplus acid is produced because of tumor glycolytic metabolism. Excess acid would travel through the pH gradient to neighboring cells to avoid acidosis which could lead to cell death [2]. In combination with poor tumor perfusion environment explored in previous studies [13-15], all of these factors would lead to a significantly lower peritumoral pH_i . This pH gradient could also be an indication of tumor invasion to the peritumoral region [1,3,22].

Studies have found that the tumor extracellular (pH_e) environment becomes more acidic towards the tumor edge and the peritumoral regions, this is the result of the elevated activation of glucose transporters and poor tumor perfusion [2,3,13-15]. This study indicates a similar pH_i distribution as the peritumoral pH_i is significantly lower than the tumor pH_i . The significant correlation between tumor Lac:Pyr and baseline tumor/peritumor pH_i emphasizes the effect of tumor anaerobic glycolysis on its pH environment. Higher tumor glycolytic activity has been associated with lower extracellular pH (pH_e) [2,6,9,22,23]. In this study, higher tumor anaerobic glycolytic activity is linked with lower tumoral and peritumoral pH_i . A significant correlation was also found between tumor Lac:Pyr and the pH_i gradient from the tumor to peritumor region, with higher Lac:Pyr corresponding to a higher pHG_i . The conversion of pyruvate to lactate during anaerobic glycolysis, as measured with hyperpolarized [1- ^{13}C]pyruvate (Lac:Pyr), more directly captures the process of tumor acidosis, and indicated a directly proportional and significant relationship with the pHG_i across the tumor to peritumor region.

Although all imaging experiments were performed in 24 hours, they were in the span of two days, specifically, FDG-PET on Day 11-13, and CEST followed by the hyperpolarized [1- ^{13}C]pyruvate on the next day. Although this is a practical limitation, all imaging was

completed within 24 hours for each subject and no significant changes were found in tumor volumes as mentioned in our previous publication [13]. Since tumor pH and the glyceemic environment were not identical between these measurement sessions, this could explain the absence of significant correlations between tumor SUV from FDG-PET and tumoral and peritumoral pH_i . The tumor pH environment measured from CEST would be closer to the hyperpolarized pyruvate experiment than during FDG-PET, acquired a day prior. The sequential design of the study also gave rise to distinct glucose conditions prior to the glycolysis measurements. The subjects were normoglycemic before FDG-PET while they were hyperglycemic prior to hyperpolarized $[1-^{13}\text{C}]$ pyruvate experiment as it was conducted the following day immediately after the dynamic CEST experiment. Under the effect of hyperglycemia, directly proportional relationships were found between tumor Lac:Pyr vs. tumor and peritumor ΔpH_i . A higher tumor Lac: Pyr is related to a greater shift towards the basic direction in tumor and peritumor pH_i . This could be because cells in tumoral and peritumoral regions try to maintain pH homeostasis to avoid acidosis which results in cell death [1,2].

In summary, the relationship between tumor intracellular pH environment and tumor glycolysis was examined in this study. Significant inversely proportional relationships between tumor and peritumor pH_i and tumor Lac:Pyr were found; as well as significant directly proportional relationships between tumor and peritumor ΔpH_i and tumor Lac:Pyr. There were several limitations from this study, to follow the radiation safety protocols at different sites, the rats had to be housed at our PET facility overnight before they could be transferred to the MR facility. In the future, experiments could be carried out on a hybrid PET/MR system not only to simplify the experimental procedure but also to provide simultaneous measurements under the same tumor pH and metabolic microenvironment. The precise roles of glucose transporters were not examined in this study – histological information about these transporters will be acquired in future studies, and the correlation between the distribution of these glucose transporters and the tumor pH_i environment can then be evaluated [2,3]. A measurement of pH_e would also aid in interpreting these results. We plan on acquiring this information in a future study simultaneously with acidoCEST

[7,9] to provide a more complete picture of the tumor pH environment. The current 60-min glucose infusion protocol leads to hyperglycemia by the end of the AACID CEST experiment. The acute change in pH_i environment after the glucose infusion was not measured in the current study since a different CEST acquisition protocol was used during the first half of glucose infusion. Moreover, the Lac:Pyr value obtained from the MRSI right after would be elevated under hyperglycemia [13,24,25] – a CEST acquisition promptly following a bolus injection with a moderate dose of glucose will be implemented in the future to avoid an overly large alteration of the tumor glycolytic environment.

3.5 Conclusions:

This study demonstrated that using AACID CEST MRI, a change in tumor pH_i can be detected after glucose infusion, the presence of metabolites with similar resonant frequencies with amine or amide would not significantly affect AACID although the calibrations were distinct under different metabolite concentrations. Tracking changes in tumor pH could provide information about tumor metabolism and pH imaging using AACID CEST MRI can be used as an alternative for tumor metabolic imaging. Hyperglycemia induced by glucose infusion leads to a change in tumoral pH_i that can be detected in vivo using CEST MRI. The relationship between tumor and peritumor pH_i environment and tumor glycolysis were explored. Tumor Lac:Pyr is significantly inversely proportional to tumor and peritumoral pH_i , it is also significantly directly proportion to tumoral and peritumoral ΔpH_i induced by a glucose infusion. The associations emphasize the innate relationship between tumor glycolytic metabolism and the tumor pH environment as well as the peritumor pH environment. A multimodal imaging approach could provide a more complete picture of the process of tumor progression and invasion by monitoring both tumor glycolysis and the change in the pH environment.

3.6 Reference

1. Webb BA, Chimenti M, Jacobson MP, et al. (2011) Dysregulated pH: A Perfect Storm for Cancer Progression. *Nat Rev Cancer* 11(9):671-677.
2. Corbet C, Feron O. (2017) Tumour Acidosis: From the Passenger to the Driver's Seat. *Nat Rev Cancer* 17(10):577-593.
3. Estrella V, Chen T, Lloyd M, et al. (2013) Acidity Generated by the Tumor Microenvironment Drives Local Invasion. *Cancer Res* 73(5):1524-1535.
4. Heiden MG, Cantley LC, Thompson CB. (2019) Understanding the Warburg effect: The Metabolic Requirements of Cell Proliferation. *Science* 324(5930):1029-1033.
5. Stubbs M, Rodrigues L, Howe FA, et al. (1994) Metabolic Consequences of a Reversed pH Gradient in Rat Tumors. *Cancer Res* 54(15): 4011-4016.
6. Lim H, Albatany M, Martínez-Santesteban F, et al. (2018) Longitudinal Measurements of Intra-and Extracellular pH Gradient in a Rat Model of Glioma. *Tomography* 4(2): 46-54.
7. Chen LQ, Howison CM, Jeffery JJ, et al. (2014) Evaluations of Extracellular pH within *in vivo* Tumors using Acidocest MRI. *Magn Reson Med* 72(5):1408-1417.
8. Volk T, Jähde E, Fortmeyer HP, et al. (1993) pH in Human Tumour Xenografts: Effect of Intravenous Administration of Glucose. *Br J Cancer* 68(3):492-500.
9. Longo DL, Bartoli A, Consolino L, et al. (2016) *In vivo* Imaging of Tumor Metabolism and Acidosis by Combining PET and MRI-CEST pH Imaging. *Cancer Res* 76(22):6463-6470.
10. Albatany M, Li A, Meakin S, et al. (2018) Dichloroacetate Induced Intracellular Acidification in Glioblastoma: *in vivo* Detection using AACID-CEST MRI at 9.4 Tesla. *J Neurooncol* 136(2):255-262.
11. McVicar N, Li AX, Gonçalves DF, et al. (2014) Quantitative Tissue pH Measurement during Cerebral Ischemia using Amine and Amide Concentration-Independent Detection (AACID) with MRI. *J Cereb Blood Flow Metab* 34(4):690-698.
12. Lim H. (2017) A Longitudinal Study of Tumour Metabolism Using Hyperpolarized Carbon-13 Magnetic Resonance Spectroscopic Imaging in a Preclinical Model of Glioma. PhD Thesis.

13. Qi Q, Fox MS, Lim H, et al. (2021) Multimodality *in vivo* Imaging of Perfusion and Glycolysis in a Rat Model of C6 Glioma. *Mol Imaging Biol* 23(8): 516-526.
14. Qi Q, Yeung TPC, Lee TY, et al. (2016) Evaluation of CT Perfusion Biomarkers of Tumor Hypoxia. *PLoS One* 11(4): e0153569
15. Yeung TPC (2014) Functional Imaging of Malignant Gliomas with CT Perfusion. PhD Thesis.
16. Gallamini A, Zwarthoed C, Borra A. (2014) Positron Emission Tomography (PET) in Oncology. *Cancers* 6(4): 1821-1889.
17. Silver IA, Erecinska M. (1994) Extracellular Glucose Concentration in Mammalian Brain: Continuous Monitoring of Changes During Increased Neuronal Activity and Upon Limitation in Oxygen Supply in Normo-, Hypo-, and Hyperglycemic Animals. *J Neurosci* 14(8):5068-5076.
18. Zaiss M, Anemone A, Goerke S, et al. (2019) Quantification of Hydroxyl Exchange of D-Glucose at Physiological Conditions for Optimization of GlucoCEST MRI at 3, 7 and 9.4 Tesla. *NMR Biomed* 32(9): e4113
19. Zaiss M, Zu Z, Xu J, et al. (2015) A Combined Analytical Solution for Chemical Exchange Saturation Transfer and Semi-Solid Magnetization Transfer. *NMR Biomed* 28(2):217-230.
20. Yeung TPC, Kurdi M, Wang Y, et al. (2014) CT Perfusion Imaging as an Early Biomarker of Differential Response to Stereotactic Radiosurgery in C6 Rat Gliomas. *Tomography* 9(10): e10981.
21. McVicar N, Li A, Suchý M, et al. (2013) Simultaneous *in vivo* pH and temperature mapping using a PARACEST-MRI contrast agent. *Magn Reson Med* 70(4):1016-1025.
22. Webb BA, Chimenti M, Jacobson MP, et al. (2011) Dysregulated pH: A perfect storm for cancer progression. *Nat Rev Cancer* 11(9):671-677.
23. Coman D, Huang Y, Rao JU, et al. (2016) Imaging the intratumoral-peritumoral extracellular pH gradient of gliomas. *NMR Biomed* 29(3):309-319.
24. Lund J, Ouwens DM, Wettergreen M, et al. (2019) Increased Glycolysis and Higher Lactate Production in Hyperglycemic Myotubes *Cells*. 8(9):1011.
25. Twarock S, Reichert C, Peters U, et al. (2017) Hyperglycaemia and Aberrated Insulin Signalling Stimulate Tumour Progression via Induction of the Extracellular Matrix Component Hyaluronan. *Int J cancer* 141(4):791-804.

Chapter 4

Evaluation of the Change in Tumor Intra-/Extracellular pH Environment Induced by Glucose Injection and its Relationship with Tumor Glycolysis in a C6 Rat Model of Glioblastoma

Qi Qi, Matthew S. Fox, Heeseung Lim, Rebecca Sullivan, Harris Smailovic, Alex Li, Miranda Bellyou, Lise Desjardins, Andrew McClennan, Robert Bartha, Lisa Hoffman, Timothy J. Scholl, Ting-Yim Lee, Jonathan D. Thiessen

In the previous chapter, we explored the relationship between tumor glycolysis and its intracellular pH environment, but the information regarding extracellular pH in the tumor was missing. In this chapter, we investigated tumor glycolysis along with both intra- and extracellular pH. One of the hallmarks of glioblastoma is the reliance on glycolytic metabolism, even with adequate oxygen supply. Excess acid and H^+ are produced from glycolysis, resulting in a more acidic tumor environment. Consequently, a glucose injection could lead to a drop in tumor pH. Chemical exchange saturation transfer (CEST) MRI can be used *in vivo* to detect intracellular pH (pH_i) with amine and amide concentration independent detection (AACID) as mentioned in previous chapter, and extracellular pH (pH_e) with acidoCEST using iopamidol. Glucose metabolism can be evaluated using kinetic modeling of dynamic positron emission tomography (PET) data obtained from ^{18}F -fluorodeoxyglucose (FDG). In this chapter, we compared CEST measurements of AACID and acidoCEST to FDG-PET to explore the relationship between the tumor pH environment and glycolytic metabolism. We demonstrate the capability of simultaneous measurements of pH_i and pH_e using CEST MRI and provided a more complete picture of tumor pH environment. Metabolic rate of glucose (MRGlu) was used to demonstrate the intrinsic relationship between tumor glycolysis and tumor pH_e .

4.1 Introduction

Aerobic glycolysis is used as a primary energy production method for cancer cells, in contrast with normal mammalian cells, that rely on more efficient oxidative phosphorylation as the main means for energy production. Due to the overreliance on aerobic glycolysis (Warburg effect), excess H^+ and lactic acids are produced as a byproduct, and the amount produced is directly proportional to the level of glycolytic activity [1–3]. In order to avoid intracellular acidosis, cancer cells are innately equipped with a number of proton or acid transporters such as monocarboxylate transporters (MCTs) to help transfer these acids to the extracellular space. When compared to normal mammalian cells, a slightly more alkaline intracellular pH (pH_i) in combination with a more acidic extracellular pH (pH_e) are the result of cancer cell pH regulation. This pH distribution is regarded as a hallmark of malignant cancers and the pH gradient across intra- and extracellular space is found to be associated with low survival outcome [4]. The acidic pH_e has also been found to benefit cancer proliferation, as it can promote cancer cell invasion, metastasis and decrease the effectiveness of conventional cancer treatments [2,3]. In order to reverse the detrimental outcome due to the cancer pH profile, chemotherapy agents have been designed to neutralize the acidic pH_e or acidify the pH_i [3]. It is important to monitor these processes *in vivo* to track if treatment outcome is achieved.

Chemical exchange saturation transfer (CEST), a magnetic resonance imaging (MRI) technique, enables the surveillance of pH changes *in vivo* [5,6]. Amine and amide concentration independent detection (AACID) is sensitive to pH_i . It is based on distinct, pH-mediated proton exchange behaviors between intracellular amine (2.75 ppm) and amide (3.5 ppm) metabolites with the intracellular water pool [7,8]. Another CEST technique, acidoCEST, is sensitive to pH_e . It relies on an exogenous contrast agent, iopamidol, which only occupies the extracellular space. Similar to AACID, protons in two distinct amide groups on iopamidol have pH-mediated exchange properties that can be measured using CEST [9,10]. These two CEST methods rely on metabolite resonant frequencies with sufficient separation to enable simultaneous measurements of pH_i and pH_e .

Aerobic glycolysis can be monitored with positron emission tomography (PET) using ^{18}F -fluorodeoxyglucose (FDG). FDG is a glucose analogue often used to evaluate cancer glycolytic metabolism. FDG pharmacokinetics can be represented by an irreversible, two-tissue compartment model, simplified by using a Patlak graphical analysis method [11]. The metabolic rate of glucose (MRGlu) can be derived from the kinetic analysis to provide an accurate evaluation of aerobic glycolysis [12].

In this study, the intrinsic relationship between tumor glycolytic metabolism and tumor pH environments (pH_i and pH_e) are evaluated. To monitor acute alteration of intra- and extracellular tumor pH environments simultaneously using CEST, a glucose injection was used to induce a change in pH.

4.2 Methods:

4.2.1 Experiment Design

All procedures were performed in compliance with the Canadian Council for Animal Care.

C6 glioma tumor cells were implanted using stereotactic surgery on Day 0 followed by an MRI tumor check on Day 7 to see if the longest diameter of the tumor had reached 4 mm [13–15]. The FDG-PET experiment was performed on Day 11. The animals were kept in the PET facility overnight for radiation decay before being transported to the 9.4 T MR facility for the CEST experiment on the following day (Day 12). Subjects were euthanized immediately after the CEST experiment, and the brain tissues were extracted, fixed and stained using hematoxylin and eosin (H&E). Experimental timeline and the detailed CEST experiment design are shown in **Figure 4.1**.

4.2.2 C6 cell implantation

Male Wistar rats (Charles River, Canada, age 8 to 10 weeks at surgery) weighing on average 301.5 ± 22 g ($N = 11$) were used in this study. The animals were induced with 5% isoflurane and were maintained at 2-3% for all surgical and imaging procedures.

Detailed C6 glioma cell culturing and implantation can be found in a previous publication [13,15]. In short, 1 million C6 glioma cells were injected 3–4 mm from the skull surface at a burr hole 1 mm anterior and 3 mm right of the bregma and with a Hamilton syringe with the aid of a stereotactic frame. The burr hole was sealed with bone wax, and the incision

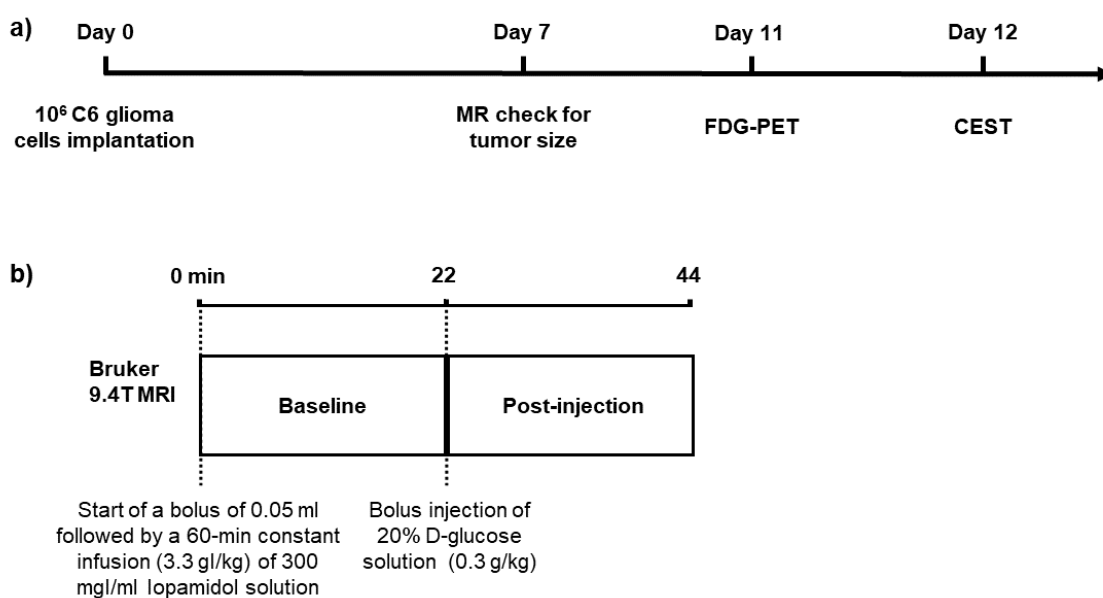


Figure 4.1: **a)** Study overview, Day 0 denotes the day of C6 glioma cell implantation. An MR tumor check took place on Day 7. The FDG-PET experiment was carried out on Day 11, with follow up CEST experiment on the morning of the next day (within 24 hours). **b)** Simultaneous AACID and acidoCEST experimental design. A bolus (0.05 ml) followed by the start of a constant infusion (3.3 gI/kg over 44 minutes) of 300 mgI/ml of Iopamidol took place prior to the start of the CEST acquisition. A baseline CEST acquisition took place before the bolus injection of 20% D-glucose (0.3 g/kg), followed by another post-injection CEST acquisition.

was closed with sutures. The subjects were recovered and returned to the animal care facility.

4.2.3 Benchtop blood glucose measurement

Dynamic blood glucose changes were measured by sampling blood from a rat tail artery (weight = 510 g) and measuring blood glucose with a glucometer (Contour 7152B, Bayer HealthCare, Leverkusen, Germany) on the benchtop using the same glucose injection protocol used during the CEST experiments. The baseline blood glucose was measured before the injection of a bolus of 20% glucose-saline solution (0.3 g/kg of the rats). The blood glucose of the subject was measured approximately every 5 minutes after the start of glucose infusion for 40 minutes.

4.2.4 MR tumor check

Subjects were imaged on Day 7 using a 3T MRI (Siemens Biograph mMR) with a transmit/receive quadrature rat brain RF coil (Cubresa, 44 mm inner diameter). A turbo spin echo (TSE) sequence (128 x 128 field-of-view, FOV; 0.2-mm in-plane resolution; 3-mm slice thickness; slice number = 10; repetition time, TR = 4710 ms; echo time, TE = 100 ms; 10 echo trains and 4 averages) was used to acquire axial T₂-weighted MRI. A line of the longest diameter was drawn on the tumor to confirm it was longer than 4 mm [13,16].

4.2.5 FDG-PET

The FDG-PET acquisition took place on Day 11 using a small animal PET system (Inveon DPET, Siemens Healthineers, Knoxville, TN, USA). The blood glucose level of each subject was tested using the same glucometer prior to FDG-PET acquisition. A 90-minute emission scan was performed with a timing window of 3.432 ns and 350-640 keV discrimination energy range. Approximately 30 s after the acquisition had started, a bolus of ¹⁸F-FDG (34.3 ± 4.8 MBq) was injected through a lateral tail vein.

Longitudinal PET data were histogrammed into 53 successive time intervals comprised of 1 frame of 30 s, 20 frames of 3 seconds, 7 frames of 30 seconds, 10 frames of 60 seconds and 15 frames of 300 seconds, totaling 90 minutes. An iterative, 3D ordered subset expectation maximization (OSEM3D) reconstruction was used to generate dynamic images for all frames with 2 iterations and 18 subsets.

4.2.6 CEST experiment

MRI was acquired on a 9.4-T small animal MRI (Bruker Corporation, Billerica, Massachusetts, USA) the day after PET on Day 12. Axial T₂-weighted images using a 2-dimensional fast spin-echo (FSE) sequence (TR = 3000 ms; TE = 10 ms; effective TE = 40 ms; echo train length = 4; number of slices = 29; slice thickness = 1 mm; FOV = 3.84 × 3.84 cm; matrix size = 128 × 128; acquisition time = 179 s) were acquired first to locate the slice that contained the largest tumor cross-section axially.

CEST spectra were acquired using a continuous echo planar imaging (EPI) sequence, with a series of EPI images acquired on the same axial slice localized using the FSE sequence. The parameters for the EPI sequence are saturation time (TS) = 5 s; B₁ = 3 μT; offset frequency pulse alternated between negative and positive, from -6/+6 to 0 ppm with 0.2 ppm steps; TR = 10 s; effective TE = 25 ms; echo train length = 48; slice thickness = 2 mm; FOV = 3.84 × 3.84 cm FOV; matrix size = 96 × 96, number of averages = 2, acquisition time = 22 min. Two spectra were obtained from two consecutive 22 min CEST acquisitions. A bolus of 300 mgI/ml of iopamidol (0.05 ml, Isovue, Bracco Diagnostics Inc, Vaughan, Canada) was injected prior to the first CEST acquisition, along with a 44-min constant infusion of the same concentration of iopamidol at a dose of 3.3 gI/kg. The first CEST spectrum (Baseline) was acquired prior to the glucose injection. A bolus of 20% D-glucose solution (0.3 g/kg, Sigma Aldrich, Miamisburg OH, USA) was injected at the end of the first spectrum acquisition. The acquisition of the second (Post-injection) CEST spectra took place after the glucose injection.

The post injection CEST spectrum was used to compare with the baseline CEST spectrum to examine the effect of glucose infusion on pH_i and pH_e .

4.2.7 Kinetic analysis of FDG-PET

PET kinetic analysis was performed using PMOD 3.9 (PMOD Technologies LLC, Zürich, Switzerland). An arterial input function (AIF) was defined using the averaged time-activity curve (TAC) from an ROI drawn covering the left ventricle. The equation for the Patlak plot is shown in **Equation 4.1**. The whole brain including the tumor region was delineated and the pixel-wise TACs were normalized by the input function and plotted against the ratio of the integral of the input function and input function (Patlak graphical analysis, [11]).

$$\frac{TAC(t)}{AIF(t)} = K_i \times \frac{\int_0^T AIF(t)}{AIF(t)} + Int \quad [4.1]$$

Where Int is the y-axis intercept and the slope of the linear portion, representing the net transfer rate (K_i), was obtained and converted into MRGlu using **Equation 4.2**.

$$MRGlu = K_i \times \frac{C_{Glucose\ Plasma}}{LC} \quad [4.2]$$

Where $C_{Glucose\ Plasma}$ is the plasma glucose concentration measured prior to FDG injection, and LC is the lumped constant, a conversion factor to estimate the glucose metabolic rate from the glucose analog FDG. $LC = 0.71$ was used based on literature [17,18].

4.2.8 acidoCEST phantom calibration

In order to test the effect of glucose on acidoCEST, two pH phantoms were made using modified recipes from published works [9,10]. One phantom was used as a control (i.e., without glucose), it holds seven NMR tubes (Sigma Aldrich, Miamisburg OH, USA), and each tube contains a mixture of 1 × phosphate buffered saline (PBS, pH = 7) and the same concentration of iopamidol (30 mM). pH of the solution in each tube was titrated by either adding sodium hydroxide (NaOH) or hydrogen chloride (HCl) to obtain seven pH levels from 6.2 to 7.4 with 0.2 increments. The second phantom was made with the same pH levels with the addition of 6 mM glucose to mimic brain tissue glucose levels under hyperglycemia [19].

As shown in **Equation 4.3**, the magnetization transfer ratio asymmetry (MTR_{asym} , [5,6]) was calculated at the resonant frequencies of the exchangeable protons of the two amide functional groups in iopamidol (4.2 and 5.5 ppm).

$$MTR_{\text{asym}} = \frac{S_{-\Delta\omega} - S_{\Delta\omega}}{S_0} \quad [4.3]$$

pH vs. the corresponding MTR_{asym} values at the two resonant frequencies with (**Figure 4.2a**) and without glucose (**Figure 4.2b**) were plotted. The ratios of the MTR_{asym} signals at the resonant frequencies (4.6 and 5.5 ppm) of the two amide functional groups on iopamidol were calculated (**Equation 4.4**).

$$R_{\text{ST}} = \frac{MTR_{\text{asym}}(4.2 \text{ ppm})}{MTR_{\text{asym}}(5.5 \text{ ppm})} \quad [4.4]$$

The relationship between R_{ST} and the corresponding pH was plotted in **Figure 4.2c**. An exponential function was fitted and plotted, and the goodness-of-fit was tested. The equation was then used to convert the ratio obtained from *in vivo* CEST experiments to pH.

The area under the curve (AUC) was also calculated using MTR_{asym} (AUC_{MTR}) values from 1.2 to 2.8 ppm to generate regional glucose maps [15].

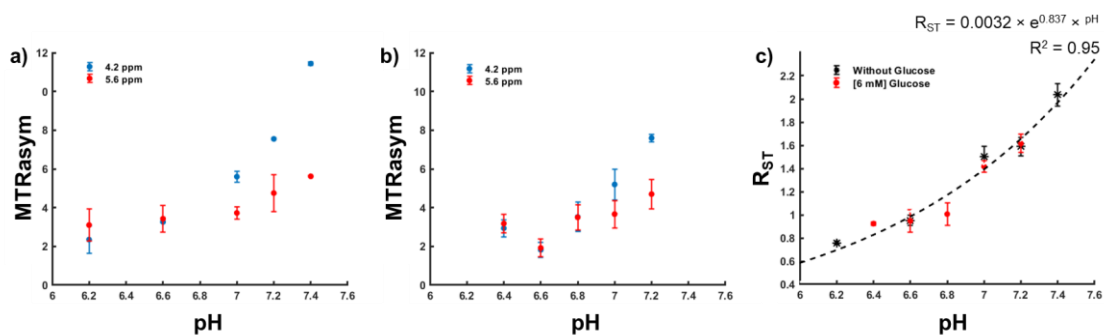


Figure 4.2: pH vs. MTRasym values at the resonant frequencies of the exchange protons on the two amide functional groups on iopamidol without **a.** and with **b.** the presence of glucose (6 mM). **c.** pH vs. the corresponding R_{ST} value calculated using acidoCEST measurements obtained from the phantom experiments. Error bar = standard deviation.

4.2.9 Tumoral and peritumoral pH_i , pH_e and pH gradient

AACID values were calculated from the Z-spectra using **Equation 4.5** for both baseline and post-injection CEST acquisitions. Calculated AACID values were converted using the same calibration as indicated in **Equation 4.6** from a previous study (Chapter 2, [15]). The ratio (R_{ST}) obtained from acidoCEST was converted to pH_e using an exponential calibration derived from the phantom experiment described above. pH gradient (pHG) across the intra- to extracellular space was calculated as shown in **Equation 4.7**.

$$AACID = \frac{Mz_{(3.50 \text{ ppm})} \times (Mz_{(6 \text{ ppm})} - Mz_{(2.75 \text{ ppm})})}{Mz_{(2.75 \text{ ppm})} \times (Mz_{(6 \text{ ppm})} - Mz_{(3.50 \text{ ppm})})} \quad [4.5]$$

$$AACID = -0.45 \times pH_i + 4.88 \quad [4.6]$$

$$pHG = pH_i - pH_e \quad [4.7]$$

4.2.10 Histology

Animals were euthanized with an overdose of potassium chloride immediately after the end of CEST experiment. The animals were perfusion-fixed with phosphate buffered saline followed by 4% paraformaldehyde. Brains were removed and fixed in 4% paraformaldehyde for 24 hours. Brain specimens were sectioned into 3 mm thick blocks, paraffin-embedded, sectioned at 5 μm in the axial orientation picked up on positively charged microscope slides and dried overnight at 37°C. The brain sections were deparaffinized in xylene, hydrated through graded alcohols and washed in water. The slides were then placed in a bath of 3% H_2O_2 for 10 minutes to block peroxidase activity, washed in running tap water for 5 minutes, rinsed in distilled water and placed in pH 7.4 PBS. The slides were incubated 40 minutes at room temperature. The slides were then washed 3 x 5 minutes with PBS before DAB (3,3'-diaminobenzidine, Vector Laboratories, Inc.) was applied for 8 minutes. The slides were subsequently washed in running tap water, counterstained with Carazzi's haematoxylin for 1 minute, washed with tap water, dehydrated through graded alcohols, cleared in xylene and mounted.

The brain slides were imaged and captured using a digital bright-field microscope (Zeiss Axioscope, Oberkochen, Germany).

4.2.11 Image registration and ROI selection

Detailed description can be found in a previous publication (Chapter 2, [15]). T_2 -weighted MRI was used as guidance for manual delineation of tumor, peritumor and contralateral brain regions as well as a reference for coregistration of CEST MRI, FDG-PET and histology images using 3D Slicer (www.slicer.org). The average tumoral, peritumoral and contralateral brain pH_i , ΔpH_i , pH_e , ΔpH_e and pHG from CEST, along with MRGlu from FDG-PET, were extracted. Illustrative examples of co-registered CEST, PET and histology, and the delineations of the three different regions are shown in **Figure 4.3** and **Figure 4.4**.

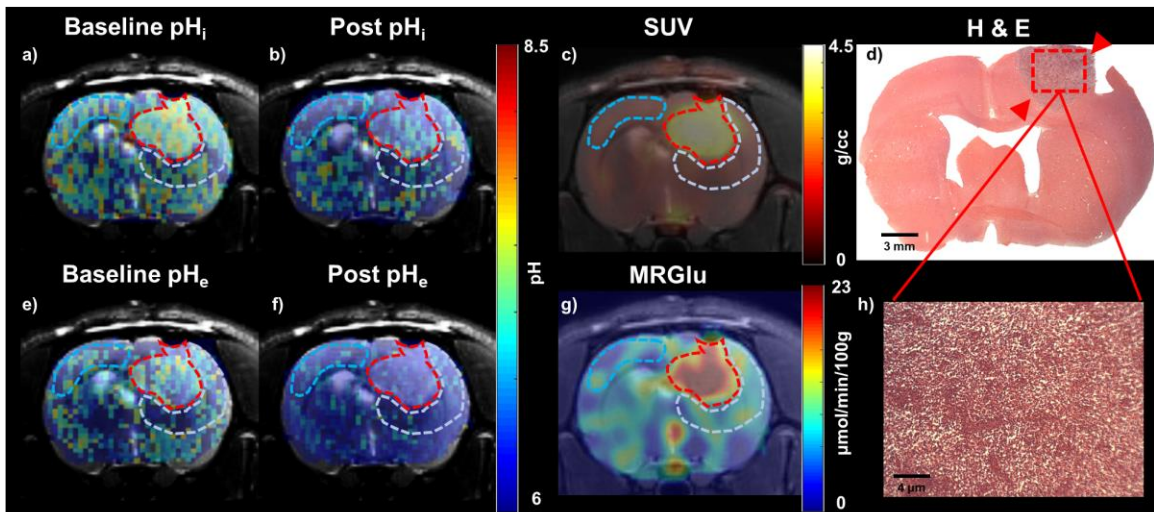


Figure 4.3: Illustrative example of all registered images and ROIs for one rat. T_2 -weighted MRI acquired on the 9.4 T MRI is used as a reference to co-register CEST MRI (a, b, e and f), FDG-PET (c and g) and the corresponding H&E images with different magnifications (d and h). The tumor, peritumor and contralateral brain regions are delineated using the T_2 -weighted MRI with the red-, beige- and blue-dotted lines respectively.

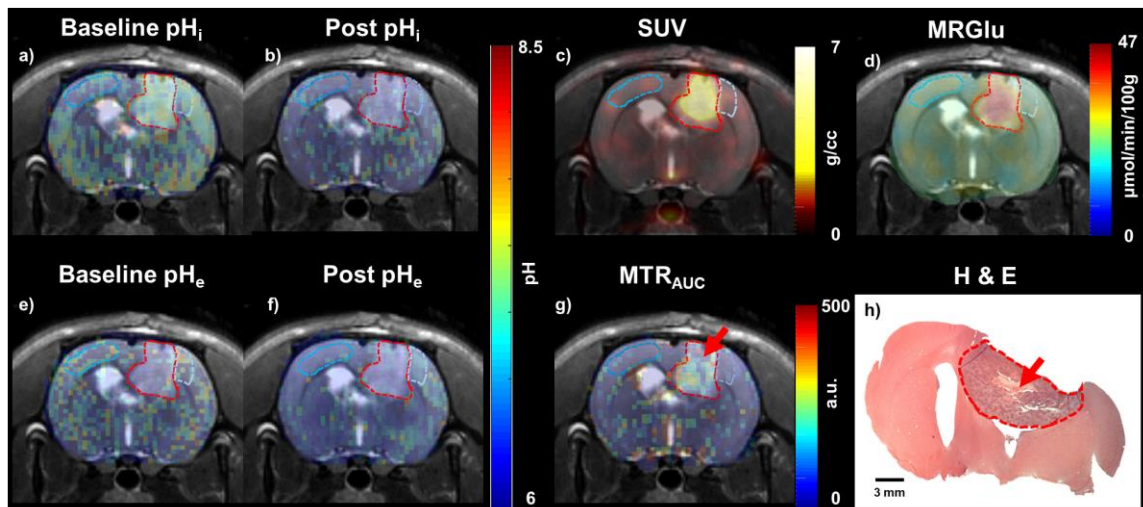


Figure 4.4: Illustrative example of all registered images and ROIs for another rat, T_2 -weighted MRI acquired on the 9.4 T MRI is used as a reference to co-register CEST MRI (a, b, e, f and g), FDG-PET (c and d) and the corresponding H&E image (h). The tumor, peritumor and contralateral brain regions are delineated using the T_2 -weighted MRI with the red-, beige- and blue-dotted lines respectively. The red arrows indicate a potential co-localization of tumor necrosis between CEST MRI and histology.

4.2.12 Statistical analysis

A two-tailed paired T-test was performed to determine if significant differences ($P < 0.05$) can be found in tumoral and peritumoral pH after a bolus injection of glucose solution. Pearson's correlation test was used to investigate the relationship between tumor glycolytic measurement of MRGlu with tumoral and peritumoral pH environment measurements (pH_i , pH_e and pHG) as well as glucose distribution (AUC_{MTR}). A P-value less than 0.05 was defined as a significant correlation.

4.3 Results:

4.3.1 Blood glucose measurement

Benchtop measurements of blood glucose as a function of time during the glucose infusion protocol are plotted in **Figure 4.5**. The baseline blood glucose of the subject was 6.9 mmol/L and increased to 15.3 mmol/L 15 minutes after the bolus injection of glucose, the blood glucose later dropped to 9.3 mmol/L 30 minutes after the injection (i.e., end of the injection protocol).

During the *in vivo* CEST experiment, the average blood glucose level at baseline was 7.2 ± 2.3 mM, and the average blood glucose level post-injection was significantly higher, at 15.6 ± 5.5 mM.

4.3.2 Calibration of acidoCEST to pH_e

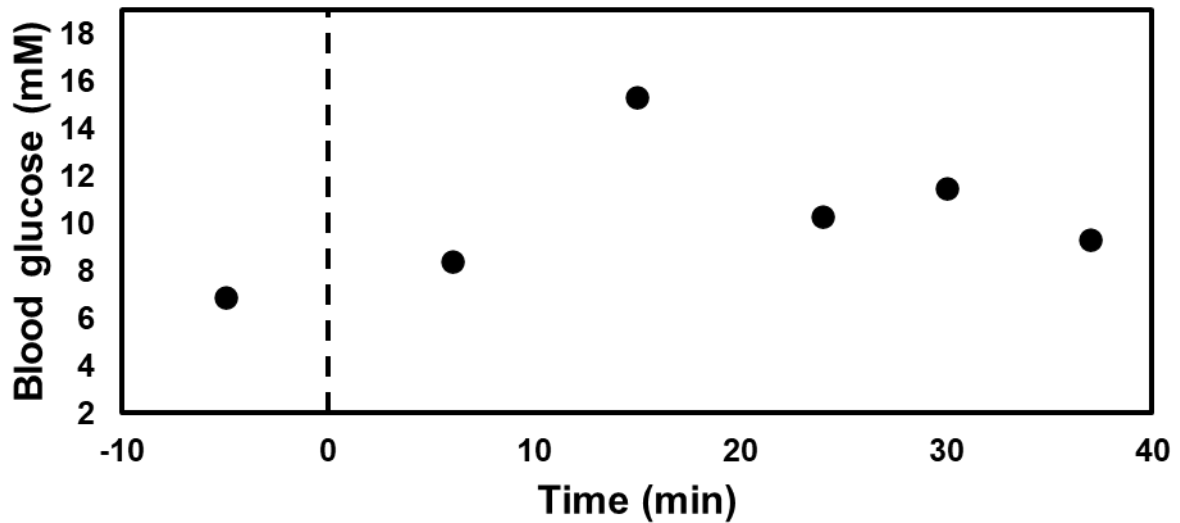


Figure 4.5: An illustrative example of blood glucose changes 30 minutes after an injection of a bolus of 20% glucose solution (0.3 g/kg).

After examining the relationship between pH_e vs. R_{ST} from the two phantoms (with and without glucose), no significant differences were found in R_{ST} values at each pH_e value regardless of the presence of glucose (**Figure 4.2**).

The equation of between pH_e and R_{ST} obtained from the line-of-best-fit indicated by an exponential function was:

$$R_{ST} = 0.0032 \times e^{0.837 \times \text{pH}}$$

and the goodness-of-fit (R^2) was 0.95.

4.3.3 The effect of glucose injection on pH_i and pH_e

Baseline and post-injection averaged pH_i and pH_e in tumor, peritumor and contralateral brain tissue are illustrated in **Figure 4.6**. After the glucose injection, a significant decrease in pH_i was found in tumor ($P = 0.02$) and peritumor ($P = 0.01$) regions but not in the

contralateral brain region ($P = 0.12$). A significant decrease in pH_e was found in tumor ($P < 0.01$), peritumor ($P < 0.001$) and contralateral brain tissue ($P = 0.03$) regions.

At baseline, tumor pH_i was significantly higher than pH_i in peritumor ($P < 0.01$) and contralateral brain regions ($P = 0.04$), and tumor pH_e was significantly lower than pH_e in peritumor ($P = 0.03$) and contralateral brain ($P = 0.02$) regions; peritumor pH_e was significantly lower than contralateral brain pH_e ($P = 0.01$).

After glucose injection, pH_i in tumor and peritumor regions were significantly lower than pH_i in the contralateral brain region ($P = 0.03$ and $P < 0.001$ respectively), tumor pH_i was significantly higher than the peritumor region ($P = 0.02$); tumor and peritumor pH_e were both significantly lower than contralateral brain pH_e ($P < 0.01$ and $P = 0.01$ respectively).

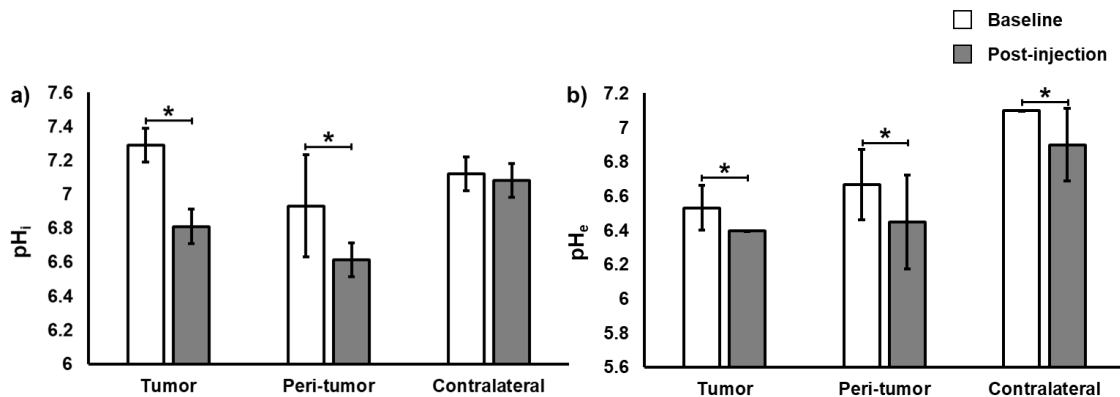


Figure 4.6: Mean pH values of all rats ($N = 11$) from ROIs defined in tumor, peritumor and contralateral brain tissue in pH_i (a) and pH_e (b) at baseline and post-injection. Error bar = standard deviation.

4.3.4 Kinetic analysis results

The averaged MRGlu values in the tumor, peritumor and contralateral brain regions are illustrated in **Figure 4.7**, MRGlu in tumor region is significantly higher than peritumor (P

< 0.001) and contralateral brain ($P < 0.001$) MRGlu. MRGlu in the peritumor region is not significantly different from the contralateral brain region ($P = 0.67$).

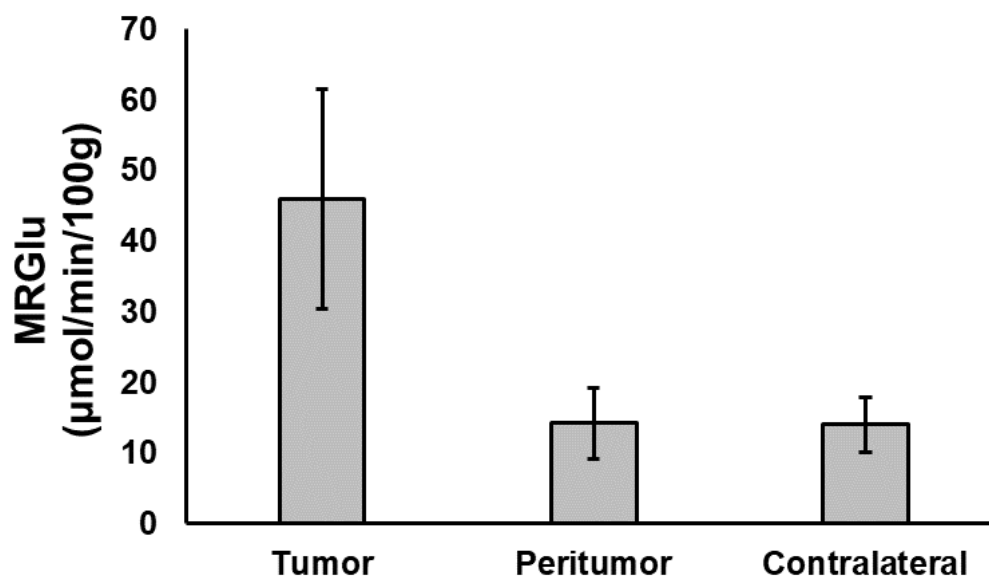


Figure 4.7: Mean MRGlu measurement in the tumor, peritumor and contralateral brain regions. The error bar = standard deviation.

4.3.5 Correlation between tumoral, peritumoral pH measurement and tumor glycolysis

As shown in **Table 4.1**, significant correlations were found between baseline tumor glycolytic measurement of MRGlu and tumor pH_i ($\rho = 0.78$, $P = 0.03$) (**Figure 4.8a**), tumor pH_e ($\rho = -0.87$, $P < 0.001$) (**Figure 4.8b**), as well as the tumor pHG ($\rho = 0.70$, $P = 0.012$).

Table 4.1: Pearson's correlation among baseline tumor glycolysis measurements (MRGlu), tumor and peritumor pH environments (pH_i , pH_e and pHG) and AUC_{MTR} . The asterisk indicates a statistical significance of $P < 0.05$.

$N = 11$	pH_{i_t}	pH_{i_p}	pH_{e_t}	pH_{e_p}	pHG	AUC_{MTR}
MRGlu	0.78*	0.56	-0.87*	-0.47	0.70*	0.14

As shown in **Table 4.2**, tumor and peritumor ΔpH_i are significantly correlated ($\rho = 0.81$, $P < 0.001$), the tumor and peritumor ΔpH_e are also significantly correlated ($\rho = 0.81$, $P < 0.001$). Tumor MRGlu is inversely proportional and significantly correlated with ΔpH_e in the tumor region ($\rho = -0.83$, $P = 0.02$) (**Figure 4.8c**). Tumor ΔpH_i is inversely proportional and significantly correlated with peritumor ΔpH_e ($\rho = -0.65$, $P = 0.02$) (**Figure 4.8d**).

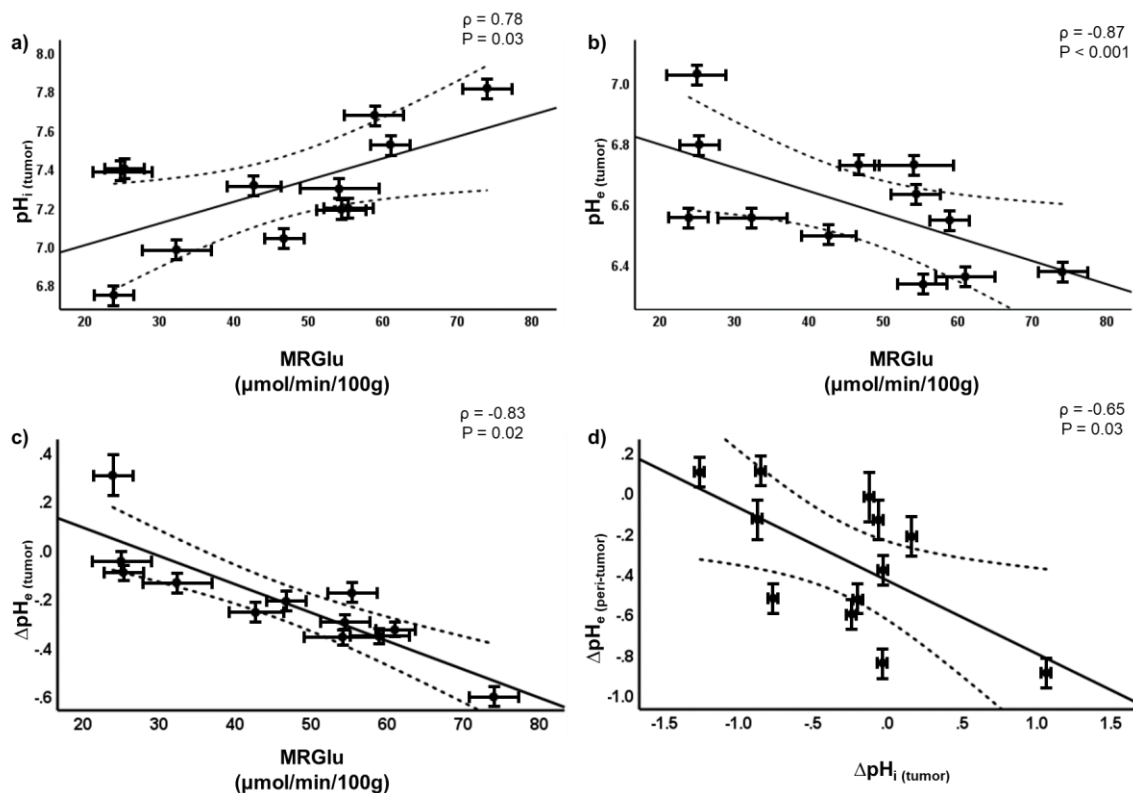


Figure 4.8: Tumor glycolytic measurement of MRGlu vs. tumor pH_i **a**, tumor pH_e **b**, tumor ΔpH_e **c**, and tumor ΔpH_i vs. peritumor ΔpH_e **d**. The dotted line indicates the 95% confidence interval, and the error bar denotes the standard deviation.

4.3.6 Histological validation

The H&E staining indicated the location of tumor highlighted by the red arrows as shown in **Figure 4.3d**, the zoomed-in tumor region is shown in **Figure 4.3h**. A potential co-localization of necrosis between CEST MRI and histology is indicated by the arrows in **Figure 4.4g** and **4.4h**.

Table 4.2: Pearson's correlation among tumor glycolysis measurement (MRGlu) and tumor and peritumor ΔpH (ΔpH_t and ΔpH_e) induced by glucose injection. The asterisk indicates a statistical significance of $P < 0.05$.

$N = 11$	MRGlu	ΔpH_t	ΔpH_p	ΔpH_e
ΔpH_t	0.45			
ΔpH_p	0.28	0.81*		
ΔpH_e	-0.83*	-0.04	0.13	
ΔpH_p	0.26	-0.65*	0.53	0.78*

4.4 Discussion

In this study, the association between glycolysis and tumor pH environment was investigated *in vivo* in the C6 rat model using FDG-PET and CEST. All imaging experiments were performed within 24 hours and the tumor size should not change significantly within a 24-hour span according to our study presented in Chapter 2 [15].

From the phantom experiment, the addition of glucose solution did not affect the R_{ST} values at different pH, as the R_{ST} values derived from the phantom containing glucose (with a

concentration of 6 mM) were not significantly different from the phantom without glucose across a range of physiologically-relevant pH values. As a result, the R_{ST} values from both phantoms were used, and the exponential relationship between pH_e and R_{ST} was determined. The equation used to calibrate *in vivo* R_{ST} to pH_e produced *in vivo* tumor extracellular pH levels (average 6.53 ± 0.11 , mean \pm standard deviation) similar to the pH_e level obtained from Chen et al. (~ 6.5 , [9]), Lim et al. (7.19 ± 0.11 [4]), Volk et al. (6.79-6.85, [19]) and Longo et al. (6.5-7.1, [10]).

At baseline, the average tumor pH_i measured using AACID is 7.29 ± 0.12 , higher than pH_i in the peritumor and contralateral brain regions. Meanwhile, the average tumor pH_e measured using acidoCEST was lower than in peritumor and contralateral brain regions. This was a likely result of the Warburg effect, with an alkaline pH_i in combination with a more acidic pH_e aiding in tumor proliferation [1,2,4]. The average tumor pH_i obtained from this study (7.29 ± 0.10) was very similar to a previous study by Lim et al. (7.30 ± 0.09 , [4]). This indicates that the calibrations used from this study could produce acceptable results. Importantly, we were able to measure intra- and extracellular pH simultaneously during this study, with the presence of a glucose solution in the system having no apparent effect on our pH_i estimates. The resonant frequencies needed for acidoCEST are further away from glucose, amine and amide resonant frequencies, as a result, no significant difference was found for R_{ST} values with and without glucose at various pH as shown in the phantom result.

After glucose injection, significant decreases in intra- and extracellular pH in both tumor and peritumor regions were detected using AACID and acidoCEST simultaneously. The injected glucose was utilized in tumor glycolysis and led to an acute decrease in tumor and peritumor pH environment (pH_i and pH_e) as more H^+ and acid were produced through glycolysis. A drop of 0.3-0.4 in pH_e was found across various cancer types after an intravenous infusion of glucose solution. by Volk et al. [19]; meanwhile, a drop of 0.72 in pH_i was observed by Albatany et al. [20] after an intraperitoneal glucose injection. The results from this study illustrated a similar decrease in pH_i and pH_e (a decrease of $0.41 \pm$

0.1 and 0.30 ± 0.07 respectively) with a bolus injection of glucose. The excess H^+ and acid produced by the tumor cells due to glucose injection could accumulate in the peritumor regions as the upregulation H^+ and acid transporters especially at the edge of the tumor [1–3], in turn these H^+ and acid are transferred to the peritumor region and alter the pH environment in these regions. This could indicate the process of tumor invasion, as acidosis led apoptosis in peritumor regions results in the breakdown of the extracellular matrix and help tumors spread into these areas [1,2]. The possibility of detecting a pH environment change induced by a glucose injection could be valuable to observe other pH alteration procedures in cancer treatment to monitor treatment outcomes.

The tumor MRGlu was significantly greater than peritumor and contralateral brain tissue, further highlighting the Warburg effect, with higher glycolytic metabolism in tumor compared to contralateral brain tissue as well as peritumor tissue. Although the peritumor region could potentially be a site of tumor invasion, the rate of glycolysis was not significantly higher when compared to contralateral brain tissue.

The tumor MRGlu derived from FDG-PET kinetic analysis was significantly correlated with the tumor baseline pH_i , pH_e and pHG . Greater tumor MRGlu is associated with higher tumor pH_i , lower tumor pH_e and a higher pHG . This matches what we would expect to see in tumors with higher glycolytic activity, leading to a more acidic pH_e and a greater pHG across the intra- and extracellular space. pHG has been found to be associated with tumor proliferation [4], more alkaline or higher pH values are associated with higher tumor mitotic activity [4] which is a hallmark of glioblastoma [21,22], and this study has provided additional information on the association with tumor metabolism and growth. This further highlights the intrinsic relationship between the Warburg effect in the tumor and its pH environment.

Tumor ΔpH_i and ΔpH_e are significantly correlated with peritumor ΔpH_i and ΔpH_e respectively. Tumor and peritumor pH environments changed concurrently when induced by the glucose injection. This might indicate the innate relationship between the tumor and peritumor pH environment, as well as the effect of tumor glycolytic activity on the pH

environments. Significant correlation was found between tumor MRGlu and tumor ΔpH_e , showing that higher tumor glycolytic activity is associated with a greater decrease in tumor pH_e . The injection of glucose will lead to elevated production of H^+ and acid in the tumor based on the tumor glycolytic activity, and they will be transported to the extracellular space and lead to a greater drop in pH_e . An inversely proportional and significant relationship was found between tumor ΔpH_i and peritumor ΔpH_e , with an increase in tumor ΔpH_i linked to a decrease in peritumor ΔpH_e . Under elevated glucose conditions, as more H^+ and acid are produced, tumor cells will transport these H^+ and acid out of the cells to avoid acidosis. As a result, H^+ and acid accumulate not only in the tumor extracellular space but could also spill over into the peritumor extracellular space [1,23].

Although significant correlation was not found between tumor AUC_{MTR} and FDG-PET measurements from this and previous studies [15], a good colocalization of high intensity regions within the tumor can be seen among AUC_{MTR} and FDG-PET measurements as shown in **Figure 4.3**. From Chapter 2 [15], the low intensity values of AUC_{MTR} within the tumor region was hypothesized to be possible tumor necrosis. In this study, a potential colocalization of tumor necrosis is observed between AUC_{MTR} map and the corresponding histology slide highlighted by the red arrows as shown in **Figure 4.3**. Using CEST measurements of AUC_{MTR} in addition to the pH measurements, the tumor metabolic activity could be estimated.

There are a couple of limitations for this study: the CEST acquisition did not take place right after the PET experiment to follow the radiation safety protocol at different sites. The subjects have to be housed at the PET facility overnight for radiation decay before transferring to the 9.4 T MR facility for imaging, however, the imaging experiments for each subject were performed within a 24-hour span. A hybrid PET/MR system could be used in the future to provide simultaneous measurements under the same tumor microenvironment. The role of glucose transporters is not studied in this study, other studies have demonstrated the inversely proportional relationship between the number of glucose transporters and tumor and peritumor pH_e (more acidic) [1,24]. The Patlak

graphical analysis method assumes the pharmacokinetics of FDG are irreversible [25], i.e. FDG6P will be trapped inside the cells after FDG is phosphorylated. However, a recent study has shown the reversibility of FDG6P trapping, where FDG6P could be fed into pentose phosphate pathway by glucose-6-phosphate dehydrogenase, and in turn be transported out of the cell by GLUTs [26]. A Logan graphic analysis method could be employed to better model FDG pharmacokinetic, as it assumes reversible binding for radiopharmaceuticals [11].

4.6 Conclusion

To our knowledge, this is the first study that demonstrated the possibility of measuring both intracellular and extracellular pH simultaneously using CEST MRI and demonstrated the capability of measuring the tumor intra- and extracellular pH environments, as well as detecting the change in pH after a glucose injection. The intrinsic relationship between tumor and peritumor pH environments (tumor pH_i and peritumor pH_e) could potentially help predict tumor invasion. Tumor glycolytic metabolism and its effect on tumor pH_e was also shown in this study, and further illustrates the importance of understanding the tumor pH environment as it relates to tumor metabolism.

4.7 Reference

1. Estrella V, Chen T, Lloyd M, et al. (2013) Acidity generated by the tumor microenvironment drives local invasion. *Cancer Res* 73(5):1524-1535.
2. Corbet C, Feron O. (2017) Tumour acidosis: From the passenger to the driver's seat. *Nat Rev Cancer* 17(10):577-593.
3. Thews O, Riemann A. (2019) Tumor pH and metastasis: a malignant process beyond hypoxia. *Cancer Meta Rev* 38(1-2):113-129.
4. Lim H, Albatany M, Martínez-Santesteban F, Bartha R, et al. (2018) Longitudinal Measurements of Intra-and Extracellular pH Gradient in a Rat Model of Glioma. *Tomography* 4(2): 46-54.
5. Van Zijl PCM, Yadav NN. (2011) Chemical exchange saturation transfer (CEST): What is in a name and what isn't? *Magn Reson Med* 65(4):927-948.
6. Liu G, Song X, Chan KWY, McMahon MT. (2013) Nuts and bolts of chemical exchange saturation transfer MRI. *NMR Biomed* 26(7):810-828.
7. McVicar N, Li AX, Gonçalves DF, et al. (2014) Quantitative tissue pH measurement during cerebral ischemia using amine and amide concentration-independent detection (AACID) with MRI. *J Cereb Blood Flow Metab* 34(4):690-698.
8. Albatany M, Li A, Meakin S, Bartha R. (2018) Dichloroacetate induced intracellular acidification in glioblastoma: in vivo detection using AACID-CEST MRI at 9.4 Tesla. *J Neurooncol* 136(2):255-262.
9. Chen LQ, Howison CM, Jeffery JJ, et al. (2014) Evaluations of extracellular PH within in vivo tumors using acidocest MRI. *Magn Reson Med* 72(5):1408-1417.
10. Longo DL, Bartoli A, Consolino L, et al. (2016) *In vivo* imaging of tumor metabolism and acidosis by combining PET and MRI-CEST pH imaging. *Cancer Res* 76(22):6463-6470.
11. Logan J. (2000) Graphical Analysis of PET Data Applied to Reversible and Irreversible Tracers. *Nucl Med Biol* 27(7):661-70.
12. Villien M, Wey HY, Mandeville JB, et al. (2014) Dynamic functional imaging of brain glucose utilization using fPET-FDG. *Neuroimage* 100:192-199.
13. Qi Q, Yeung TPC, Lee TY, et al. (2016) Evaluation of CT perfusion biomarkers of tumor hypoxia. *PLoS One* 11(4).
14. Yeung TPC. (2014) Functional Imaging of Malignant Gliomas with CT Perfusion. PhD Thesis.

15. Qi Q, Fox MS, Lim H, et al. (2021) Multimodality In Vivo Imaging of Perfusion and Glycolysis in a Rat Model of C6 Glioma. *Mol Imaging Biol* 23(4):516-526.
16. Yeung TPC, Kurdi M, Wnag Y et al. (2014) CT Perfusion Imaging as an Early Biomarker of Differential Response to Stereotactic Radiosurgery in C6 Rat Gliomas. *Plos One* 9(10): e109781.
17. Tokugawa J, Ravasi L, Nakayama T, et al. (2007) Operational lumped constant for FDG in normal adult male rats. *J Nucl Med* 48(1):94-99.
18. Backes H, Walberer M, Endepols H, et al. (2011) Whiskers Area as Extracerebral Reference Tissue for Quantification of Rat Brain Metabolism Using 18 F-FDG PET: Application to Focal Cerebral Ischemia. *J Nucl Med* 52:1252-1260.
19. Volk T, Jähde E, Fortmeyer HP, et al. (1993) pH in human tumour xenografts: effect of intravenous administration of glucose. *Br J Cancer* 68(3):492-500.
20. Albatany M, Ostapchenko VG, Meakin S, et al. (2019) Brain tumor acidification using drugs simultaneously targeting multiple pH regulatory mechanisms. *J Neuro-Oncology* 144(3):453-462.
21. Hanif F, Muzaffar K, Perveen K, et al. (2017) Glioblastoma Multiforme: A Review of its Epidemiology and Pathogenesis through Clinical Presentation and Treatment. *Asian Pac J Cancer Prev* 18(1):3-9.
22. Wen PY, Weller M, Lee EQ, et al. (2020) Glioblastoma in Adults: a Society for Neuro-Oncology (SNO) and European Society of Neuro-Oncology (EANO) Consensus Review on Current Management and Future Directions. *Neuro Oncol* 22(8):1073-1113.
23. Coman D, Huang Y, Rao JU, et al. (2016) Imaging the intratumoral-peritumoral extracellular pH gradient of gliomas. *NMR Biomed* 29(3):309-319.
24. Lombardi AF, Wong JH, High R, et al. (2021) AcidoCEST MRI Evaluates the Bone Microenvironment in Multiple Myeloma. *Mol imaging Biol* 23(6):865-873.
25. van den Hoff J, Hofheinz F, Oehme L, et al. (2013) Dual time point based quantification of metabolic uptake rates in 18F-FDG PET. *EJNMMI Res* 3(1):1-11.
26. Yang DM, Palma D, Louie A, et al. (2019) Assessment of tumour response after stereotactic ablative radiation therapy for lung cancer: A prospective quantitative hybrid ¹⁸F-fluorodeoxyglucose-positron emission tomography and CT perfusion study. *J Med Imaging Radiat Oncol* 63(1):94-101.

Chapter 5

Discussion and Future Direction

The aim of this thesis is to investigate cancer perfusion, metabolic and pH environment using CEST MRI along with multimodal imaging approach. Conclusion and limitations of each chapter is discussed below.

5.1 Chapter 2: Multimodality In Vivo Imaging of Perfusion and Glycolysis in a Rat Model of C6 Glioma

In this chapter, the association between tumor perfusion and tumor glycolysis was investigated *in vivo* using CTP, FDG-PET and hyperpolarized [1-¹³C]pyruvate MRSI in a C6 rat model of glioma. Dynamic glucose enhancement measurements of tumor Δ CEST were significantly correlated with tumor perfusion measurements of BV and PS but not tumor glycolysis measurements of SUV and Lac:Pyr, suggesting that glucose CEST imaging using Δ CEST functions primarily as a perfusion tracer. Conversely, tumor glycolysis measurements of SUV and Lac:Pyr were significantly correlated with perfusion measurements of PS, reflecting increased tumor leakiness in tumors with higher glycolytic metabolism. Moreover, tumor perfusion measurement of BF and BV were significantly correlated with tumor SUV and Lac:Pyr respectively, this further emphasize that better perfusion environment could result in better glucose delivery to cancer cells and can later be used in cancer glycolytic metabolism.

The ROI defined using the T₂-weighted MRI will contain CSF, and the inclusion of CSF in tumor ROIs could lead to underestimation of all measurements in the tumor regions as CSF is distinct from the contrast agent in the blood vessels and tissue. Although the imaging measurements were conducted within 24 h, they were in the span of 2 days, and on multiple scanners, as a result, the tumor perfusion and glyceic environment were not identical during the measurements. CEST measurements of the immediate response during glucose infusion were missing because CEST experiments for the first 30 min of the

glucose infusion were performed with two different protocols. Confounding these results is the fact that hyperglycemia induced by a constant infusion of glucose during dynamic CEST experiments may lead to a more acidic pH environment and give rise to underestimation of CEST measurements. Subsequently, in approximately half of the dynamic glucose CEST experiments, there was a drop in CEST signal post-glucose infusion. Although glucose CEST measurements may yield additional novel information about tumor status, the complicated dependency of glucose CEST signal on a variety of factors would benefit from additional in vivo mechanistic studies.

5.2 Chapter 3: Glucose Infusion Induced Change in Intracellular pH and Its Relationship with Tumor Glycolysis in a C6 Rat Model of Glioblastoma.

In this chapter, the tumor pH_i environment was evaluated using AACID CEST MRI, and AACID CEST MRI was tested to detect the change in pH_i environment induced by a glucose infusion. The relationship between tumor pH_i environment and its glycolytic activity measured using FDG-PET and hyperpolarized $[1-^{13}\text{C}]$ pyruvate was also investigated. This study demonstrated that using AACID CEST MRI, a change in tumor pH_i can be detected after a glucose infusion is introduced. Tracking changes in tumor pH could provide important information regarding the treatment response from chemotherapy and/or radiotherapy. Hyperglycemia induced by a glucose infusion leads to a change in tumoral pH_i that can be detected in vivo using CEST MRI. The relationship between tumor and peritumor pH_i environment and tumor glycolysis were explored. Tumor Lac:Pyr is significantly inversely proportional to tumor and peritumoral pH_i , it is also significantly directly proportional to tumoral and peritumoral ΔpH_i induced by a glucose infusion. The associations emphasize the innate relationship between tumor glycolytic metabolism and the tumor pH environment as well as the peritumor pH environment. A multimodal imaging approach could provide a more complete picture of the process of tumor progression and invasion by monitoring both tumor glycolysis and the change in the pH environment.

There were several limitations from this study. To follow the radiation safety protocols at different sites, the rats had to be housed at our PET facility overnight before they could be transferred to the MR facility. In the future, experiments could be carried out on a hybrid PET/MR system not only to simplify the experimental procedure but also to provide simultaneous measurements under the same tumor pH and metabolic microenvironment. The precise roles of glucose transporters were not examined in this study – histological information about these transporters will be acquired in future studies, and the correlation between the distribution of these glucose transporters and the tumor pH_i environment can then be evaluated [1,2]. A measurement of pH_e would also aid in interpreting these results. We plan on acquiring this information in a future study simultaneously with acidoCEST [3,4] to provide a more complete picture of the tumor pH environment (see Chapter 4). The current 60-min glucose infusion protocol leads to hyperglycemia by the end of the AACID CEST experiment. The acute change in pH_i environment after the glucose infusion was not measured in the current study due to a different CEST acquisition protocol that was used during the first half of glucose infusion. Moreover, the Lac:Pyr value obtained from the MRSI right after would be elevated under hyperglycemia [5–7] – a CEST acquisition promptly following a bolus injection of moderate dose will be implemented in the future to avoid an overly large alteration of the tumor glycolytic environment.

5.3 Chapter 4: Glucose Infusion Induced Change in Intracellular pH and Its Relationship with Tumor Glycolysis in a C6 Rat Model of Glioblastoma.

In this chapter, both tumor intra- and extracellular pH environment was evaluated using CEST MRI with AACID and acidoCEST techniques respectively. The change in tumor pH_i and pH_e was measured after a glucose injection. The relationship between the tumor pH environment and its glycolytic activity measured using dynamic FDG-PET was also evaluated. This chapter demonstrated the possibility of measuring both intracellular and extracellular pH simultaneously using CEST MRI. CEST MRI was also able to detect the change in tumor pH_i and pH_e after a glucose injection. The intrinsic relationship between

tumor and peritumor pH environments (tumor pH_i and peritumor pH_e) could potentially help predict tumor invasion. Tumor glycolytic metabolism and its effect on tumor pH_e was also shown in this study. A strong correlation between tumor glycolysis and pH_e might suggest that acidoCEST measurement could be a surrogate measurement of tumor glycolysis. The above findings illustrate the importance of understanding the tumor pH environment as it relates to tumor metabolism.

Other than the limitations mentioned previously, there were a few limitations for the work presented in this chapter: similar to what was mentioned previously, all imaging was done in a sequential order, as a result the tumor glycolytic and pH environment were not identical during the experiment. A simultaneous PET/MR system can potentially capture both tumor glycolytic metabolism and its pH environment simultaneously in a single session. The information regarding tumor hypoxia was missing from the presented study. Tumor hypoxia will aggravate the acidosis in tumor pH_e due to the Warburg effect [2,8,9]. Tumor hypoxia can be investigated *ex vivo* using histopathology with pimonidazole [10,11], or *in vivo* with hypoxia associated PET tracers such as ^{18}F -flurozaomycin arabinoside (FAZA) [12,13]. The kinetic analysis performed in this study assumed there is no reversible transfer from the bound compartment to the free compartment using Patlak graphical analysis [14,15]. A recent study demonstrated that the “trapped” ^{18}F -FDG6P can be transferred back to extracellular space [16]. A more sophisticated modeling method could be employed in the future to account for the possible reversible pharmacokinetics of FDG.

5.4 Future Directions

All imaging presented in Chapter 2, 3 and 4 was done in a sequential order, and on multiple scanners in 2 days, as a result, the tumor microenvironment was not identical. Future experiments can be done using a PET/MRI system [17,18] to simplify the experimental design and capture a more accurate snapshot of the tumor microenvironment.

This thesis investigated the relationship between tumor perfusion, glycolytic metabolism and its pH environment, however the role that cancer hypoxia played in this vicious cycle was not examined. Tumor hypoxia in combination with the Warburg effect will exacerbate tumor acidosis [2,8,9,19]. The effect of hypoxia can be investigated invasively *in vivo* using a probe measuring partial pressure of oxygen (pO_2) [20], or using an implantable microfabricated oxygen sensor [21]; it can be imaged non-invasively using PET with hypoxia sensitive tracers such as ^{18}F -flurozaomycin arabinoside (FAZA) [12,13] and ^{18}F -fluronisonidazoles (FMISO) [22], or using optical sensing approaching with luminescent probes described as Förster resonance energy transfer (FRET) complexes [23]; or via histopathology using pimonidazole [24]. Future studies can incorporate some of the techniques mentioned above to fill in the missing piece that tumor hypoxia plays in the vicious cycle of tumor proliferation.

FDG-PET can provide information on tumor glycolytic activity [9], however, FDG can also be taken up by cells such as microglia and tumor-associated macrophages activated during an inflammatory response induced by cancer cells [25]. This could lead to overestimation of tumor volume and tumor glycolytic metabolism using FDG-PET [26]. Ideally, the information related to inflammatory response could be measured separately and also subtracted from FDG-PET so that tumor glycolysis can be estimated more accurately. Multiple PET tracers have been developed to investigate inflammatory response, including tracers such as ^{11}C -PK11195 and ^{18}F -FEPPA that target the translocator protein (TSPO) overexpressed in the mitochondria of activated microglia and macrophages under inflammation [27,28]. However, these tracers will also target reactive astrocytes, endothelial cells and glioma cells as well [29,30], resulting in an inaccurate measurement of inflammation in a glioma model. A PET tracer targeting the macrophage colony-stimulation factor 1 receptor (CSF1R) that is primarily expressed on microglia has been developed [31]. Using a PET tracer targeting CSF1R might provide a more accurate measurement of inflammation relative to TSPO tracers mentioned above [32]. Moreover, these tracers can be labeled with a 20-minute half-life radioisotope ^{11}C , such as ^{11}C -CPPC, and enable the possibility of imaging inflammation with ^{11}C -CPPC and tumor glycolysis

using ^{18}F -FDG sequentially in one PET imaging session. CEST MRI can also be used to evaluate inflammatory response by indirectly measuring the elevated endogenous glutamate (~ 3 ppm downfield from bulk of water) during inflammation [33–35]. Future experiments could perform a dual-tracer PET session sequentially using ^{11}C -CPPC and ^{18}F -FDG to measure and separate inflammatory cells in the tumor from tumor glycolysis, a CEST session measuring glutamate and/or pH can occur simultaneously using a PET/MR system or an MR-compatible PET insert.

The simultaneous detection of intra- and extracellular pH with CEST can be utilized in tracking cancer treatment response. As mentioned previously, cancer has a neutral to slightly alkaline pH_i and more acidic pH_e [2,36], chemotherapy and/or radiotherapy would reverse this pH distribution across the intracellular and extracellular space i.e., a more acidic tumor pH_i and more neutral pH_e [37–39] in order to achieve a good treatment outcome [37,40]. As a result, treatment response and progress can be tracked if the change in cancer pH environment (both pH_i and pH_e) can be monitored throughout the treatment session. In the future, experiments will be designed to monitor the change in tumor pH environment for subjects receiving either chemotherapy or radiotherapy with AACID and acidoCEST MRI. The effect of tumor metabolism can be tracked with FDG-PET simultaneously using either a PET/MR system or an MR-compatible PET insert. Kinetic analysis of FDG-PET can also be modeled more accurately by including a reversible transfer rate constant (k_4) as mentioned above. The relationship between the tumor pH environment and its glycolytic activity can be examined longitudinally throughout the treatment period. The effectiveness of the treatments either using chemotherapy or radiotherapy can be accessed based on the change in tumor pH environment and its glycolytic metabolism.

5.5 Conclusion

This thesis explored the intrinsic relationships between cancer perfusion, glycolysis and its pH environment using a multimodal *in vivo* imaging approach. In Chapter 2, we show that glucoCEST is more related to measurements of perfusion than glycolysis. In Chapters 3

and 4, we show that the change in tumor pH environment can be monitored using CEST MRI after a glucose injection. To our knowledge, this thesis includes the first study measuring pH_i and pH_e simultaneously using CEST MRI in a single session (Chapter 4).

5.6 Reference

1. Estrella V, Chen T, Lloyd M, et al. (2013) Acidity Generated by the Tumor Microenvironment Drives Local Invasion. *Cancer Res* 73(5):1524-1535.
2. Corbet C, Feron O. (2017) Tumour Acidosis: From the Passenger to the Driver's seat. *Nat Rev Cancer* 17(10):577-593.
3. Chen LQ, Howison CM, Jeffery JJ, et al. (2014) Evaluations of extracellular PH within in vivo tumors using acidocest MRI. *Magn Reson Med* 72(5):1408-1417.
4. Longo DL, Bartoli A, Consolino L, et al. (2016) *In Vivo* Imaging of Tumor Metabolism and Acidosis by Combining PET and MRI-CEST pH Imaging. *Cancer Res* 76(22):6463-6470.
5. Lund J, Ouwens DM, Wettergreen M, et al. (2019) Increased Glycolysis and Higher Lactate Production in Hyperglycemic Myotubes. *Cells* 8(9):1101.
6. Twarock S, Reichert C, Peters U, et al. (2017) Hyperglycemia and aberrated insulin signaling stimulate tumor progression via induction of extracellular matrix component hyaluronan. *Int J Cancer* 141: 791-804.
7. Qi Q, Fox MS, Lim H, et al. (2021) Multimodality In Vivo Imaging of Perfusion and Glycolysis in a Rat Model of C6 Glioma. *Mol Imaging Biol* 23: 516-526
8. Webb BA, Chimenti M, Jacobson MP, et al. (2011) Dysregulated pH: A Perfect Storm for Cancer Progression. *Nat Rev Cancer* 11(9):671-677.
9. Xu XD, Shao SX, Jiang HP, et al. (2015) Warburg Effect or Reverse Warburg Effect? A Review of Cancer Metabolism. *Oncol Res Treat* 38(3):117-122.
10. Kaanders JH, Wijffels K, Marres H, et al. (2002) Pimonidazole Binding and Tumor Vascularity Predict for Treatment Outcome in Head and Neck Cancer. *Cancer Res* 62(23):7066-7074.
11. Qi Q, Yeung TPC, Lee TY, et al. (2016) Evaluation of CT perfusion biomarkers of tumor hypoxia. *PLoS One* 11(4):e0153569.
12. Melsens E, De Vlieghere E, Descamps B, et al. (2018) Hypoxia imaging with ¹⁸F-FAZA-PET/CT predicts radiotherapy response in esophageal adenocarcinoma xenografts. *Radiat Oncol* 13(1):39.
13. Fiona Li (2020) Kinetic Analysis of Dynamic PET for Molecular, Functional and Physiological Characterization of Diseases. PhD

Thesis.

14. van den Hoff J, Hofheinz F, Oehme L, et al. (2013) Dual time point based quantification of metabolic uptake rates in 18F-FDG PET. *EJNMMI Res* 3(1):1-11.
15. Gunn RN, Gunn SR, Cunningham VJ. (2001) Positron emission tomography compartmental models. *J Cereb Blood Flow Metab* 21(6):635-652.
16. Yang DM, Palma D, Louie A, et al. (2019) Assessment of tumour response after stereotactic ablative radiation therapy for lung cancer: A prospective quantitative hybrid 18F-fluorodeoxyglucose-positron emission tomography and CT perfusion study. *J Med Imaging Radiat Oncol* 63(1):94-101
17. Wilk B. (2021) Measuring inflammation in the entire myocardium in a canine model of myocardial infarction with hybrid PET/MRI. PhD Thesis.
18. Goldenberg JM, Cárdenas-Rodríguez J, Pagel MD. (2018) Preliminary Results that Assess Metformin Treatment in a Preclinical Model of Pancreatic Cancer Using Simultaneous [¹⁸F]FDG PET and acidoCEST MRI. *Mol Imaging Biol* 20(4):575-583.
19. Heiden MG, Cantley LC, Thompson CB. (2009) Understanding the warburg effect: The metabolic requirements of cell proliferation. *Science* 324(5930):1029-1033.
20. Griffiths JR, Robinson SP. (2014) The OxyLite: a fibre-optic oxygen sensor. *Br J Radiol* 859:627-630.
21. Marland JRK, Gray ME, Dunare C, et al. (2020) Real-time measurement of tumour hypoxia using an implantable microfabricated oxygen sensor. *Sens Bio-Sensing Res* 30:100375.
22. Lee GH, Kim JS, Oh SJ, et al. (2015) ¹⁸F-fluoromisonidazole (FMISO) Positron Emission Tomography (PET) Predicts Early Infarct Growth in Patients with Acute Ischemic Stroke. *J Neuroimaging* 25(4):652-655.
23. Xu Y, Piston DW, Johnson CH. (1999) A bioluminescence resonance energy transfer (BRET) system: Application to interacting circadian clock proteins. *Proc Natl Acad Sci USA* 96(1):151.
24. Varia M a, Calkins-Adams DP, Rinker LH, et al. (1998) Pimonidazole: a novel hypoxia marker for complementary study of tumor hypoxia and cell proliferation in cervical carcinoma. *Gynecol Oncol* 71(2):270-277.
25. Balkwill FR, Mantovani A. (2011) Cancer-related inflammation: Common themes and therapeutic opportunities. *Semin Cancer Biol* 22:33-40.

26. Chang JM, Lee HJ, Goo JM, et al. (2006) False Positive and False Negative FDG-PET Scans in Various Thoracic Diseases. *Korean J Radiol* 7(1):57.
27. Su Z, Herholz K, Gerhard A, et al. (2013) [¹¹C]-(R)PK11195 tracer kinetics in the brain of glioma patients and a comparison of two referencing approaches. *Eur J Nucl Med Mol Imaging* 40(9):1406.
28. Al-Khishman NU, Qi Q, Roseborough AD, et al. (2020) TSPO PET detects acute neuroinflammation but not diffuse chronically activated MHCII microglia in the rat. *EJNMMI Res* 10(1):1-10.
29. Onuska KM. (2020) The Dual Role of Microglia in the Progression of Alzheimer's Disease. *J Neurosci* 40(8):1608.
30. Ammer LM, Vollmann-Zwerenz A, Ruf V, et al. (2020) The Role of Translocator Protein TSPO in Hallmarks of Glioblastoma. *Cancers (Basel)* 12(10):1-26.
31. Akiyama H, Nishimura T, Kondo H, et al. (1994) Expression of the receptor for macrophage colony stimulating factor by brain microglia and its upregulation in brains of patients with Alzheimer's disease and amyotrophic lateral sclerosis. *Brain Res* 639(1):171-174.
32. Horti AG, Naik R, Foss CA, et al. (2019) PET imaging of microglia by targeting macrophage colony-stimulating factor 1 receptor (CSF1R). *Proc Natl Acad Sci USA* 116(5):1686-1691.
33. Haroon E, Miller AH, Sanacora G. (2017) Inflammation, Glutamate, and Glia: A Trio of Trouble in Mood Disorders. *Neuropsychopharmacology* 42(1):193.
34. Cai K, Haris M, Singh A, et al. (2012) Magnetic resonance imaging of glutamate. *Nat Med* 18(2):302-306.
35. Chen YZ, Dai ZZ, Shen ZW, et al. (2016) Magnetic resonance imaging of glutamate in neuroinflammation. *Radiol Infect Dis* 3(2):92-97.
36. Webb BA, Chimenti M, Jacobson MP, et al. (2011) Dysregulated pH: A perfect storm for cancer progression. *Nat Rev Cancer* 11(9):671-677.
37. Hao G, Xu ZP, Li L. (2018) Manipulating extracellular tumour pH: an effective target for cancer therapy. *RSC Adv* 8(39):22182-22192.
38. Albatany M. (2018) Monitored Acute Pharmacologic Modulation of Glioblastoma pH Monitored by Chemical Exchange Saturation Transfer Magnetic Resonance Imaging. PhD Thesis.
39. Lim H, Albatany M, Martínez-Santesteban F, Bartha R, et al. (2018) Longitudinal

Measurements of Intra-and Extracellular pH Gradient in a Rat Model of Glioma. *Tomography* 4(2): 46-54.

40. Ward C, Meehan J, Gray ME, et al. (2020) The impact of tumour pH on cancer progression: strategies for clinical intervention. *Explor Target Anti-tumor Ther.* 1(2):71-100.

Appendices

Appendix A: Animal use protocol for Chapter 2, 3 and 4:

PI :	Thiessen, Jonathan
Protocol #	2018-101
Status :	Approved (w/o Stipulation)
Approved :	06/01/2019
Expires :	06/01/2023
Title :	Assessing C6 Glioma Brain Tumors with Multimodal Imaging



AUP Number: 2018-101

PI Name: Thiessen, Jonathan

AUP Title: Assessing C6 Glioma Brain Tumors with Multimodal Imaging

Approval Date: 06/01/2019

Official Notice of Animal Care Committee (ACC) Approval:

Your new Animal Use Protocol (AUP) 2018-101:1: entitled " Assessing C6 Glioma Brain Tumors with Multimodal Imaging " has been APPROVED by the Animal Care Committee of the University Council on Animal Care. This approval, although valid for up to four years, is subject to annual Protocol Renewal.

Prior to commencing animal work, please review your AUP with your research team to ensure full understanding by everyone listed within this AUP.

As per your declaration within this approved AUP, you are obligated to ensure that:

1) Animals used in this research project will be cared for in alignment with:

a) Western's Senate MAPPs 7.12, 7.10, and 7.15

http://www.uwo.ca/univsec/policies_procedures/research.html

b) University Council on Animal Care Policies and related Animal Care Committee procedures

http://uwo.ca/research/services/animalethics/animal_care_and_use_policies.htm

2) As per UCAC's Animal Use Protocols Policy,

a) this AUP accurately represents intended animal use;

b) external approvals associated with this AUP, including permits and scientific/departmental peer approvals, are complete and accurate;

c) any divergence from this AUP will not be undertaken until the related Protocol Modification is approved by the ACC; and

d) AUP form submissions - Annual Protocol Renewals and Full AUP Renewals - will be submitted and attended to within timeframes outlined by the ACC.

e)

http://uwo.ca/research/services/animalethics/animal_use_protocols.html

3) As per MAPP 7.10 all individuals listed within this AUP as having any hands-on animal contact will

- a) be made familiar with and have direct access to this AUP;
- b) complete all required CCAC mandatory training (training@uwo.ca);

and

- c) be overseen by me to ensure appropriate care and use of animals.

4) As per MAPP 7.15,

- a) Practice will align with approved AUP elements;
- b) Unrestricted access to all animal areas will be given to ACVS Veterinarians and ACC Leaders;
- c) UCAC policies and related ACC procedures will be followed, including but not limited to:

- i) Research Animal Procurement
- ii) Animal Care and Use Records
- iii) Sick Animal Response
- iv) Continuing Care Visits

5) As per institutional OH&S policies, all individuals listed within this AUP who will be using or potentially exposed to hazardous materials will have completed in advance the appropriate institutional OH&S training, facility-level training, and reviewed related (M)SDS Sheets, <http://www.uwo.ca/hr/learning/required/index.html>

Submitted by: Copeman, Laura
on behalf of the Animal Care Committee
University Council on Animal Care

Appendix B: Copyright for Chapter 2: Multimodality In Vivo Imaging of Perfusion and Glycolysis in a Rat Model of C6 Glioma

This Agreement between Mr. Qi Qi ("You") and Springer Nature ("Springer Nature") consists of your license details and the terms and conditions provided by Springer Nature and Copyright Clearance Center.

License Number	5207320881447
License date	Dec 13, 2021
Licensed Content Publisher	Springer Nature
Licensed Content Publication	Molecular Imaging and Biology
Licensed Content Title	Multimodality In Vivo Imaging of Perfusion and Glycolysis in a Rat Model of C6 Glioma
Licensed Content Author	Qi Qi et al
Licensed Content Date	Feb 3, 2021
Type of Use	Thesis/Dissertation
Requestor type	academic/university or research institute
Format	electronic
Portion	full article/chapter

Curriculum Vitae

Name: Qi Qi

Post-Secondary Education and Degrees:

Bachelor of Medical Science, Honours Specialization in Medical Biophysics (clinical concentration)

The University of Western Ontario 2012-2016

PhD of Medical Science, Medical Biophysics

The University of Western Ontario May 2016-

Supervised by: Dr. Jonathan Thiessen and Dr. Ting Yim Lee

Related Work Experience Teaching Assistant, Department of Applied Math
The University of Western Ontario
2017-2020

Presentations and Publications:

Conference presentations:

Poster presentation International Society for Magnetic Resonance in Medicine (2021), “Comparison of Tumour pH Environment and Glycolysis Measurements in a C6 Rat Model of Glioma”. Vancouver, Canada.

Author list: Qi Qi, Matthew S. Fox, Heeseung Lim, Harris Smailovic, Rebecca Sullivan, Alex Li, Miranda Bellyou, Lise Desjardins, Andrew McClennan, Robert Bartha, Timothy J. Scholl, Lisa Hoffman, Ting-Yim Lee, Jonathan D. Thiessen.

Poster presentation World Molecular Imaging Congress (2019), “Comparison of Tumour pH Environment and Glycolysis Measurements in a C6 Rat Model of Glioma”. Montreal, Canada.

Author list: Qi Qi, Matthew S. Fox, Heeseung Lim, Rebecca Sullivan, Alex Li, Miranda Bellyou, Lise Desjardins, Andrew McClennan, Robert Bartha, Timothy J. Scholl, Lisa Hoffman, Ting-Yim Lee, Jonathan D. Thiessen.

Poster presentation AAN (2018), “Multimodal Imaging of White Matter Inflammation in a Rat Model of Striatal Ischemic Stroke” Los Angeles, USA.

Alex Levit, Austyn Roseborough, Matthew S. Fox, Qi Qi, Jonathan D. Thiessen, Shawn N. Whitehead

Poster presentation World Molecular Imaging Congress (2018), “Comparison of Glucose-CEST with Perfusion and Glycolysis Measurements in a C6 Rat Model of Glioma” Seattle, USA.

Author list: Qi Qi, Matthew S. Fox, Heeseung Lim, Fiona Li, Robert Bartha, Timothy J. Scholl, Lisa Hoffman, Ting-Yim Lee, Jonathan D. Thiessen.

Poster presentation Imaging Network of Ontario (2018), “Correcting the Arterial Input Function for Dynamic ^{18}F -FEPPA PET in Transgenic Fischer 344 Rats with Manual Blood Sampling.” Toronto, Canada.

Author list: Qi Qi, Alex Levit, Austyn Roseborough, Matthew S. Fox, Jonathan D. Thiessen, Shawn N. Whitehead

Poster presentation Imaging Network of Ontario (2017), “Evaluation of Tumour Perfusion and Glycolysis using C6 Model of Glioma” London, Canada.

Author list: Qi Qi, Matthew S. Fox, Heeseung Lim, Robert Bartha, Timothy J. Scholl, Lisa Hoffman, Ting-Yim Lee, Jonathan D. Thiessen.

Poster presentation London Health Research Day (2016), “Correlation of Digital Histology Images of the Human Lung to in vivo Computed Tomography Imaging: A Feasibility Study” London, Canada

Author List: Qi Qi, Sarah A. Mattonen, David A. Palma, Keith Kwan, Aaron D. Ward

Platform and poster presentation Imaging Network Ontario conference (2015), “Evaluation of CT Perfusion as a Surrogate Biomarker of Tumour Hypoxia” London, Canada.

Author list: Qi Qi Timothy Pok Chi Yeung, Dr. Ting-Yim Lee, Glenn Bauman, Cathie Crukley, Laura Morrison, Slav Yartsev.

Poster presentation London Health Science Research Day (2015), “Evaluation of CT Perfusion as a Surrogate Biomarker of Tumour Hypoxia”, London Canada.

Author list: Qi Qi Timothy Pok Chi Yeung, Dr. Ting-Yim Lee, Glenn Bauman, Cathie Crukley, Laura Morrison, Slav Yartsev.

Poster presentation CIHR-STP in Cancer Research & Technology Transfer (CaRTT) and the Department of Oncology 12th Annual Research & Education Day (2015), “Evaluation of CT Perfusion as a Surrogate Biomarker of Tumour Hypoxia” London, Canada.

Author list: Qi Qi Timothy Pok Chi Yeung, Dr. Ting-Yim Lee, Glenn Bauman, Cathie Crukley, Laura Morrison, Slav Yartsev.

Publications:

Co-author “A human-Derived Dual MRI/PET Reporter Gene System with High Translational Potential for Cell Tracking” *Mol Imaging Biol.* Accepted December 2021.

Primary author: Nourhan Shalaby, co-authors: John Kelly, Francisco Martinez, Qi Qi, Matthew S. Fox, Justin Hicks, Jonathan D. Thiessen, Timothy J School, John Ronald.

Primary author “Glucose Infusion Induced Change in Intracellular pH and Its Relationship with Tumor Glycolysis in a C6 Rat Model of Glioblastoma.” *Mol Imaging Biol.* Revision required, submitted November 2021.

Co-authors: Matthew S. Fox, Heeseung Lim, Rebecca Sullivan, Alex Li, Miranda Bellyou, Lise Desjardins, Andrew McClennan, Robert Bartha, Lisa Hoffman, Timothy J. Scholl, Ting-Yim Lee, Jonathan D. Thiessen

Primary author “Multimodality In Vivo Imaging of Perfusion and Glycolysis in a Rat Model of C6 Glioma.” *Mol Imaging Biol.* 2021. **23**: 516-526. DOI: 10.1007/s11307-021-01585-1.

Co-authors: Matthew S. Fox, Heeseung Lim, Robert Bartha, Timothy J. Scholl, Lisa Hoffman, Ting-Yim Lee, Jonathan D. Thiessen.

Second author “TSPO PET detects acute neuroinflammation but not diffuse chronically activated MHCII microglia in the rat” *EJNMMI Research.* 2020, 10(1): 133, DOI: 10.1186/s13550-020-00699-x.

Primary author: Nassir U. Al-Khishman, co-authors: Qi Qi, Austyn D. Roseborough, Alex Levit, Brian L. Allman, Udunna C. Anazodo, Mathew S. Fox, Shawn Whitehead, Jonathan D Thiessen

Primary author “Evaluation of CT Perfusion as a Surrogate Biomarker of Tumour Hypoxia” *PLoS ONE* 2016, 11(4): e0153569 DOI: 10.1371/journal.pone.0153569

Co-authors: Qi Qi Timothy Pok Chi Yeung, Dr. Ting-Yim Lee, Glenn Bauman, Cathie Crukley, Laura Morrison, Slav Yartsev.

Invited Presentations:

ISMRM Hyperpolarization Methods Study Group, November 17th, 2021, “Multimodality In Vivo Imaging of Perfusion and Glycolysis in a Rat Model of C6 Glioma.” Zoom.

International Forum of Nuclear Medicine and Molecular Imaging, June 2018, Zhengzhou, China.